Title

SPITZER-IRS HIGH-RESOLUTION SPECTROSCOPY OF THE 12 μm SEYFERT GALAXIES. II. RESULTS FOR THE COMPLETE DATA SET

Journal
The Astrophysical Journal, 709(2)

ISSN
0004-637X

Authors

Tommasin, Silvia
Spinoglio, Luigi
Malkan, Matthew A
et al.

Publication Date
2010-02-01

DOI
10.1088/0004-637x/709/2/1257

Peer reviewed

Not to appear in Nonlearned J., 45.
Preprint typeset using LaTeX style emulateapj v. 6/6/04

SPITZER-IRS HIGH RESOLUTION SPECTROSCOPIC SURVEY OF THE 12μM SEYFERT GALAXIES: II. RESULTS FOR THE COMPLETE DATASET

Silvia Tommasin[1], Luigi Spinoglio
Istituto di Fisica dello Spazio Interplanetario, INAF, Via Fosso del Cavaliere 100, I-00133 Roma, Italy

Matthew A. Malkan
Astronomy Division, University of California, Los Angeles, CA 90095-1547, USA

and

Giovanni Fazio
Harvard-Smithsonian Center for Astrophysics, 60 Garden Street, Cambridge, MA 02138

Not to appear in Nonlearned J., 45.

ABSTRACT

We present our *Spitzer* IRS spectroscopic survey from $10\mu m$ to $37\mu m$ of the Seyfert galaxies of the $12\mu m$ Galaxy Sample, collected in high resolution mode (R$\sim$ 600). The new spectra of 61 galaxies, together with the data we already published, gives us a total of 91 $12\mu m$ Seyfert galaxies observed, out of 112. We discuss the mid-IR emission lines and features of the Seyfert galaxies, using an improved AGN classification scheme: instead of adopting the usual classes of Seyfert 1's and Seyfert 2's, we use the spectropolarimetric data from the literature to divide the objects into categories "AGN 1" and "AGN 2", where AGN 1's include all broad-line objects, including the Seyfert 2's showing hidden broad lines in polarized light. The remaining category, AGN 2's contains only Seyferts with no detectable broad lines in either direct or polarized spectroscopy. We present various mid-IR observables, such as ionization-sensitive and density-sensitive line ratios, the PAH 11.25μm feature and the H_2 S(1) rotational line equivalent widths, the ($60\mu m$ - $25\mu m$) spectral index and the source extendedness at $19\mu m$, to characterize similarities and differences in the AGN populations, in terms of AGN dominance versus star formation dominance.

We find that the mid-IR emission properties characterize all the AGN 1's objects as a single family, with strongly AGN-dominated spectra. In contrast, the AGN 2's can be divided in two groups, the first one with properties similar to the AGN 1's except without detected broad lines, and the second with properties similar to the non-Seyfert galaxies, such as LINERs or starburst galaxies.

We computed a semianalytical model to estimate the AGN and the starburst contributions to the mid-IR galaxy emission at $19\mu m$. For 59 galaxies with appropriate data, we can separate the $19\mu m$ emission into AGN and starburst components using the measured mid-IR spectral features. We use these to quantify the brightness thresholds that an AGN must meet to satisfy our classifications: AGN 1 have an AGN contribution $\geq$ 73 % and AGN 2 $\geq$ 45 % of their total emission at $19\mu m$.

The detection of [NeV] lines turns out to be an almost perfect signature of energy production by an AGN. Only 4 ($\sim$ 7.5% percent) of 55 AGN 1 and 2 (10% percent) out of 20 AGN 2 do not have [NeV] 14.3μm down to a flux limit of $\sim 4\times10^{-15} erg s^{-1} cm^{-2}$. We present mean spectra of the various AGN categories. Passing from AGN-dominated to starburst-dominated objects, the continuum steepens, especially at wavelengths shorter than $20\mu m$, while the PAH feature increases in its equivalent width and the high ionization lines decrease.

We estimate H_2 mass and excitation temperature through the measurement of the S(1) rotational line of this molecule. Finally we derive the first local luminosity functions for the brighest mid-infrared lines and the PAH feature at $11.25\mu m$. No statistical difference is apparent in the space densities for Seyfert 1's and 2's of a given line luminosity, nor for the new classes of AGN 1's and 2's. We use the correlation between [Ne V] line and nonstellar infrared continuum luminosity to derive the global output of accretion-powered galactic nuclei in the local universe.

Subject headings: Galaxies: Active - Galaxies: Starbursts - Infrared: Galaxies

1. INTRODUCTION

This paper contains the final results of the *Spitzer* high-resolution IRS spectroscopic survey of the sample of Seyfert galaxies (hereafter 12MSG) included in the *IRAS* 12μm galaxy sample (Rush, Malkan & Spinoglio 1993, hereafter RMS). In Tommasin et al. (2008) (hereafter Paper I) we have presented and analyzed the first 30 high-resolution spectra of 29 Seyfert galaxies of this sample (one IRAS galaxy, Mrk 1034, was coincident with a pair, for which we obtained two spectra). The first spectroscopic observations of active galaxies with the Infrared Spectrometer (Houck et al. 2004, IRS) onboard the *Spitzer Space Observatory* (Werner et al. 2004) have been collected on classical AGNs (Weedman et al. 2005) and ULIRGs (Armus et al. 2007). Af-

---

[1] also at the Physics Department of Universitá di Roma, La Sapienza, Roma, Italy

ter the work presented in Paper I and the referenced works therein, a few more studies have discussed the Spitzer mid-infrared spectra of Seyfert galaxies, among these Deo et al. (2007), Meléndez et al. (2008a) and Wu et al. (2009). As expected, the mid-infrared spectra of Seyfert galaxies show forbidden lines originating in the Narrow Line Regions, excited by the AGN ionizing flux. This power is thought to be produced by black-hole accretion, i.e., ultimately from the conversion of gravitational into radiative energy. The fine structure lines of [NeV] at 14.32μm and 24.31μm originate exclusively in the highly ionized gas (with an ionization potential of 97eV) illuminated by the AGN[2]. As discussed in Paper I, the [OIV] line at 25.88μm (ionization potential of 55eV) is most probably excited from the AGN. In fact, Meléndez et al. (2008b) consider this line as an accurate and truly isotropic indicator of AGN activity, even if it could also originate from high excitation starburst emission or in shocks in low-metallicty starbursts (Lutz et al 1998).

The [NeIII]15.55μm line (Ne+ and Ne++ have ionization potentials of 14eV less than O++ and O+++ respectively) can be excited both from AGN activity (Gorjian, Cleary & Werner 2007) and from starbursts (Thornley et al. 2000). Superimposed on the AGN spectra, the lines of [NeII]12.81μm, [SIII]18.71μm and 33.48μm and [SiII]34.82μm originate in gas with moderate ionization and most of their emission is generated by young newly formed stars, even if some contribution from the AGN is also expected (Spinoglio & Malkan 1992). The relationship between the [OIV]25.88μm, [NeIII]15.55μm and [NeII]12.81μm lines in an eterogeneous sample of Seyfert galaxies has been studied by Meléndez et al. (2008a), who found that Seyfert 1's and Seyfert 2's have different AGN and star formation contributions to the total emission.

The interstellar medium produces the pure rotational lines of molecular hydrogen, as already shown by the early results of *ISO* spectroscopy in Genzel et al. (1998) and Rigopoulou et al. (2002), respectively. Wu et al. (2009) analyzed the IRS low resolution spectra of 103 Seyfert galaxies from the 12MSG and measured the policyclic aromatic hydrocarbons (hereafter PAH) emission features and the Silicate absorption strength. The PAHs have been proposed as star formation tracers by Puget & Leger (1989), while the Silicate absorption is sensitive to heavy dust obscuration of the nucleus.

According to the simplest Unified Model for AGN, the Accreting Torus Model (ATM) (Malkan, Gorjian & Tam 1998), Seyfert 1 and 2 galaxies are the same kind of objects, only viewed from different angles. The strongest demonstration of this is detection via optical spectropolarimetry of the Broad Line Region emission–the defining characteristic of Seyfert 1'–in a significant minority of Seyfert 2 galaxies (Antonucci & Miller 1985; Antonucci 1993). A different scenario postulates an evolutionary difference: that Seyfert 2 are the early stages of the transition of HII/Starburst galaxies into Seyfert 1's. Two suggested evolutionary progressions are HII → Seyfert 2 (Kauffmann et al. 2003; Storchi-Bergmann et al. 2001), or a fuller scenario of HII → Seyfert 2 → Seyfert 1 (Hunt & Malkan 1999; Krongold, Dultzin-Hacyan & Marziani 2002; Levenson, Weaver & Heckman 2001). Because the radiation due to the star formation processes is roughly isotropic, the ATM predicts no observational difference in the star formation tracers between Seyfert 1's and 2's. If, on the other hand, star formation is stronger in Seyfert 2's, as suggested in Buchanan et al. (2006), then some evolution from Seyfert 2's to Seyfert 1's could be invoked. If general interstellar extinction towards the center of the galaxy is extremely high, optical data alone might not always provide the correct (intrinsic) classification.

Our sample is described in §2, the observations and the data reduction are briefly reported in §3, the direct results of our observations, the estimates of the H_2 masses and temperatures and the measure of the continuum extendedness are presented in §4, the diagnostic diagrams and the semianalytical models to interpret them are presented and discussed in §5. In §6 the [NeV] is quantified as an unambiguous AGN activity indicator, in §7 we show that the mid-infrared diagnostics differentiate AGN 1's from the other populations, and we derive the average spectra for each class of objects that can be used as templates also for predictions and comparisons with high redshift populations. Finally in §8 we present the line luminosity functions for our sample, and calculate the total accretion power generated in the local universe. The conclusions are summarized in §9.

2. THE SEYFERT GALAXIES OF THE 12μM GALAXY SAMPLE

From the original Seyfert galaxies list of the RMS, we present 91 IRS high-resolution spectra, including one third of them which were published in Paper I. Our final sample is over 80% complete, large enough to give reasonable statistical results, with 41 Seyfert 1's, 47 Seyfert 2's and 3 galaxies which have been reclassified as optical starburst galaxies, according to NED [3].

Another improvement of this work is the classification that we adopt: we reclassify the Seyfert 1's and 2's into more general *"AGN 1's"* and *"AGN 2's"*. We consider AGN 1's to be all those with broad line regions, including those Seyfert 2's with *hidden broad line regions* (hereafter HBLR), observed in polarized light. The remaining Seyfert 2's lacking any broad permitted lines, even in polarized light, are classified as AGN 2's. Our classification scheme is an attempt to identify a 'clean' category of intrinsically broad-line AGN. We follow Tran (2001) and Tran (2003), who made a spectropolarimetric survey of the 12MSG. Out of the original 47 Seyfert 2's, they found HBLR in 19, 20 lacking an HBLR and they reclassify 11 objects as LINER, HII or starburst galaxies[4]. We classifiy as non-Sy for all these latter objects and similar ones (in the diagrams LINER and HII or starburst galaxies will be distinguished). Exceptions are NGC1097 and MRK897, that we reclassify as being a AGN 1 and an

---

[2] either currently or some time during the last several hundred years, because, even if the AGN ionizing continuum could be completely switched off, the photoionized NLR could still be detected, due to its large extension and the long recombination time

[3] NASA Extragalactic Database, IPAC, Caltech Pasadena, http://nedwww.ipac.caltech.edu/

[4] Among these 11 objects: three (Mrk897, NGC7496 and NGC7590) were presented in Paper I and the other eight are: NGC1056, NGC1097, NGC4922, NGC5005, NGC6810, NGC7130, MCG+0-29-23 and CGCG381-051, whose IRS spectra are presented in this paper.

AGN 2 respectively. We refer to the Appendix A for the details on the classification of each one of these objects. Tran (2003) also adopt a somewhat arbitrary distinction between "bona fide" and "non-bona fide" Seyfert 1's, based on the NED classification of Seyfert 1.8, Seyfert 1.9 types and on radio loudness. For the remaining 13 objects not considered as "bona fide" Seyfert 1 in Tran (2003), we prefer instead to carefully classify them on the basis of detection or not of optical broad lines, either in direct or polarized spectra. We present the details on the classification of these 13 galaxies in Appendix A, while we summarize here that we classify as AGN 1 seven Sy1 of the original RMS list (NGC526A, NGC1097, NGC1365, NGC2639, NGC7316, ESO545-G13 and ESO362-G18), we classify as a HBLR NGC5347 (Moran 2007) and we reclassify as AGN 2 one galaxy (NGC5506), while we consider non-BLR four objects for which there is no evidence of broad lines, but they lack polarization observations (NGC1194, NGC4602, MRK1034 NED02 and MRK897) and finally we reclassify as non-Sy two galaxies (NGC3511 and MRK1034 NED01). Although Tran (2003) distinguish the radio-loud 3C galaxies, we actually classify 3C120, 3C234 and 3C445 as AGN 1, independently of their radio characteristics, because of the presence of broad line emission.

We note that 7 Seyfert 1's have Balmer lines with relatively small FWHM, under 2000 km/s but which are nonetheless produced in a BLR (Zhang & Wang 2006), These are usually classified as "narrow line Seyfert 1's", but our sample contains too few to define another category. It will turn out that their infrared spectra do not appear different from those of normal Seyfert 1's (see Sec. 4).

In summary our observed sample of "original" Seyfert galaxies contains 55 objects showing some evidence of broad lines, either in direct (34 Sy 1) or polarized light (21 HBLR) that we classify as AGN 1, 20 AGN 2 (non-HBLR) and 4 non-BLR not included in the AGN2 class. We will also consider in the following the 13 non-Sy galaxies, however these latter will not be used for any statistical derivation.

Following the results of Wu et al. (2009), who have defined as "20 μm peakers" the Seyfert galaxies having a flux ratio $F_{20\mu m}/F_{30\mu m} \geq 0.95$, we have also identified these in our sample[5] to search for any difference with our classes of galaxies. We refer to Appendix B for the results on these objects.

3. OBSERVATIONS AND DATA REDUCTION

Most of the sample galaxies–the 29 galaxies presented in Paper I and the 23 galaxies in this paper– have been observed within the Spitzer Guaranteed Time Project 30291 (P.I. Fazio). IRS high-resolution observations of another 37 objects, belonging to the 12MSG, were extracted from the SSC (Spitzer Science Center) archive. For 25 of the latter objects, the observing mode was similar to the one of P30291, namely the off-source observations have been collected to allow accurate background subtraction. For the remaining 12 sources from the archive (see Tab.1), no off-source observation was taken. For these objects, we give the line intensities, as for the other galaxies, but not the equivalent widths (EW) of the emission features and lines, nor do we present the photometric measurements at 19 and 19.5 μm for computing the extendedness of the sources, because of their large uncertainty in the level of the continuum. MRK335 was observed by the Program 50253 (P.I. Malkan), in the last cold cycle of Spitzer.

The whole data reduction was done using the SMART packages[6]. We refer to Paper I for more details of the data reduction and analysis.

4. OBSERVATIONAL RESULTS

The journal of the observations of the 61 galaxies presented here is shown in Tab.1, giving for each galaxy: the equatorial coordinates at the 2000 equinox; the redshift; the original RMS Seyfert class and the new classification; the IRAS fluxes at 12 and 25μm; the observing date and the number of cycles and integration times per cycle. For the sources already presented in Paper I, we refer to the table 11 in the appendix for the adopted classification.

The spectra of the new 61 galaxies are shown in Fig.1. For all galaxies for which the off-source spectra have been subtracted, both the SH and the LH spectra are presented. For the galaxies for which no off-source observation was available, we show in the figure the on-source SH spectrum only. This latter is only marginally affected by the lack of background subtraction, because the theoretical background, as measured using the background estimator provided by the SSC, is less than 10% of the total measured SH emission. For these galaxies, we show only the detected lines in the LH range; we do not present the whole spectrum, because it is affected by a higher level of background (estimated to be about 20-30% of the total measured emission). The spectra of MRK335, F05563-G018, NGC5135, IC4329A, NGC5347 and NGC5506 show only the LH detected lines, because after background subtraction, the LH orders are not well inter-calibrated and thus the continuum cannot be defined properly.

Tab.2 reports the fluxes of the fine structure lines, measured with a Gaussian fit, for both the SH and LH spectra. Tab.3 gives the fluxes of the molecular H_2 rotational lines S(0), S(1), S(2) and S(3) and the PAH 11.25μm integrated flux, measured with a moment fit, and its equivalent width. We consider as detections the measurements with a signal to noise ratio higher than 3. We also report in Tab. 11 in the appendix the PAH 11.25μm integrated flux and equivalent width as well as the H_2 masses derived from the H_2 rotational lines observations for the 30 spectra of the galaxies presented in Paper I. We have repeated the measurements of fluxes and equivalent widths of the PAH 11.25μm to be consistent with the following method adopted here, and also because we found that some of the equivalent widths given in Paper I were affected by non-traceable errors.

We measured the PAH fluxes by removing from the spectra the continuum under a baseline traced from the continuum shortwards of the PAH feature to the continuum longwards of the [NeII] line. Such a large interval

---

[5] The "20 μm peakers" in our sample are: MRK335, MRK348, NGC424, NGC526A, MCG-02-08-039, F03450+0055, ESO033-G002, MRK0006, MRK704, MRK1239, 3C234, MCG-06-30-015, IC4329A, NGC6860, NGC7213

[6] SMART is available on the SSC website and developed by the Infrared Spectrograph (IRS) Instrument Team at Cornell University (Higdon et al. 2004)

has been chosen because, in addition to the feature at 11.25μm, two other PAH features are present (approximately at 12.0μm and at 12.5μm) and they increase the level of the apparent continuum under the 11.25μm feature. The integration range of the PAH emission depends on the feature's intensity, for the brightest sources it can be as wide as 0.5 μm (11.15μm - 11.65μm). Chosing this large baseline allowed us to avoid the other PAH contributions and remove the correct continuum from the galaxy. By dividing the resulting PAH integrated flux by the continuum flux density at the midpoint wavelength of the baseline, we can obtain the EW of the feature.

4.1. *H_2 excitation diagrams: H_2 temperatures and masses*

Using the H_2 rotational lines intensities, we can estimate the temperature and the mass of the H_2 line emitting regions (see Paper I for the details of the method used). The derivation of the masses presented in Paper I was affected by some errors, therefore we recomputed their values, and list them in Table 9.

In Fig.2 the excitation diagrams of each of the sources are shown. Tab.4 presents the derived temperatures T(3-2), T(2-1), T(1-0) of the gas in those regions where the rotational lines S(3), S(2) and S(1) are emitted, respectively. The 0-0 S(1) is the most intense H_2 line in every source, and so we estimated the mass of the molecular regions from its intensity. We calculated the masses from the Boltzmann equation using the two transitions of S(0) and S(1), listing the results in Tab.4. Therefore we obtain the masses only for the 50 galaxies where both these rotational lines were detected, while we give an upper limit to the mass when only the S(1) line was detected. The temperature values that we derive here are comparable with the ones we report in Paper I.

The estimated H_2 masses are of the same order of magnitude as those calculated by Rigopoulou et al. (2002) in Seyfert and starburst galaxies and by Higdon et al. (2006) in ULIRGs, ranging from 10^7 to 10^9 $M_\odot$. The average mass (in units of 10^8 $M_\odot$) for the AGN 1 class is 1.8±1.3, for AGN 2 is 0.65±0.47, excluding from the average the outlier NGC1142 because it has a mass an order of magnitude larger than the others. For non-Sy galaxies is not possible compile a sensible average, because their masses spread over a wide range of values; MRK1034 NED1 has a mass of 5.36, CGCG381-051 3.8, NCG3511 0.15 and NCG7590 0.12. For the two Seyfert galaxies in common with Rigopoulou et al. (2002), NGC1365 and NGC7582, our results are in complete agreement, even though they used ISO spectra, for which the H_2 S(1) data were obtained throught an aperture of 14"×27", that is 7 times larger than the aperture of SH. This implies that the H_2 emission is concentrated in the inner $\sim 50"^2$ of these two large (several arcminutes in diameter) galaxies.

In figure 3a,b we present the H_2 flux vs PAH flux and the H_2 luminosity vs PAH luminosity. We confirm the results of Paper I with our new classification: there are no differing trends which could discriminate between AGN 1 and AGN 2.

4.2. *Source extendedness*

The SH and LH spectra overlap in the range 17-19μm, allowing us to form an estimate of the extendedness of the sources called R, the ratio of the flux measured in LH to the flux measured in SH in an adjacent spectral interval. This parameter can be defined only for sources after an appropriate background subtraction. We refer to Paper I for the details. The flux densities measured at 19μm in SH and those at 19.5μm in LH are reported in Tab. 5, with the R ratio and the corresponding extendedness class (see Paper I). We report the average extendedness factors in the classification table (Tab. 6), for each class of galaxies and also for the group of "20μm peakers". Both SH and LH spectra were already corrected for light lost outside the slits, assuming a point source: this correction takes into account the increasing size of the PSF as wavelength increases from the blue to the red end of each spectrum. In order to better understand the validity of the spectroscopic extendedness ratio R, we analyzed Spitzer direct images of four compact (R∼1) sources taken with IRAC at 8μm and MIPS at 24μm. We measured in these images the fluxes through the same apertures as observed by IRS in SH and in LH, flux-corrected with the prescriptions of the SSC for point-sources. The mean extendedness of these four sources measured through IRS is $< R >_{IRS} = 1.00 \pm 0.01$, while for IRAC at 8$\mu$m and MIPS at 24$\mu m$ are respectively $< R >_{IRAC} = 1.00 \pm 0.03$ and $< R >_{MIPS} = 1.02 \pm 0.06$. Therefore the IRS estimate of the extendedness is reliable for compact sources. We have also attempted an analogous test on the extended sources, although this estimate has serious limitations because the aperture corrections to photometry of extended sources are not well defined for IRAC[7] and MIPS. We find that, using both IRAC at 8μm and MIPS at 24μm, the extendedness classes we have defined are reproduced for our sources, although there are some differences in individual values. This implies a broad agreement among the IRS, IRAC at 8μm and MIPS at 24μm measurements of the extendedness. A paper with the analysis of the IRAC four channels and MIPS at 24μm images of the Seyfert galaxies of our sample is in preparation.

5. AGN DIAGNOSTIC DIAGRAMS: DATA AND MODELS

One of our aims is to develop a method to disentangle the contributions of the AGN and the Starburst to the total infrared emission of the Seyfert galaxies of our sample using mid-infrared spectral features. In this section we use the diagnostic diagrams, together with semianalytic models, to estimate for the sample galaxies the AGN contribution, e.g. through the [NeV] to [NeII] line ratio, and the star formation contribution, e.g. with the equivalent widths of the 11.25μm PAH feature and of the [NeII] emission line, and to search for differences between AGN 1's compared with AGN 2's.

To estimate the percentage of the contribution of the AGN and the Starburst to the observed emission of a galaxy at 19μm, we computed a mathematically simple analytic model to describe both the emission due to the AGN and that due the star formation in each of the following observed quantities: the extendedness of the source, the equivalent widths of the PAH at 11.25μm and of the [NeII] line at 12.81μm, the line ratios [NeV]14.32μm/[NeII]12.81μm and [OIV]25.89μm/[NeII]12.81μm and the spectral index α at (60-25)μm. We constructed analytic models for

---

[7] For IRAC, see: http://ssc.spitzer.caltech.edu/irac/calib/extcal/index.html

these quantities, because they provide the best separation of emission from AGN and non-AGN, and therefore the best estimates of the AGN percentage contribution to the total mid-infrared emission at 19*μm*. The simple equations for each of the models are given in the Appendix C. In the following plots of those quantities, we compare the observations with the semi-analytic models, which are plotted with solid lines.

5.1. *Line ratios versus PAH equivalent widths*

In Fig.4a the line ratio [NeV]14.32μm/[NeII]12.82μm is shown as a function of the equivalent width of the PAH feature at 11.25μm. This ratio is the best AGN tracer in the IRS wavelength range, because [NeV] can be excited only by the AGN ionizing continuum. Its ratio to [NeII]12.82μm is not directly affected by abundances. 76% of the AGN 1's have an absolute value of the EW of the PAH at 11.25μm of $|EWPAH| < 0.14\mu$m and a neon ratio [NeV]/[NeII] > 0.15. On the other hand, 87% of non-Sy and non-bona fide Sy1 have $|EWPAH| > 0.14\mu$m and [NeV]/[NeII] < 0.5. AGN 2's (i.e. non-HBLR) show a wide range of both the EW of the PAH and of the neon line ratio. Fig.4b shows a similar diagram with the PAH EW vs [OIV]/[NeII] line ratio. This diagram presents the same characteristics of the former, but with fewer upper limits, confirming its results. There is a Sy1, NGC7213, that has not been detected in the [OIV] line and has been reported to be at an intermediate stage between LINER and Seyfert (Starling et al. 2005).

Both the diagrams of Fig.4 show semi-analytic models which reproduce the empirical data and estimate the percentage of the AGN and the starburst contributions to the total infrared emission at 19*μm*. If we define as an *Seyfert-dominated* galaxy any of the sources with an AGN contribution equal or more than 50% (see the dashed lines in the diagrams), this corresponds to a the line ratios [NeV]/[NeII] > 0.054 and [OIV]/[NeII] > 0.28. Using this simple argument, we confirm that all the AGN 2's (non-HBLR's) are Seyfert-dominated, even if they span a wide range of AGN percentage in the diagnostic diagrams. We report in the Table 6 the average PAH EW and [NeV]/[NeII] ratio for each class of galaxies.

Also the diagrams PAH EW vs [NeV]14.32μm/[SiII]34.8μm and PAH EW vs [NeIII]15.55μm/[NeII]12.82μm, presented in Fig.5a,b, show similar characteristics as the previous two: the line ratio increases when the PAH EW decreases. All these diagrams (Figs.4, 5) show the general inverse relation between the AGN dominance, as measured from the ionization sensitive line ratios, and the star formation dominance, estimated from the PAH EW.

5.2. *Line ratios as density indicators*

In the IRS high-resolution spectral range, there are two fine structure line doublets, from which the electron density can be derived. These are [NeV] at 14.32μm and 24.31μm and [SIII] at 18.71μm and 33.48μm. Following Dudik et al. (2007), as already reported in paper I, we present the diagram of the neon doublet ratio versus the sulfur doublet ratio in Fig.6. In the diagram are shown the low-density limits for both line ratios and the estimated electron density as calculated by Dudik et al. (2007) assuming a temperature $T = 10^4$K. The sulfur doublet ratio has been computed correcting the flux of the [SIII]18.71μm taken throught the smaller aperture SH, multiplying it by its extendedness factor (see Table 5) to be compared with the larger aperture LH. If the ratio of two lines of the same species is below the low density limit, either there is extinction that preferentially reduces the flux of the shorter wavelength transition, and/or the assumed temperature is wrong, and these doublet ratios could not be used to measure the electron density.

We find that 34% of the AGN1's lie under the neon ratio low density limit and 15% under the sulfur low density limit, and that 30% of the AGN2's lie under the sulfur limit and 30% under the neon's. Our current sample is much larger than that of Paper 1, making these results statistically significant.

Taken at face value, these diagrams indicate low electron densities ($10^{(3-4)}$ cm^{-3}) in the [NeV] emitting region. For a typical ionizing luminosity of 10^{43} erg s^{-1} and an ionization parameter of 10^{-2}, this implies a characteristic radius of about 100 parsecs. Since the recombination time is long, for densities of $10^{(3-4)}$ cm^{-3} it ranges from 10-100 years[8], 'fossil' NLR emission will continue to be detectable in AGN 2 which could have 'shut down' production of ionizing photons for the last 300 years. We suspect this may be the explanation of many of the 'pure Seyfert 2' members of our AGN 2 class.

Thus a significant percentage of each of the Seyfert types falls under the low-density limit for either one or the other doublet, therefore, at least for the galaxies whose line ratio(s) are below the limit, we cannot estimate correctly the electron densities. However all the objects are below the low density limit only in one line ratio and not in the other line ratio. If extinction were responsible, both ratios would show this effect. We do not have any explanation for this unexpected behaviour and the possibility that some currently adopted atomic parameters for these lines (transition probabilities and/or collision strengths) might be inaccurate must be considered.

In Fig.7a we show the [SIII] doublet ratio as a function of the [SIV]10.51μm/[SiII]34.8μm ratio, with the [SIII]18.71μm flux corrected for the extendedness factor (cf Sec. 4.2). These lines are produced either in the narrow-line regions of the active nuclei or in the HII regions. In Fig.7b the [NeV] doublet ratio as function of the [NeV]14.32μm/[NeII]12.82μm line ratio is given. Figures 7a and b show no differences in the density-sensitive line ratios between the different Seyfert populations.

5.3. *Ionization Diagrams*

[NeV]14.32*μm* and [OIV]25.89*μm* are the best AGN tracers in the high-resolution IRS spectra. We normalized them both to the [NeII]12.81*μm*, that is mainly produced in the HII/star-forming regions, to produce two ionization-sensitive ratios (in Fig.8a). All the sources lie along the same sequence. As expected, the AGN 1's occupy the highest ionization region of the diagram as in the other diagrams. Most AGN 2's lie in the same region of the AGN 1's. This diagram can be used to estimate the ionizing power in the NLR, both in AGN 1 and AGN 2 objects. As mentioned above, we computed a semi-

---

[8] A typical recombination time is $\tau_r \sim 10^5/n_e$ years (Osterbrock & Ferland 2006)

analytic model to reproduce the data in this diagram. We choose as the threshold to consider a source as an Seyfert-dominated AGN again a 50% AGN contribution to the $19\mu m$ continuum, and this includes all the AGN 1's and all the detected AGN 2's. A clear implication is that using optical spectroscopy to identify Seyfert nuclei, as we have done in the 12MGS, will systematically miss out a significant population of non-HBLR Seyfert 2's (weak AGN 2's) which have less than 50% AGN contributions to their infrared emission at $19\mu m$.

Veilleux et al. (2009) present the same diagram for their sample of ULIRGs belonging to the QUEST survey, and compute a model to estimate the AGN and starburst contributions to the total emission. Their values of the line ratios are in the same range as ours. However, the percentage of AGN contribution they estimate is on average lower than the percentage we compute. This difference is likely due to the different populations of the samples. In fact ULIRGs have a stronger starburst component than Seyfert's and/or more heavily obscured AGN emission, even in the mid-infrared.

5.4. *Line Equivalent Width Diagnostics*

The line equivalent widths can also be used to estimate the contributions of the AGN and the starburst to the total galaxy emission. Since the original IRAS studies of Seyfert galaxies (Spinoglio & Malkan 1989; Rush, Malkan & Spinoglio 1993; Spinoglio et al. 1995; Spinoglio, Andreani & Malkan 2002), we have known that the mid-IR continuum can be dominated by the AGN continuum (e.g. from 12μm to 25μm), while at longer wavelengths the continuum due to the galactic disk and reprocessed thermal emission from dust around the young stellar populations increases, and it dominates the total emission at wavelenghts of 60-100μm. Therefore the equivalent widths of emission lines in the mid-IR are differently affected by the underlying continuum, as a function of the wavelength: around 12μm the EW will be more depressed by the strong AGN continuum, than they would be around 25μm. The lines originating in the galactic disk and its star-forming regions, such as [NeII]12.8μm and the H_2 S(1) at 17.02μm, will have a smaller equivalent width in objects with a stronger AGN continuum, while the lines tracing the AGN, like [NeV]14.32μm and the [OIV]25.89μm will not suffer this depression because they are enhanced in proportion to the strength itself of the AGN, keeping their equivalent widths more constant.

In our analysis of the equivalent widths, we consider only objects for which an accurate measurement of the continuumm was possible through background subtraction and with detected lines, neglecting the ones with upper limits. The equivalent width of the [NeII]$12.81\mu m$, the [NeV]$14.32\mu m$, the [NeIII]$15.55\mu m$, the [OIV]$25.89\mu m$ and H_2 $17.02\mu m$ are reported in the Tab.7.

We present in Fig.8b the PAH EW as a function of the [NeII]12.82μm equivalent width. This diagram is able to disentangle Seyfert-dominated AGN from starbursts. Comparing it with our semi-analytic model, we find that almost all the sources lie in the region of AGN contribution greater than 50%. We further find all the AGN 1's and 50% of the AGN 2's lie in the region with the modelled AGN contribution $\geq$75%, i.e. for |EW [NeII]| < 0.08. The likely explanation is that both the HII regions/star-formation tracers– [NeII] and PAH–happen to have wavelengths in a continuum range that can be strongly enhanced by the presence of an AGN contribution. The brighter the nuclear AGN continuum, the smaller the equivalent width of the spectral feature, as can be seen in the average spectra of the different populations of Fig.14 in §7.1. We report in table 6 the [NeII]EW for each class of galaxies.

We computed a mean PAH EW at $11.25\mu m$ for the AGN 1 of $<$ |PAH EW| $>$ = 0.17 ± 0.20 (Seyfert 1: 0.17 ± 0.21 and HBLR: 0.16 ± 0.19), and for the AGN 2 $<$ |PAH EW| $>$ = 0.34 ± 0.28. Wu et al. (2009) find, for the 55 objects that are in common, a similar mean PAH EW at $11.25\mu m$. From their data, we calculated for the AGN 1 class $<$ |PAH EW| $>$ = 0.19 ± 0.20 (Seyfert 1: 0.20 ± 0.20 and HBLR: 0.17 ± 0.21), and for the AGN 2 $<$ |PAH EW| $>$ = 0.43 ± 0.27. For the detailed comparison between ours and their data, we refer to Appendix D.

Using a Kolmogorov-Smirnov test, we derive that the probability that the two kind of AGN 1's– the Seyfert 1's and the HBLR-Seyfert 2's– belong to the same family is 78%. Applying the same test to the Sy 1 and the AGN 2 or to the HBLR-Sy2's and the AGN 2, results in both cases in a probability of less then 1% that the two groups are drawn from the same population. This reinforces our hypothesis that the HBLR belong with the Sy1, not the other Sy2s. We will further discuss this topic in Par.7.

5.4.1. *Line equivalent width, extendedness factor and far-IR slope*

We present in Figures 9 - 10 the extendedness versus the equivalent widths of 11.25μm PAH, [NeII]12.8μm, and [NeIII]15.5μm, respectively. The galaxies with the largest extendedness, which we define as class III, namely NGC1056, NGC1142, NGC1667 and NGC5005, are the ones with the largest equivalent widths of the PAH at 11.25μm and of the [NeII]12.8μm. These emission features are generated principally in the interstellar medium and in the HII regions of the galaxies, but not much from their active nuclei. Among these four galaxies, NGC1056 and NGC5005 have no detected [NeV] lines, and are reclassified as non-Sy (see tables 1 and 2); NGC1142, NGC1667 are AGN 2. Including the galaxies of Paper I, among the galaxies of class III there is also a non-BLR, NGC4602, and a Sy1, NGC4748. We find the same trend as in Paper I, that with increasing size of the 19μm emitting region, both the PAH and [NeII] equivalent widths increase. That is, in these diagrams AGN 1's occupy the region where the point sources lie. In contrast the non-Sy's with a measured extendedness, occupy the region of significantly extended sources with large PAH or [NeII] equivalent widths. This separation works properly in the diagrams of extendedness vs PAH EW and extendedness vs [NeII] EW, shown in Figg.9a and b. In fact just 1 of 23 Sy 1's and 2 out of 17 HBLR's do not lie in the "AGN 1 region", with extendedness $\leq$1.3. But 2/3 of the non-Sy have extendedness $\geq$1.3. AGN 2 split almost equally in the two regions: 8 of 18 lie in the AGN 1 region and 10 in the other.

Comparing the diagrams of the extendedness versus EW PAH and versus EW [NeII] with our semi-analytic model, we find that these diagrams do separate the

Seyfert-dominated AGN from Starburst-dominated ones: a modelled AGN contribution greater than 75% corresponds to |EW PAH| $\leq$0.4μm and |EW [NeII]| $\leq$0.08μm.

The diagram of [NeIII] equivalent widths versus the 19μm source extendedness (Fig.9) shows a similar trend of the figure with [NeII], but with a much higher scatter. On the contrary, the diagrams of the [NeV] and [OIV] equivalent widths versus the 19μm source extendedness (that we do not show) do not show any clear trend. This confirms that the high-ionization lines are almost totally produced in the active nuclei with no significant contribution from in extended regions. [NeIII] is an intermediate case, with contributions from both the Seyfert nucleus and also the extended star-forming regions.

The IRAS 12μm luminosity and the [NeV]14.32μm/[NeII]12.82μm line ratio are not correlated for any Seyfert type (see Fig.11), confirming the finding of Paper I. We notice that high-luminosity objects, e.g. those with $L_{12\mu m} > 10^{44} ergs^{-1}$, have the ratio [NeV]14.32μm/[NeII]12.82μm $>$ 0.2, i.e. are AGN-dominated. Fig.12a,b shows the diagrams of [NeV]14.32μm/[NeII]12.82μm and [NeIII]15.55μm/[NeII]12.82μm vs (60-25)μm spectral index. In both diagrams AGN 1's lie in the upper right region, with [NeV]/[NeII] $>$ 0.05 and [NeIII]/[NeII] $>$ 0.1, and the spectral index $\alpha_{60-25} > -2.2$. The non-Sy's cluster in a region [NeV]/[NeII] $<$ 0.2 and [NeIII]/[NeII] $<$ 0.5, with a steeper spectral index, $\alpha_{60-25} < -1.2$. AGN2 lie across both the regions. The average spectral indices are given in table 6.

5.5. *The AGN and starburst contribution to the 19μm flux*

By inverting the semi-analytic models, i.e. solving the analytical expressions with the true values of the observed quantities, we obtained a value of $\Re$, defined as starburst to AGN continuum ratio at 19μm (see Appendix C) for each of the five observed quantities of every source. We then computed the mean value of $\Re$ to estimate the relative percentage of AGN and Starburst emissions. From the value of $\Re$ we computed in Tab.8 the percentages of the Starburst and of the AGN emission. When, for a particular source, the scatter is greater than half of the mean and is due to a single $\Re$ value of one of the models, which does not describe that source because of a noisy detection, we removed that discrepant value of $\Re$ and recomputed the mean. The sample of sources to which we apply this analysis is reduced from the observed sample of 89 because the models depend on the extendedness and the PAH equivalent width, which are not always detected (for the PAH) or measurable (for the extendedness). We found that the model can disentangle the AGN and the Starburst emission for 31 AGN1 (17 bona fide Sy1's and 14 HBLR), 3 non-BLR, 15 AGN 2's and 9 objects re-classified as non-Seyferts. As can be seen from the histogram in Fig.13 Sy1's have a mean AGN contribution at 19μm of 92% $\pm$ 6%; HBLR's 92% $\pm$ 8%; AGN's 79% $\pm$ 16%, non-Sy's 69% $\pm$ 16%, and non-BLR's 62%$\pm$7%. These average percentages are also given in table 6. It is perhaps an uncomfortable surprise that up to *half* of the 19μm continuum in the IRS slit can come from a normal AGN, but still not be strong enough to make it unambiguously classified as an AGN from spectroscopy. As discussed below, this has lead to substantial confusion in the literature when Seyfert "AGN" are discussed and compared, using different selection observations.

The differences that we find between the AGN 1 and the AGN 2, (even if the latter cannot be considered from our data as an homogeneous population), i.e. the lower ionization ratios, the increased PAH and [NeII] EQW, the extendedness of the 19μm emission, can all be related to a weaker strength of the AGN component with respect to the starburst component. As a matter of fact, all our AGN 2's have evidence of an AGN both in the optical (as seen in their optical line ratios in the BPT diagrams (Baldwin, Phillips & Terlevich 1981), where we have used the optical spectral observations of Rodriguez, Malkan & Spinoglio (2009)) and also in the hard X-rays, at 2-10keV (Shu et al. 2007; Malizia et al. 2007; Bianchi et al. 2005), 2-8keV (Cardamone, Moran & Kay 2007), 15-136keV (Deluit 2004) or 40-100keV (Bird et al. 2008).

5.6. *Line equivalent widths for the different AGN types*

The average equivalent width of the fine structure lines in the various AGN classes will change depending on whether the line emission, and also the underlying continuum, is dominated by the nonstellar nucleus or the hot stars. Thus the equivalent width of [NeV]14.32μm is the same for AGN 1's: 0.020$\pm$0.021 and AGN 2's: 0.025$\pm$0.010μm, because both the line and the underlying continuum emission are proportional to the luminosity of the AGN component. The EW drops in non-Seyfert galaxies because of the complete cutoff of [NeV] emission–it is detected in two non-Seyfert galaxies which are classified as LINER (see Appendix A), but measured only in NGC7130, for which we have an off-source measurement.

The [OIV] EW decreases somewhat because the underlying continuum has a larger starburst contribution passing from AGN1 to non-Sy, in fact the [OIV] EW of the AGN1 is 0.116$\pm$0.134μm, of the AGN2 is 0.093$\pm$0.054μm and of the non-Seyfert galaxies: 0.033$\pm$0.035μm. In contrast, the [NeII] and the H_2 equivalent widths increase for the same sequence of objects, that is [NeII] EW for the AGN1 is 0.028$\pm$0.026μm, for the AGN2 it is 0.081$\pm$0.057μm, for the non-Seyfert galaxies it is 0.116$\pm$0.029μm and the average EQW H_2 is a factor ten greater in the non-HBLR's and the normal galaxies than in Sy1's and HBLR's (AGN1: 0.009$\pm$0.008μm; AGN2: 0.046$\pm$0.069μm; normal galaxies: 0.058$\pm$0.062μm). These trends are summarized in the 'classification table' given in Table 6.

6. [NEV] AS INDICATOR OF AGN ACTIVITY

Because of the very high ionization potential of NeV, we consider it as the best emission feature to distinguish active galaxies from starburst galaxies. Strong starburst activity could possibly excite some high-ionization lines such as [OIV]25.89μm (Lutz et al 1998), but the ionizing spectrum of O and B stars is not hard enough to produce much Ne^{4+}. Shocks would need to have exceptionally high velocities. Among the 91 sources we analyzed here and in Paper I classified as Seyfert galaxies, 16 objects have no [NeV] emission. As already mentioned in Sec.2, 10 (NGC1056, MCG+00-23-029, NGC5005, NGC6810, CGCG381-051, MCG-03-34-063, NCG7496, NCG7590,NGC3511 and MRK1034 NED01) of these 16 galaxies have already been reclassified as LINER, HII or starburst galaxies by Tran (2001) and Tran (2003). 4 are Sy1's: NGC1097 and NGC2639 lie in the HII region area of the BPT diagram based on [NII]6584Å/Hα vs [OIII]5007Å/Hβ (Baldwin, Phillips & Terlevich 1981); NGC7213, which also lacks the [OIV] line detection and has been classified as intermediate between LINER and Seyfert (Starling et al. 2005). The other undetected sources are the AGN 2 NGC4501 and MRK938, which also lack a detectable [OIV] line.

In contrast, two of the non-Sy's show [NeV]14.32μm emission: NGC4922 and NGC7130 are LINERs, whose active nuclei can produce highly photo-ionized gas emission (Dudik, Satyapal & Marcu 2009). There are also 4 sources with detections of [NeV] at 14.32μm but not 24.31μm. Nevertheless we consider them as [NeV] emitters, even if not detected at 24.31μm, because the noise of LH is greater than the noise of SH.

In conclusion, we can consider the [NeV] emission lines as a strong indicator for a galaxy to be classified as an AGN. In fact it is detected in 88% of the AGN 1's, 90% of the AGN 2's, only the 17% of the non-Sy's. This means that deep spectroscopic searches, e.g., for [NeV]14μm, can discover relatively weaker AGN with lower luminosities, which only produce less than 45% of the total 19μm emission observed.

Thus our infrared classification of galactic nuclei turns out to be in very close agreement to the classifications of them originally made from optical spectroscopy. The 12MGS AGN sample, which is originally defined based on optical spectra, does not contain very heavily obscured ("buried") Seyfert nuclei, more or less by definition. Deep searches for [NeV]14μm emission in the remaining "non-Seyfert" members of 12MGS would be required to find out how common buried Seyferts are. A first step has recently been taken by (Goulding & Alexander 2009), who uncovered a significant fraction of [NeV]-emitting luminous infrared galaxies whose Seyfert nuclei had been missed by previous optical spectroscopy, due to lack of sensitivity and heavy dust reddening.

7. AGN 1 STATISTICS

We give in Tab.9 the probabilities P that the two AGN1 sub-populations, the Sy1's and the HBLR Sy2's, do not differ significantly from one another, for each of the observed quantities. To derive those probabilieties we used a Kolmogorov-Smirnov test, which calculates the probability of two sets of data values arising from the same intrinsic distribution. The higher the probability, the closer are the two sets of data. We have grouped similar diagrams together to derive an average probability $< P >$, with its standard deviation. For the first group of the relations combining fine structure line ratios with PAH equivalent width (EW PAH vs [NeV]/[NeII], vs [NeIII]/[NeII], vs [OIV]/[NeII], vs [NeV]/[SiII]), we obtain $< P > = 73\% \pm 31\%$ that the AGN1 populations–Sy 1's and HBLR Sy2's–belong in the same class. For the second group, relations of the extendedness vs the equivalent width of the [NeII], [NeIII], [OIV], PAH we find $< P > = 71\% \pm 12\%$. For the the relations between the H_2 S(1) line and the PAH flux and luminosity we obtain $< P > = 77\% \pm 2\%$. Grouping together the relations between the neon ratios ([NeV]/[NeII] and [NeIII]/[NeII]) vs the spectral index at (60-25)μm, gives $< P > = 99\% \pm 2\%$. A probability of P = 78% is obtained using the diagrams EW [NeII] vs EW PAH and ([NeV]/[NeII]. The high probabilities obtained strengthen our classification which joins both Sy 1's and HBLR's as members of a single AGN 1 category. We computed the same statistical tests to calculate the probability that the Sy1 and AGN2 or HBLR and AGN2 objects belong to the same family. Both of these probabilities are on average lower. The indistinguishability between Sy 1's and HBLR has been also verified by plotting the average of the spectra of all AGN1's with an AGN percentage greater than 95%, and the average spectrum of those AGN1's with an AGN percentage below that value. The resulting plot in Figure 14 looks almost identical to the plot with the average spectra of Sy 1's and HBLR's.

7.1. *Average Spectra for each class*

To study representative spectral features of all classes of galaxies in our sample, and provide templates useful for comparisons and predictions of high-redshift galaxy populations, we computed the average spectrum of each of the classes normalized to the flux at 27μm. All the normalized average spectra are presented together in Fig.14, and are available electronically. They are compared to the average spectrum of a sample of starburst galaxies from the IRS high resolution data by Bernard-Salas et al. (2009).

The slopes of the continua of the average spectra are steepest in starburst and non Seyfert's and in AGN 2, with spectral indices[9] (10-35)μm of -2.88, -2.25 and -1.65, respectively. We cannot fit the continuum of the bona fide Sy1's and the HBLR with a single power-law. Instead we must distinguish the (10-18)μm and the (18-35)μm continuum slopes. The shorter wavelength range in the bona fide Sy1's has a spectral index of the averaged spectra of -1.21 and for the HBLR of -1.95, while the longer wavelength range has continuum spectral indexes of -0.65 and -0.90, respectively.

Wu et al. (2009) find an average spectral index of the Seyfert 1's to be -0.85±0.61 and of the Seyfert 2's to be -1.53±0.84, quite similar to the original findings based on IRAS data of Edelson & Malkan (1986).

Fig.14 shows a clear sequence. The highly ionized lines, such as [SIV], [NeV] and [OIV] are intense in the mean spectra of the Seyfert 1's, HBLR Sy 2's, and AGN 2s. The PAH feature is stronger in starburst galaxies, non Seyfert's and AGN 2, and is weaker in AGN 1. Thus, going from Seyfert-dominated to starburst-dominated objects, the continua steepen from AGN 1 to AGN 2 to non-Seyfert's and starbursts, the higher ionization lines decrease not only in their flux, but also in their equivalent widths (see §5.6), while the PAH feature remains almost constant in flux, while its equivalent width increases. It seems therefore that the PAH grains do survive in the highly ionized medium of AGNs, however they appear weaker in the most powerful ones, because they are masked by the strong underlying AGN continuum. The H_2 S(1) line has a behavior similar to the PAH, and in fact its equivalent width increases with decreasing AGN activity (see §5.6) . The presence of a BLR is closely correlated with strong thermal continuum from hot dust grains which emit around 10μm.

---

[9] We define as spectral index $\alpha = \frac{dlog(F_\nu)}{dlog(\nu)}$.

7.2. *Line Luminosity Functions*

From our statistically complete sample of galaxies, we are able to compute the first infrared line luminosity functions for Seyfert 1's and Seyfert 2's. The 12MGS includes 53 Seyfert 1's and 63 Seyfert 2's, but only 42 Seyfert 1's and 50 Seyfert 2's have been observed by IRS, therefore we have to correct the luminosity function for completeness. Tab.10 gives the luminosity functions for Seyfert 1's and Seyfert 2's, for several of the bright emission lines. In Figg.15-20 the luminosity functions of the [SIV], [NeII], [NeV]14.32μm, [NeIII], [SIII]18.71μm, [NeV]24.31μm, [OIV], [SIII]33.5μm, [SiII], H_2 17.04μm and PAH 11.25μm are shown. All the fine structure lines have a luminosity in the range 10^{39}-10^{43} erg sec^{-1} and the corresponding space densities range from 2×10^{-4} to 10^{-9} Mpc^{-3}, while the H_2 rotational line and the PAH 11.25μm feature have luminosities from 10^{38} to 10^{42} and from 10^{37} to 10^{41} respectively.

We do not find any significant difference in the line LFs of Seyfert 1's and Seyfert 2's, which are indistinguishable at the 2σ level. We also computed the line luminosity functions separately for the AGN 1's and the AGN 2's, using our new classification, and find no differences, probably because the shift of the 20 HBLR from the Seyfert 2's class into the new AGN 1 class has not a noticeable (statistical) effect on the new AGN 1 luminosity functions, while it increases the uncertainties in the AGN 2 luminosity function. We do not present the luminosity functions with the new classification, because the AGN 1 sample size is 53 but the AGN 2 sample is only 21, making the statistics of these latter quite poor.

Our sample includes all the galaxies selected at 12μm that show evidence of Seyfert activity through optical spectroscopy. We are aware that some AGN activity can be detected in the mid-IR in optically unidentified AGN. Goulding & Alexander (2009), using a volume limited sample to D< 15Mpc, find that $\sim$ 50% of the AGN they detect are not identified using optical spectroscopy. However, these objects are typically starburst dominated systems hosting modest AGN activity and have low luminosities. The luminosity of the [NeV]14.32μm emission line measured in these galaxies is about 10^{37-39}erg/sec, which is too low to affect our luminosity function (see Fig. 16a).

8. THE ACCRETION POWER IN THE LOCAL UNIVERSE

Because the [NeV]14.3μm line is uniquely generated by the accretion process through the ionizing continuum of the central engine, its luminosity function can be used to measure the accretion power in the Local Universe. The first step is to determine the correlation between the luminosity in this line and the 19μm continuum luminosity that we measured in 59 of our Seyfert galaxies (see Table 8). This relation is:

$$LogL_{19\mu m}^{AGN} = 0.9667 \times LogL([NeV]14.32\mu m) + 4.3263$$

and is shown in Fig. 21a, for each of the galaxies detected in the [NeV]14.32μm line and for which we have a measure of the AGN component. We can use this relation to convert the [NeV]14.32μm line luminosity function, of the whole set of galaxies measured in this line, into a 19μm AGN luminosity function. We present this latter in Fig. 21b. The integration over all luminosities and over the volume defined by the average redshift of the 12MSG of z=0.030 (RMS) gives a measure of the accretion power in the local universe at 19μm of 2.1 × 10^{46} erg s^{-1}.

If we want to convert this monochromatic power at 19μm into the bolometric power due to accretion, we simply use the relations between the bolometric luminosity and the infrared luminosities published in Spinoglio et al. (1995). Taking the typical spectral index for Seyfert galaxies $\alpha(12 - 19\mu m)$ = -1 and the 12μm vs bolometric luminosity correlation, we find a bolometric power of accretion of 8.0 × 10^{46} erg s^{-1}, over the local volume out to z=0.03. We are well aware that the relation between 12μm and bolometric luminosity has been derived from large-beam (few arcminutes square) IRAS data, however both quantities are affected by possible extended emission in an analogous way. Moreover all the Seyferts are dominated by AGN emission, which is almost point-like. In any case, a better estimate of the bolometric correction will be done using the nuclear fluxes of the 12MSG that we are planning to measure through the Spitzer IRAC and MIPS images (Spinoglio et al. 2009, in prep.).

A more serious concern is that not all of the AGN 2's now emitting [NeV] are generating accretion power right now, i.e., in this decade, even though they evidently did in some previous centuries. This is offset to some degree by the missing population of "weak" AGN 2's which are not optically classified as Seyferts because their AGN component produces less than 50% of their infrared emission currently (which we call "non-Seyfert-dominated"). The existence of these AGN 2's continues to complicate many discussions about "AGN", since they can leave and enter this category depending on details of the detection observations. But since the 14.32μm luminosities of all these AGN 2's are well below the characteristic "knee" in the luminosity function, their inclusion or exclusion should not alter the luminosity integral substantially.

We compare the derived accretion power with the power which originates in the starburst component of our Seyfert galaxies. We follow a similar procedure by using the [NeII]12.81μm vs starburst luminosity relation, as taken from the starburst percentage of the sample galaxies from Table 8:

$$LogL_{19\mu m}^{SB} = 0.9897 \times LogL([NeII]12.81\mu m) + 2.0198$$

We derive a monochromatic power at 19μm due to star formation and stellar evolution in Seyfert galaxies of 2.3 × 10^{45} erg s^{-1}, which corresponds to about 1/10 of the accretion power. This is quite reasonable, since the host galaxies of unambiguous Seyfert nuclei are only about one ninth of the 12 Micron Galaxy survey. In summary, because of their rarity, the set of galaxies we classify as AGN, namely those producing NeV line emission, generate only a few percent of the total fusion power in the local universe.

9. DISCUSSION AND CONCLUSIONS

Our large sample of Seyfert galaxies, and the accompanying spectropolarimetric classifications have improved and extended the analysis of Paper I. In the IR diagnostic diagrams presented, we find that AGN 1–defined as having broad line emission of some kind–have high values of ionization-sensitive line ratios, relative to the strength of star-formation tracers. In contrast, those galaxies we re-classify as non-Seyfert's have low ionization-sensitive line ratios and high PAH equivalent widths, and lie in the opposite regions of the diagnostic diagrams from AGN. The class of AGN 2's–those without broad lines–spread across both regions of the diagrams.

The simplest and strongest version of the AGN Unified Model requires that any differences between Seyfert 1's and Seyfert 2's should be due to the inclination angle of an obscuring structure (e.g. of a torus) with the line of sight to the observer, the Seyfert 2's being covered by the thick dust in the equator. However, in order to salvage this unification model from the results presented here, one has to explain why AGN 2's show a wider range of mid-IR properties, with similarities both to AGN 1 and the non-Seyfert's. Perhaps this could derive from the particular geometry of the "torus-BLR-scattering region": the torus in fact can absorb the radiation not only from the BLR but also from the scattering region where the polarized emission could be produced, depending, for example, from the precise inclination angle, or the intrinsic clumpiness of the torus. That is the basic suggestion of Heisler, Lumsden & Bailey (1997). However, to suppress high-ionization emission lines we observe in the IR– which are assumed to be isotropic– the absorbing structure would also need to block out a significant fraction of the ionizing photons that would otherwise illuminate the NLR, even though this does not seem to happen in Seyferts with any detectable BLR. But once additional intrinsic differences other than just the viewing angle are admitted, the attractive simplicity of ATM unification is lost.

On the contrary, however, there may be "genuine" type 2 Seyfert nuclei. These would be the half of our AGN2 category which have smaller proportions of AGN emission, and do not have analogs among the Seyfert 1s. As we discussed, the remaining NLR emission we detect in the optical and infrared spectra of these true Sy2's may be the "fossil" remnants of a 10–100 parsec extent of gas that had been ionized by an AGN which was active in previous millenia, but has been effectively "turned off" for the last several hundred years. Given their strong variability over all timescales, AGN which recently "turned off" must exist. Depending on the duty cycles of power generation through black hole accretion, they could account for up to half of our AGN2. This would then imply the existence of a comparable population of "recently turned on" AGN. These could stand out as having unusually strong broad line and near-IR continuum emission, relatively to their NLR strength. The most likely candidates for these "young" or more accurately, "rejuvenated" AGN1's are those Seyfert 1's having relatively strong FeII emission and low values of NLR/BLR ratios such as [OIII]5007/Hβ (Boroson & Green 1992). Thus it could well turn out that long-term variability is at least as important as viewing angle in unifying the various observed classes of AGN.

- The main results of this paper are as follows: We present the *Spitzer* IRS high-resolution spectra of almost 80% of the Seyfert galaxies of the 12μm galaxy sample, a total of 91 galaxies;

- We adopted a spectropolarimetric classification, with the "AGN 1" class broadly defined to include both the Seyfert 1's and the "hidden broad line Region" Seyfert 2's, as detected through optical spectropolarimetry. All of our infrared diagnostics are consistent with Sy 1's and HBLR Sy 2's belonging to the same single class. The AGN 2 class contains the remaining Seyfert 2 galaxies without polarized broad lines are likely a mixture of weaker AGN 1, in which the BLR exists but has not yet been detected, and "true" AGN 2, galaxies that may not have been producing much hard ionizing radiation for the last several hundred years. Our AGN 1/2 distinction, based solely on reddening-independent IR data, is supported by more of the data than the usual traditional classification scheme that divides the Seyfert 1's and 2's based strictly on the detectability of BLR emission in direct optical spectroscopy. It appears that the mid-IR observed properties characterize the AGN 1 as an homogeneous class of objects. The mid-IR behaviour of AGN 2's, instead, shows objects similar to AGN 1's and others more similar to non-Seyfert galaxies.

- Semi-analytic models based on the observed mid-IR spectra are effective in separating the AGN and starburst components in Seyfert galaxies. We find that for 31 AGN 1 the average AGN percentage contribution to the 19μm luminosity is 92.2±6.6%, while for 16 AGN 2 this percentage decreases to 79.3±15.7% and for 9 non-Seyfert's is 67.6±17.2%. Although with large scatter, there is a clear trend of decreasing AGN strength from AGN1 to AGN2 to non-Seyfert's. Ionization-sensitive line ratios can discriminate AGN 1's from AGN 2's and non-Seyferts. The diagnostic diagram of [NeV]/[NeII] versus [OIV]/[NeII] provides a measure of the AGN strength in both AGN 1's and AGN 2's. The AGN 2 do not appear to be a homogeneous population with respect to starburst tracers, such as the EW PAH and the EW of [NeII]. Moreover, some AGN 2 nuclei could either contain more ongoing star formation and/or be covered by more dust than any of the AGN 1's.

- The 0-0 S(1) H_2 rotational transition can be used to estimate the mass of the emitting regions. The average mass value is of the order of 10^8 $M_\odot$, which is in agreement with other estimates for Seyfert and starburst galaxies.

- The density-sensitive line ratios (the [NeV] and [SIII] doublet ratios), in about 40% of the objects imply electron densities below the low density limit. Therefore they can not be used reliably to estimate the electron density of these regions. The simple interpretation that the line emission from the NLR and the HII regions can be heavily absorbed by dust even in these mid-IR lines (Dudik et al. 2007) is not confirmed from our data because the galaxies of our sample *do not* show both line ratios affected at the same time in the same objects. In addition, the abnormally low ratios occur with the same frequency in all different types of emission line galaxies. The other possibility is that some assumed atomic physics parameters need revision for both of these line ratios.

- We derived for the first time the line luminosity functions for either classical Seyfert 1's and 2's and also for AGN 1 and AGN 2. We do not find significant differences between the various populations, in either the shape or the normalization of their line LFs.

- The mid-infrared [NeV] lines are unambiguous tracers of the AGN NLR. We therefore use the [NeV] line luminosity function of all Seyfert galaxies to estimate the accretion power in the local universe within a volume out to z=0.03. We find that the power originating from accretion at 19μm is $\sim 2 \times 10^{46}$ erg s^{-1} , about 4 times less than the bolometric power. For comparison, the power related to star formation and stellar evolution in the Seyfert galaxies population at 19μm is one tenth of that one from accretion.

This work is based on observations made with the Spitzer Space Telescope which is operated by the Jet Propulsion Laboratory and Caltech under a contract with NASA. This research has been funded in Italy by ASI under contract I/05/07/0. We benefited from helpful discussions with R. Antonucci. We especially thank Kevin Hainline for help with early stages of the data reduction, and Howard Smith and members of the IRAC team for contributing Guaranteed Time to obtaining an essential portion of these data. We thank Jeronimo Bernard-Salas for having sent us the data of the average Starburst high-resolution Spitzer spectrum. We thank the anonymous referee for the useful comments and suggestions. We thank Mrs. Erina Pizzi of IFSI-INAF for the preparation of the postscript figures of the article. This research has been funded in Italy by ASI under contract I/05/07/0 and in the U.S. by NASA contract 59586.

APPENDIX

A. CLASSIFICATION: NOTES ON INDIVIDUAL OBJECTS

NGC526A: has no detected broad lines, according to new data from Bennert et al (2006), however broad Hα wings were observed more than 20 years ago (Lawrence 2009, priv. com.). Because of the possible changes in BLR characteristics over timescaales of the order of years, we conservatively classify this object as a AGN1.

MRK1034 NED1 = Akn80: this has not a Seyfert like optical spectrum (Osterbrock & Phillips 1977). We classify it as a non-Sy (IRS spectrum in paper I).

MRK1034 NED2 = Akn81: only narrow lines, slightly wider than the instrumental resolution (Osterbrock & Phillips 1977). We classify it as a non-BLR as no polarimetric observations are available (IRS spectrum in paper I).

ESO545-G13 = MCG-03-07-011 = MBG 02223-1922: detected broad Hα and Hβ $\sim$ 2000 km/s (Coziol et al. 1993). We classify this object as an AGN1 (IRS spectrum in paper I).

NGC1056: this object has been classified as an HII region galaxy through optical spectroscopy by Veilleux et al. (1995).

NGC1097: detected broad Hα $\sim$ 10000 km/s FWHM (Storchi-Bergmann, Baldwin & Wilson 1993). On the basis of this BLR evidence, we classify this object into the AGN1 class.

NGC1194: only narrow lines were detected: Hα $\sim$230 km/s FWHM and [OIII]5007Å$\sim$400 km/s FWHM (Kirhakos & Steiner 1990). Because no polarization data are available, we classify it as a non-BLR object, but we are unable to include it in either AGN1 or AGN2 classes.

NGC1365: detected broad Hβ of 1896 km/s FWHM (Shulz et al. 1999). On the basis of the BLR evidence, we classify this object into the AGN1 class. Note: [NeV] is detected.

ESO362-G018 = MCG-05-13-017: Hβ has a witdh of 5240 $\pm$ 500 km/s FWHM, therefore is a genuine AGN1 (Bennert et al 2006).

NGC2639: detected broad Hα of 3879 km/s FWZI (Keel 1983). On the basis of the BLR evidence, we classify this object into the AGN1 class.

NGC3511: only narrow lines were detected: Hα $\sim$ 135 km/s FWHM, this galaxy is classified as HII region galaxy (Kirhakos & Steiner 1990). We classify this object as a non-Sy.

MCG+00-29-23: this object has been classified as an HII region galaxy through optical spectroscopy by Veilleux et al. (1995).

NGC4602: detected only marginal evidence for an Hα broad component with FWZI$\sim$10000 km/s (Kollatschny & Fricke 1985). We classify it as a non-BLR, as no polarimetric observations are available (IRS spectrum in paper I).

NGC4922: this object has been classified as intermediate between a LINER and an HII region galaxy through optical spectroscopy by Veilleux et al. (1995).

NGC5005: this object is classified as a LINER galaxy (Goodrich & Keel 1986; Terashima, Ho & Ptak 2000).

NGC5506: observed in spectropolarization: no broad Hα component was detected at a level of 1x10$^-$15 cgs (Lumsden et al. 2004). We classify this object as an non-HBLR, and thus AGN2.

NGC6810: this object is classified as a transition object between an HII region galaxy and an AGN, having an [OIII]$\lambda 5007\AA$ width of 304 km/s FWHM and an Hα width of 263 km/s FWHM and the following line ratios: [NII]/Hα = 0.62, [OIII]/Hβ =0.6, [SII]/Hα = 0.3 (Kirhakos & Steiner 1990). We conservatively classify it an a non-Sy.

MRK897: Rodriguez, Malkan & Spinoglio (2009) confirm the classification of this galaxy as a Seyfet 2 of Durret (1994). Because of the lack of polarization data, we classify it as a non-BLR (IRS spectrum in paper I).

NGC7130 = IC5135: this object is classified as a LINER(Veilleux et al. 1995).

NGC7314: detected in spectropolarization at Hα : F6563(broad)=5.6x10$^-$15 cgs (Lumsden et al. 2004). We classify this object as an HBLR, and thus AGN1.

NGC7496: the relative strength of the emission lines in the nucleus of this object is typical of normal photoionization found in HII regions (Pence & Blackman 1984) (IRS spectrum in paper I).

NGC7590: the relative strength of the emission lines in the nucleus of this object is typical of normal photoionization found in HII regions (Storchi-Bergmann, Kinney, & Challis 1995) (IRS spectrum in paper I).

CGCG381-051: this object has been classified as an HII region galaxy through optical spectroscopy by de Grijp et al. (1992).

B. PECULIARITIES OF THE "20μM PEAKERS"

We have considered the "20μm peakers" identified by Wu et al 2009 in section 2 and computed the average values of the discussed quantities in the classification Tab. 6. We find in our sample fifteen "20μm peakers": 11 Sy1's, 3 HBLR's and 1 AGN2. The major peculiarities of this group of objects are that: they are almost all compact at 19μm, they have very faint PAH 11.25μm emission, a flat average spectral index (60-25)μm, and low equivalent widths of the lines (see Tab. 6).

In particular, among them 11 are compact sources (belonging to the extendedness class I), 1 belongs to class II, 3 do not have background subtracted spectra and therefore no extendedness measurement. 7 of them do not show any PAH feature at 11.25 μm and the mean PAH EW 11.25 μm among the other 8 objects is -0.04±0.04μm. The mean EW of the lines and the feature in Tab. 6 are consistent with the lowest values for the AGN1. On the other hand, the AGN contribution is among the highest values in the AGN1's, as it can be seen from the mean [NeV]14.32μm/[NeII]12.81μm ratio, the mean spectral index and the average modelled AGN contribution.

C. MATHEMATICAL TREATMENT OF THE MODELS

We present here the details of the semi-analytic models. To model the observed IR quantities, we have found an analytical expression for each of them as a function of $\Re$, which is defined as the ratio of the Starburst dust continuum at 19μm to the AGN flux at the same wavelength. $\Re$ varies from zero - emission totally from the AGN - to infinity - emission totally from the Starburst.

$$\Re = \frac{F^{gal}_{19\mu m}}{F^{AGN}_{19\mu m}} \tag{C1}$$

The extendedness is defined as the ratio between the flux measured at 19.5μm from the LH slit to that measured at 19μm by the SH slit. If we define $F^{gal}_{19\mu m}$ and $F^{AGN}_{19\mu m}$ as the fluxes of galaxy and AGN, respectively, through the SH slit, considering that at maximum the LH slit can intercept 4 times the $F^{gal}_{19\mu m}$ and that $F^{AGN}_{19\mu m}$ does not depend on the slit aperture, as can be approximated to a point-like source, then: Flux(LH) = $F^{AGN}_{19\mu m} + 4 \cdot F^{gal}_{19\mu m}$; Flux(SH) = $F^{AGN}_{19\mu m} + F^{gal}_{19\mu m}$.

$$ext = \frac{F^{AGN}_{19\mu m} + 4 \cdot F^{gal}_{19\mu m}}{F^{AGN}_{19\mu m} + F^{gal}_{19\mu m}} = \frac{1 + 4 \cdot \frac{F^{gal}_{19\mu m}}{F^{AGN}_{19\mu m}}}{1 + \frac{F^{gal}_{19\mu m}}{F^{AGN}_{19\mu m}}} = \frac{1 + 4 \cdot \Re}{1 + \Re} \tag{C2}$$

We know that the PAH emission feature at 11.25μm originates in the host galaxy only, while its underlying continuum derives from both galaxy and AGN. Therefore we can predict its equivalent width as:

$$EWPAH = \frac{A_1 \cdot F^{gal}_{11.25\mu m}}{F^{gal}_{11.25\mu m} + F^{AGN}_{11.25\mu m}} \tag{C3}$$

where A_1 is a costant depending on the measured features flux and we adopt A_1=1.8 for the PAH at 11.25μm. From the assumption that we can model the continua with a power law:

$$\nu^{-\alpha} F_\nu = k \tag{C4}$$

where α is the spectral index, k is a constant. We adopt α=-1.4 for the AGN component and α=-2 for the galaxy, these values are in agreement with the values commonly used as spectral index for AGN and starburst and availble in literature (cf Edelson & Malkan (1986)). We derive the $F^{gal}_{11.25\mu m}$ and the $F^{AGN}_{11.25\mu m}$ as functions of $F^{gal}_{19\mu m}$ and $F^{AGN}_{19\mu m}$, respectively, and consequentely as functions of the free parameter $\Re$. From equations C3 and C4, the PAH EW becomes:

$$EWPAH = \frac{1.8 \cdot (\frac{k/19\mu m}{k/11.25\mu m})^{(-2+1.4)} \cdot \Re}{(\frac{k/19\mu m}{k/11.25\mu m})^{(-2+1.4)} \cdot \Re + 1} \tag{C5}$$

The [NeII] EW has contributions both from the galaxy and the AGN:

$$EW[NeII] = \frac{A_2 \cdot F^{gal}_{12.81\mu m} + B_2 \cdot F^{AGN}_{12.81\mu m}}{F^{gal}_{12.81\mu m} + F^{AGN}_{12.81\mu m}} \tag{C6}$$

Because the galaxy component is stronger than the AGN's in the [NeII] emission, we chose the constant A_2 two orders of magnitude greater than B_2, adopting A_2=0.25 and B_2=0.001.

The procedure for modeling the line ratios is similar. We modelled the emission of each single line and then we simply took their ratio:

$$[NeV]/[NeII] = \frac{A_3 \cdot F^{gal}_{14.32\mu m} + B_3 \cdot F^{AGN}_{14.32\mu m}}{A_2 \cdot F^{gal}_{12.81\mu m} + B_2 \cdot F^{AGN}_{12.81\mu m}}, \tag{C7}$$

$$[OIV]/[NeII] = \frac{A_4 \cdot F^{gal}_{25.89\mu m} + B_4 \cdot F^{AGN}_{25.89\mu m}}{A_2 \cdot F^{gal}_{12.81\mu m} + B_2 \cdot F^{AGN}_{12.81\mu m}}, \tag{C8}$$

with $A_3 = 0$ and $B_3 = 0.01$ and $A_4 = 0$ and $B_4 = 0.01$, because we consider the [NeV]14.32μm and [OIV]25.89μm lines to be produced exclusively by the AGN.

To model the $\alpha_{(60-25)\mu m}$ spectral index, we use its definition as:

$$\alpha_{(60-25)\mu m} = \frac{log(\frac{F_\nu(60\mu m)}{F_\nu(25\mu m)})}{log(\frac{\nu_{60\mu m}}{\nu_{25\mu m}})}, \tag{C9}$$

writing $F_\nu(60\mu m)$ and $F_\nu(25\mu m)$ in terms of F^{gal} and F^{AGN}, considering that $F_\nu(60\mu m)$ is due mainly to the galaxy emission, it becomes:

$$\alpha_{(60-25)\mu m} = \frac{log(\frac{F^{gal}_{60\mu m} + 0.001 F^{AGN}_{60\mu m}}{F^{gal}_{25\mu m} + F^{AGN}_{25\mu m}})}{log(\frac{\nu_{60\mu m}}{\nu_{25\mu m}})}. \tag{C10}$$

The treatment of the previous equations is the same of the EW PAH model's. All the factors A_i and B_i have been found by fitting the data with the models and they depend on the instrument (spectrograph properties, slits areas, spectral extraction methods). These same models can be suitable for other observables and instruments, by scaling those factors.

D. PAH 11.25μM EW - LOW/HIGH RESOLUTION COMPARISON

We plot in Figs. 22a and b the PAH 11.25μm EW measured by Wu et al. (2009) versus that one measured by us, to compare the results on the objects in common. In Fig. 22a we present the ratio of the values found by us to the values of Wu et al. (2009) to better show the scatter of the two sets of data. In Fig. 22b we plot the PAH 11.25μm EW by Wu et al. (2009) versus ours and we computed their least square fits, calculated the mean slopes and their confidence intervals by using the bootstrap method (by 1000 resampling). The two sets of data are consistent with each other, as it is shown by the slope of the lines reproducing the least square fits of the data: considering all the galaxy types, the slope of the fitting line is 1.14±0.17; if we consider only the AGN1 and AGN2 the slope is 0.97±0.18. These two results agree within the errors. However, the fitting line slope becomes steeper when we add the non-Sy's data, because for these we used a different method to measure the PAH emission feature at 11.25μm. Wu et al. (2009) remove the continuum underlying the range 10.80-11.80μm and integrate the PAH feature flux inside this window, in each of the sources. On the other hand, we measure the flux in the range 11.15-11.65μm for all the sources, but we subtract the continuum underlying the whole range 11.2-13.0μm for those sources having in this range a broad multicomponent feature. This results in a lower continuum baseline measure and therefore in a higher PAH feature equivalent width.

E. ADDITIONAL OBSERVATIONAL MEASUREMENTS

Weak ionic fine structure lines

Besides the ionic lines we presented in §4, the spectra of seven sources showed other fine structure lines, e.g. [ArV]13.10μm, [FeII]25.99μm and 24.81μm, [FeIII]22.95μm and 33.04μm. The [FeII]25.99μm line is often blended with the [OIV]25.89μm line, because the IRS spectral resolution is not high enough to resolve these two lines in all the objects. These seven galaxies and their respective lines fluxes are reported in Tab.12.

There are unfortunately not enough good detections of these lines in this sample to base strong statistical tests on them. We have nevertheless compared our [FeII]25.99μm detections with those of Dale et al. (2009) in the line ratio diagram of [SiII]34.8μm/[SIII]33.5μm vs [FeII]25.99μm/[NeII]12.8μm. Although the small number of points, our measurements are in agreement with theirs, as the few AGN 2's are located in the region of the Seyfert's of Dale et al. (2009) and the non-Sy are located among their normal spiral galaxies.

Full Width Half Maximum of the spectral lines

The lines FWHM are due to the velocity field of the gaseous regions where they are produced. The velocity dispersion σ of the [OIII] at 5007Å, originated in the Narrow Line Regions, is related to the black hole mass (Nelson 2000; Greene & Ho 2005). It is interesting to extend the same relation to the mid-infrared lines of [NeV] at 14.32μm, [NeV] at 24.31μm and the [OIV] at 25.89μm, because they suffer less obscuration than the optical lines and are mostly originated by the AGN activity, though the [OIV] can be contaminated by strong starburst emission.

Dasyra et al. (2008) claim to have measured resolved spectral widths of the IRS lines. The IRS resolving power for the high resolution modules is on average (500 +/- 50) km/sec along the whole spectrum. We find the FWHM of all the lines to be, within the errors, of the same value of the resolving element and to have a scatter of about the 15% of the mean value (the mean value and the standard deviation of the FWHM of all the fine structure lines are reported in Tab.13). We cannot conclude that the lines are resolved, because we consider a line to be resolved if its FWHM is significantly larger than the resolution element. While Dasyra et al. (2008) consider the instrumental velocity dispersion (the one corresponding to the resolving power of the instrument) as the ratio between resolution element and 2.35, we compare the measured FWHM with the resolution element itself, to be more conservative.

Moreover, both the typical AGN lines and those originated by starburst emission have nearly the same mean FWHM (see Tab.13), which does not change with the Seyfert or galaxy type. The AGN lines, originated from the NLR, should suffer from more broadening than the lines emitted by the galactic regions. We conclude that the broadening of the lines is not intrinsic to the gas motion, but most probably is due to instrumental effects, otherwise we would measure different widths from lines originated from the different regions.

In conclusion, we consider that the FWHM of the lines measured in the IRS spectra do not measure the dispersion velocity field in the NLR, and higher spectral resolution data would be necessary.

REFERENCES

Antonucci, R., Miller J., 1985, ApJ, 297, 621
Antonucci R., 1993, ARA&A 31, 473
Armus et al., 2007, ApJ, 656, 148
Baldwin, J.A., Phillips, M.M., Terlevich, R., 1981, PASP, 93, 5
Bennert, N., Jungwiert, B., Komossa, S., Haas M. and Chini, R. 2006, A&A, 459, 55
Bianchi, S., Guainazzi, M., Matt, G., Chiaberge, M., Iwasawa, K., Fiore, F., Maiolino, R., 2005, A&A, 442, 185
Bird et al., 2007, ApJS, 170, 175
Boroson, T. A., Green, R.F. 1992, ApJS, 80, 109
Bernard-Salas, J., Spoon et al., 2009, ApJS, 184, 230
Buchanan, C.L., Gallimore, J.F., O'Dea, C.P., Baum, S.A., Axon, D.J., Robinson, A., Elitzur, M., Elvis, M., 2006, AJ, 132, 401
Cardamone, C., Moran, E.C., Kay, L.E., 2007, AJ, 134.1263
Coziol, R., Pena, M., Demers, S., Torres-Peimbert, S. 1993, MNRAS, 261, 170
Dale, D.A. et al., 2009, ApJ, 693, 1821
Dasyra, K.M., Ho, L.C., Armus, L., Ogle, P., Helou, G., Peterson, B.M., Lutz, D., Netzer, H., Sturm, E. 2008, ApJ, 674, 9
Deluit, S.J. 2004, A&A, 415, 39
de Grijp, M.H.K., Keel, W.C., Miley, G.K., Goudfrooij, P., Lub, J. 1992, A&AS, 96, 389
Deo, R.P., Crenshaw, D.M., Kraemer, S.B., Dietrich, M., Elitzur, M., Teplitz, H., Turner, T.J., 2007, ApJ, 671, 124
Dudik, R.P., Weingartner, J. C., Satyapal, S., Fischer, J., Dudley, C. C., O'Halloran, B., 2007, ApJ, 664, 71
Dudik, R.P., Satyapal, S., Marcu, D., 2009, ApJ, 691, 1501
Durret, F. 1994, A&AS, 105, 57
Edelson, R. and Malkan, M.A., 1986, ApJ, 308, 59.
Genzel, R. et al., 1998, ApJ, 498, 579
Goodrich, R.W., Keel, W.C. 1986, ApJ, 305, 148
Gorjian, V., Cleary, K., Werner, M. W., 2007, ApJ, 655, 73
Goulding, A. and Alexander, D. 2009, astro-ph/0906.0772
Greene, J. E., Ho, L. C., 2005, AAS, 20719703
Heisler, C.A., Lumsden, S.L., Bailey, J.A., 1997, Nature, 385, 700
Higdon, S.J.U. et al., 2004, PASP, 116, 975
Higdon, S.J.U. et al., 2006, ApJ, 648, 323
Hunt, L.K., & Malkan, M.A. 1999, ApJ, 516, 660
Houck, J.R. et al., 2004, ApJS, 154, 18
Kauffmann, G. et al 2003, MNRAS, 346, 1055
Keel, W.C. 1983 ApJ, 269, 466
Kirhakos, S.D., & Steiner,J.E. 1990, AJ, 99, 1722
Kollatschny, W. and Fricke, K.J. 1985, A&A, 143, 393]
Krongold, Y., Dultzin-Hacyan, D., Marziani, P., 2002, ApJ, 572, 169
Levenson, N.A., Weaver, K.A., Heckman, T. M., 2001, ApJ, 550, 230
Lumsden, S.L., Alexander, D.M., Hough, J.H. 2004, MNRAS, 348, 1451

Lutz, D., Kunze, D., Spoon, H. W. W., Thornley, M. D. 1998, AA, 333, L75

Malizia, A. et al., 2007, ApJ, 668, 81

Malkan, M.A., Gorjian, V. and Tam, R. 1998, ApJS, 117, 25

Meléndez, M., Kraemer, S.B., Schmitt, H.R., Crenshaw, D. M., Deo, R.P., Mushotzky, R.F., Bruhweiler, F.C., 2008a, ApJ, 689, 95

Meléndez, M. et al., 2008b, ApJ, 682, 94

Moran, E.C. 2007 The Central Engine of Active Galactic Nuclei, ASP Conference Series, Vol. 373. Edited by Luis C. Ho and Jian-Min Wang, p.425

Nelson, C.H., 2000, ApJ, 544, 91

Osterbrock, D.E. & Ferland G.J., 2006, Astrophysics of gaseous nebulae and active galactic nuclei, 2nd. ed. by D.E. Osterbrock and G.J. Ferland. Sausalito, CA: University Science Books, 2, p.22

Osterbrock, D.E. & Phillips, M.M. 1977, PASP, 89, 251.

Pence, W.D., Blackman, C.P. 1984, MNRAS, 210, 547

Puget, J.-L. & Leger, A. 1989, ARA&A, 27, 161

Rieke, G. H., Lebofsky, M. J., 1985, ApJ, 288, 618

Rigopoulou, D., Kunze, D., Lutz, D., Genzel, R., & Moorwood, A.F.M. 2002, A&A, 389, 374

Rodriguez, D., Malkan M., Spinoglio, L., 2009, in preparation

Roussel, H. et al. 2007, ApJ, 669, 959

Rush, B., Malkan, M.A., & Spinoglio, L. 1993, ApJS, 89, 1

Rush, B., Malkan, M.A.; Fink, H.H., Voges, W. 1996, ApJ, 471, 190

Shu, X.W., Wang, J. X., Jiang, P., Fan, L. L., Wang, T. G., 2007, ApJ, 657, 167

Schulz, H., Komossa, S., Schmitz, C., and Mucke, A. 1999, A&A, 346, 764

Spinoglio, L. , Andreani, P. & Malkan, M.A. 2002, ApJ, 572, 105

Spinoglio, L. & Malkan, M.A. 1989, ApJ, 342, 83

Spinoglio, L. & Malkan, M.A. 1992, ApJ, 399, 504

Spinoglio, L., Malkan, M.A., Rush, B., Carrasco, L., Recillas-Cruz, E. 1995, ApJ, 453, 616

Starling, R. L. C., Page, M. J., Branduardi-Raymont, G., Breeveld, A. A., Soria, R., Wu, K., 2005, MNRAS, 356, 727

Storchi-Bergmann, T., Baldwin, J.A., Wilson, A.S. 1993, ApJ, 410, L11

Storchi-Bergmann, T., Kinney, A.L., Challis, P. 1995, ApJS, 98, 103

Storchi-Bergmann, T., González Delgado, R.M., Schmitt, H.R., Cid Fernandes, R., Heckman, T., 2001, ApJ, 559, 147

Szuszkiewicz, E., Malkan, M. A., & Abramowicz, M. A. 1996, ApJ, 458, 474

Terashima, Y., Ho, L.C., Ptak, A.F. 2000, ApJ, 539, 161

Thornley, M.D., Forster Schreiber, N.M., Lutz, D., Genzel, R., Spoon, H.W.W., Kunze, D., Sternberg, A., 2000, ApJ, 539, 641

Tommasin, S., Spinoglio, L., Malkan, M., Smith, H., González-Alfonso, E., Charmandaris, V., 2008, ApJ, 676, 836

Tran, H.D., 2001, ApJ, 554, L19

Tran, H.D., 2003, ApJ, 583, 632

Veilleux, S., Kim, D.-C., Sanders, D.B., Mazzarella, J.M., Soifer, B.T. 1995, ApJS, 98, 171

Veilleux, S., et al., 2009, ApJS, 182, 628

Véron-Cetty, M.-P.; Véron, P.; Goncalves, A. C., 2001, A&A, 372, 730

Wang, J. M. & Zhang, E. P., 2007, ApJ, 660, 1072

Weedman et al., 2005, ApJ, 633, 706

Werner, M.W. et al., 2004, ApJS, 154, 1

Wu, Y., Charmandaris, V., Jiasheng H., Spinoglio, L., Tommasin, S., 2009, ApJ, 701, 658

Zhang, E. P.,& Wang, J. M., 2006, ApJ, 653, 137

TABLE 1

Journal of Spitzer IRS observations

NAME	R.A. (J2000.0) h m s	Dec. (J2000.0) deg ' ”	type	new class.	z	$F_{12\mu m}$ (Jy)	$F_{25\mu m}$ (Jy)	Obs. Date	SH Int.time (sec.)	LH Int.time (sec.)	
MRK335	00:06:19.5	+20:12:10	Sy1		0.025785	0.27	0.45	2009/01/12	4×30	2×60	3
MRK938	00:11:06.5	-12:06:26	Sy2	non-HBLR	0.019617	0.40	2.37	2006/12/20	2×30	4×14	
MRK348	00:48:47.1	+31:57:25	Sy2	HBLR	0.015034	0.49	1.02	2007/09/01	2×30	4×14	
NGC0526A	01:23:54.4	-35:03:56	Sy1	non-BLR	0.019097	0.23	0.48	2007/08/01	6×7	4×14	2,4
IRAS01475-0740	01:50:02.7	-07:25:48	Sy2	HBLR	0.017666	0.31	0.96	2007/08/04	4×30	2×60	
NGC1056	02:42:48.3	+28:34:27	Sy2	non-Sy	0.005154	0.33	4.83	2007/09/02	4×30	2×60	
NGC1097	02:46:19.0	-30:16:30	Sy1		0.004240	2.88	7.70	2004/01/08	4×30	2×60	1,2,4
NGC1142	02:55:12.2	-00:11:01	Sy2	non-HBLR	0.028847	0.26	0.62	2006/02/02	4×120	6×60	2
MCG-02-08-039	03:00:30.6	-11:24:57	Sy2	HBLR	0.029894	0.20	0.48	2007/09/02	4×30	2×60	
NGC1194	03:03:49.1	-01:06:13	Sy1	non-BLR	0.013596	0.27	0.51	2007/08/31	4×30	2×60	4
NGC1241	03:11:14.6	-08:55:20	Sy2	non-HBLR	0.013515	0.33	0.60	2006/01/27	2×30	2×60	2
NGC1320	03:24:48.7	-03:02:32	Sy2	non-HBLR	0.008883	0.33	1.07	2007/08/31	4×30	2×60	
NGC1365	03:33:36.4	-36:08:25	Sy1		0.005457	4.42	13.07	2004/01/04	4×30	8×14	1,2,4
NGC1386	03:36:46.2	-35:59:57	Sy2	non-HBLR	0.002895	0.52	1.46	2007/09/03	5×6	2×14	2
IRAS03450+0055	03:47:40.2	+01:05:14	Sy1		0.031000	0.28	0.51	2007/09/07	4×30	2×60	
3C120	04:33:11.1	+05:21:16	Sy1		0.033010	0.43	0.67	2007/10/06	5×6	2×14	2
MRK618	04:36:22.2	-10:22:34	Sy1		0.035550	0.34	0.79	2007/10/05	2×30	4×14	
F04385-0828	04:40:54.9	-08:22:22	Sy2	HBLR	0.015100	0.43	1.62	2007/10/05	2×30	4×14	
NGC1667	04:48:37.1	-06:19:12	Sy2	non-HBLR	0.015167	0.43	0.68	2007/10/05	2×30	4×14	
ESO362-G018	05:19:35.8	-32:39:28	Sy1		0.012445	0.22	0.57	2007/03/25	4×30	2×60	4
ESO253-G3	05:25:18.1	-46:00:21	Sy2	non-HBLR	0.042489	0.26	0.97	2007/03/25	4×30	2×60	
F05563-3820	05:58:02.0	-38:20:05	Sy1		0.033870	0.64	0.77	2007/10/06	4×30	2×60	2
MRK79	07:42:32.8	+49:48:35	Sy1		0.022189	0.31	0.76	2006/11/17	2×30	4×14	
NGC2639	08:43:38.1	+50:12:20	Sy1		0.011128	0.24	0.27	2005/04/15	2×30	2×60	1,2,4
MRK704	09:18:26.0	+16:18:19	Sy1		0.029234	0.35	0.53	2007/05/04	2×30	4×14	
MRK1239	09:52:19.1	-01:36:43	Sy1		0.019927	0.76	1.21	2006/12/19	2×120	2×60	2
3C234	10:01:49.5	+28:47:09	Sy1		0.184800	0.16	0.26	2007/06/08	4×30	2×60	
NGC3511	11:03:23.8	-23:05:12	Sy1	non-Sy	0.003699	1.03	0.85	2005/05/25	8×30	4×60	1,2,4
MCG+00-29-023	11:21:12.2	-02:59:03	Sy2	non-Sy	0.024897	0.48	0.68	2005/05/25	2×120	6×60	1,2
NGC3982	11:56:28.1	+55:07:31	Sy2	non-HBLR	0.003699	0.51	0.83	2006/12/22	2×30	4×14	
NGC4051	12:03:09.6	+44:31:53	Sy1		0.002336	1.37	2.28	2005/06/01	8×30	4×60	1,2
MRK766	12:18:26.5	+29:48:46	Sy1		0.012929	0.35	1.47	2006/06/22	2×120	2×60	2
NGC4388	12:25:46.7	+12:39:44	Sy2	HBLR	0.008419	1.03	3.72	2007/06/12	5×6	2×14	2
NGC4593	12:39:39.4	-05:20:39	Sy1		0.009000	0.47	0.96	2005/07/01	4×30	2×60	1,2
NGC4922	13:01:24.9	+29:18:40	Sy2	non-Sy	0.023586	0.31	1.52	2005/01/10	6×30	2×60	1,2
NGC4941	13:04:13.1	-05:33:06	Sy2	non-HBLR	0.003696	0.39	0.46	2007/07/31	5×6	2×14	2
NGC5005	13:10:56.2	+37:03:33	Sy2	non-Sy	0.003156	1.67	2.31	2007/06/09	5×6	2×14	2
MCG-03-34-064	13:22:24.4	-16:43:43	Sy2	HBLR	0.016541	0.88	2.86	2007/03/08	3×30	2×60	2
MCG-06-30-015	13:35:53.8	-34:17:44	Sy1		0.007749	0.33	0.97	2007/07/29	5×6	2×14	2
NGC5135	13:25:44.0	-29:50:01	Sy2	non-HBLR	0.013693	0.58	2.39	2007/07/29	5×6	2×14	2
NGC5256	13:38:17.5	+48:16:37	Sy2	non-HBLR	0.027863	0.30	1.13	2004/01/08	4×30	2×60	1,2
IC4329A	13:49:19.2	-30:18:34	Sy1		0.016054	1.11	2.26	2004/07/13	6×5	4×14	2
NGC5347	13:53:17.8	+33:29:27	Sy2	HBLR	0.007789	0.30	1.22	2007/06/15	7×6	4×14	2
NGC5506	14:13:14.9s	-03:12:27	Sy1	non-HBLR	0.006181	1.25	4.24	2007/07/31	5×6	2×14	2,4
NCG5548	14:17:59.5	+25:08:12	Sy1		0.017175	0.43	0.81	2007/07/31	5×6	2×14	2
NGC5929	15:26:06.1	+41:40:14	Sy2	HBLR	0.008312	0.43	1.67	2006/02/03	2×30	2×60	1,2
MCG-02-40-004	15:48:24.9	-13:45:28	Sy2	HBLR	0.025194	0.39	0.86	2007/03/18	2×30	4×14	
FSC15480-0344	15:50:41.5	-03:53:18	Sy2	HBLR	0.030300	0.19	0.73	2007/03/17	4×30	2×60	
NGC6810	19:43:34.4	-58:39:21	Sy2	non-Sy	0.006775	1.27	1.10	2007/04/30	2×30	4×14	
NGC6860	20:08:46.9	-61:06:01	Sy1		0.014884	0.24	0.33	2007/06/13	4×30	2×60	
MRK509	20:44:09.7	-10:43:25	Sy1		0.034397	0.30	0.73	2006/11/20	5×6	2×14	2
IC5063	20:52:02.3	-57:04:08	Sy2	HBLR	0.011348	1.15	3.95	2006/10/18	5×6	2×14	2
NGC7130	21:48:19.5	-34:57:05	Sy2	non-Sy	0.016151	0.64	2.15	2006/11/18	5×6	2×14	2

TABLE 1
Journal of Spitzer IRS observations

NGC7172	22:02:01.9	-31:52:11	Sy2	non-HBLR	0.008683	0.43	0.95	2007/06/12	5×6	2×14	2
NCG7213	22:09:16.2	-47:10:00	Sy1		0.005839	0.65	0.81	2007/06/13	7×6	4×14	2
3C445	22:23:49.6	-02:06:12	Sy1		0.056200	0.46	0.44	2004/06/07	4×30	2×60	1,2
NGC7314	22:35:46.2	-26:03:01	Sy1	HBLR	0.004763	0.55	0.96	2006/11/17	5×6	2×14	2,4
MCG-03-58-007	22:49:37.1	-19:16:26	Sy2	HBLR	0.031462	2.77	0.80	2006/12/20	4×30	2×60	
NGC7582	23:18:23.5	-42:22:14	Sy2	non-HBLR	0.005254	2.31	7.48	2007/06/17	2×6	2×6	2
NGC7674	23:27:56.7	+08:46:45	Sy2	HBLR	0.028924	0.64	1.79	2004/12/10	6×7	4×14	1,2
CGCG381-051	23:48:41.7	+02:14:23	Sy2	non-Sy	0.030668	0.16	0.51	2006/12/20	2×30	4×14	

[*] NOTES ON PROGRAMS: 1: Data without off-source measurements; 2: Data from Spitzer Archive; 3: Data from P50253 to be released; 4: see Appendix A for the source classification.

TABLE 2
Fine Structure Lines in our Sample

NAME	Line fluxes (10^{-14} $erg\ s^{-1}cm^{-2}$) in SH					Line fluxes (10^{-14} $erg\ s^{-1}cm^{-2}$) in LH				
	[SIV] ($10.51\mu m$)	[NeII] ($12.81\mu m$)	[NeV] ($14.32\mu m$)	[NeIII] ($15.56\mu m$)	[SIII] ($18.71\mu m$)	[SIII] ($18.71\mu m$)	[NeV] ($24.32\mu m$)	[OIV] ($25.89\mu m$)	[SIII] ($33.48\mu m$)	[SiII] ($34.82\mu m$)
MRK335	0.43±0.03	0.25±0.05	0.38±0.04	0.61±0.04	···	<0.62	1.97±0.18	7.24±0.19	<1.21	<1.45
MRK938	<1.46	52.1±1.45	<2.19	6.37±0.55	7.56±0.64	···	<0.37	<0.66	<10.7	40.5±4.21
MRK348	7.16±0.43	16.4±0.35	5.82±0.35	20.4±0.38	7.00±0.55	···	4.95±0.36	17.6±0.42	12.2±1.12	9.81±1.21
NGC526A	5.32±0.58	5.77±0.52	6.35±0.45	10.4±0.71	<2.50	···	5.92±0.29	19.3±0.44	5.91±1.05	8.58±1.19
IRAS01475-0740	2.14±0.32	13.7±0.30	6.38±0.32	9.95±0.34	<4.55	···	1.87±0.29	6.49±0.31	3.12±0.83	<6.13
NGC1056	<1.31	33.6±1.04	<1.80	10.4±0.34	18.3±0.35	···	<1.23	1.40±0.30	36.6±0.69	49.1±0.97
NGC1097	<0.85	59.1±0.22	<0.92	7.08±0.19	22.5±0.39	···	<2.31	6.20±0.75	131±2.47	254±1.25
NGC1142	1.43±0.11	17.2±0.11	0.92±0.09	5.40±0.10	8.32±0.12	24.7±0.25	1.82±0.13	5.31±0.18	32.2±0.67	67.0±0.96
MCG-02-8-039	4.83±0.30	3.86±0.30	6.59±0.31	9.79±0.30	2.00±0.36	···	5.24±0.19	14.4±0.23	<4.31	···
NGC1194	5.05±0.29	3.81±0.30	4.28±0.28	7.37±0.23	<2.25	···	3.76±0.22	15.1±0.31	3.98±0.63	3.60±0.87
NGC1241	1.06±0-33	13.4±0.26	1.61±0.30	8.08±0.37	5.53±0.39	···	1.23±0.16	5.46±0.17	13.8±0.55	19.1±0.86
NGC1320	9.01±0.41	9.58±0.36	10.7±0.35	13.6±0.33	4.15±0.44	···	7.46±0.31	27.4±0.37	12.0±0.81	10.4±0.92
NGC1365	18.6±0.78	143±3.79	19.1±0.61	61.3±0.51	51.2±0.57	···	97.5±13.2	365±26.9	720±102	1303±81
NGC1386	23.3±1.09	17.8±1.02	34.5±1.01	36.6±0.72	18.7±0.77	···	35.0±0.73	106±0.96	31.0±1.90	32.8±2.06
IRAS03450+0055	1.96±0.25	1.09±0.25	<1.48	1.82±0.25	···	···	<1.88	2.52±0.30	1.54±0.47	<4.5
3C120	24.1±0.86	7.84 ±0.63	16.6±0.89	27.6±0.93	7.34±1.48	<4.85	29±0.62	123±0.76	17.3±1.93	36.3±3.02
MRK618	6.36±0.34	16.4±0.45	3.89±0.41	5.38±0.55	5.30±0.53	···	<1.29	10.2±0.57	6.35±1.46	78.0±2.26
F04385-0828	2.38±0.42	13.9±0.53	2.28±.47	7.06±0.41	3.58±0.21	···	<1.44	8.56±0.49	<5.23	<5.36
NGC1667	1.75±0.34	10.1±0.30	1.32±0.26	7.23±0.30	3.46±0.31	···	1.22±0.27	7.06±0.33	24.5±1.61	54.3±1.68
ESO362-G018	1.70±0.16	12.4±0.21	3.27±0.20	7.49±0.19	3.87±0.16	···	2.62±0.24	8.93±0.24	7.50±0.52	11.8±0.43
ESO253-G3	6.86±0.28	16.0±0.36	6.81±0.31	18.0±0.40	···	7.93±0.26	7.21±0.31	24.2±0.47	9.62±1.30	···
F05563-3820	2.96±0.32	3.89±0.25	2.54±0.34	4.82±0.26	<1.47	···	<0.79	5.31±0.40	<1.84	2.89±0.71
MRK79	10.2±0.44	10.2±0.47	6.55±0.27	19.6±0.34	8.98±0.34	···	12.7±0.33	42.0±0.93	14.0±0.76	30.5±0.49
NGC2639	<0.80	9.95±0.22	<0.64	4.29±0.26	2.75±0.35	···	<1.70	8.21±0.39	17.1±1.03	29.2±1.15
MRK704	5.09±0.45	<3.30	3.93±0.34	5.63±0.38	<4.80	···	<3.75	11.8±0.42	<4.30	···
MKN1239	6.08±0.60	9.4±0.46	3.40±0.25	9.38±0.33	1.77±0.50	···	3.22±0.33	15.6±0.34	9.09±0.91	10.5±1.07
3C234	2.86±0.25	<1.29	2.35±0.25	3.40±0.34	···	<1.65	2.91±0.22	8.97±0.30	···	···
NGC3511	<0.72	8.75±0.25	<0.49	1.00±0.18	2.44±0.22	···	<1.66	<1.78	62.7±1.34	83.4±1.03
MCG+00-29-023	<0.72	47.1±0.40	<1.01	4.43±0.20	7.89±0.49	<6.52	<5.42	<6.01	49.3±3.42	136±3.43
NGC3982	1.48±0.33	11.4±0.34	2.89±0.31	6.79±0.30	3.16±0.39	···	1.62±0.30	5.11±0.40	15.4±0.61	32.8±1.07
NGC4051	4.75±0.38	21.2±0.31	10.7±0.35	17.1±0.36	7.45±0.49	···	32.2±0.21	94.6±3.59	38.8±3.93	39.6±1.01
MRK766	12.2±0.23	23.3±0.48	21.0±2.15	24.1±0.38	12.8±0.44	25.6±0.73	18.5±0.34	46.1±0.39	21.4±1.11	15.5±1.39
NGC4388	45.3±0.76	76.6±0.97	46.1±0.86	106±1.11	39.1±1.19	···	73.0±1.05	340±2.15	85.1±2.78	135±2.76
NGC4593	5.50±0.40	7.34±0.45	3.09±0.33	8.13±0.38	3.94±0.44	···	<4.32	33.3±0.77	19.1±0.36	32.2±1.37
NGC4922	1.94±0.27	35.1±0.51	2.77±0.31	8.86±0.32	12.4±0.34	18.2±1.36	<2.61	5.92±0.68	20.3±2.23	32.8±2.31
NGC4941	9.06±0.57	13.50±0.63	8.21±0.49	24.8±0.49	6.27±0.85	···	7.27±0.31	32.8±0.39	5.79±0.85	13.4±1.46
NCG5005	···	27.9±0.69	<0.92	11.7±0.67	3.61±0.72	···	<1.64	7.06±0.56	21.4±2.43	69.1±3.30
MCG-03-39-064	52.8±0.60	56.2±0.57	62.9±0.50	119±0.89	27.0±0.92	···	38.1±0.80	115±0.88	17.2±2.04	24.8±2.76
MCG-06-30-015	8.42 ±0.51	4.98 ±0.52	5.01 ±0.55	5.88±0.51	6.48±0.79	···	7.37±0.73	26.0±0.77	6.51±1.08	9.26±1.08
NGC5135	6.07±0.18	36.7±5.10	4.88±0.19	16.7±0.12	11.4±2.85	···	15.2±0.55	71.3±0.61	38.3±3.38	140±1.83
NGC5256	2.57±0.25	19.8±0.20	2.31±0.15	10.6±0.23	8.38±0.39	28.5±0.90	11.9±0.31	56.8±0.76	48.2±1.09	92.3±1.46
IC4329A	29.1±1.32	27.6±0.73	29.3±0.88	57.0±0.97	15.0±1.44	···	34.6±0.85	117±1.42	16.0±2.19	32.5±3.06
NCG5347	<2.41	4.17±0.82	2.08±0.69	4.09±0.74	<2.86	···	<1.74	7.64±0.62	<3.38	<4.62
NGC5506	25.4±0.32	26.4±0.40	18.5±0.28	45.6±0.24	19.1±0.50	···	56.5±0.50	239±0.87	90.1±1.71	137±2.40
NCG5548	6.37±0.71	8.47±0.62	5.4±0.39	7.27±0.78	5.93±0.95	···	3.89±0.5	17.5±0.63	<4.14	12.46±1.38
NGC5929	1.67±0.29	13.2±0.34	1.14±0.23	9.83±0.31	5.75±0.33	···	2.17±0.26	5.32±0.27	6.45±0.48	21.5±0.75
MCG-02-40-004	5.71±0.44	16.5±0.57	6.13±0.36	8.47±0.38	4.22±0.53	···	3.11±0.41	12.9±0.44	5.32±1.37	25.4±1.58
FSC15480-0344	5.19±0.34	5.57±0.28	6.08±0.26	9.35±0.32	2.72±0.48	<1.63	8.90±0.22	35.0±0.29	5.20±0.82	5.13±0.82
NGC6810	<1.09	103±1.88	<1.09	13.4±0.47	41.0±0.59	···	<2.35	2.55±0.90	78.2±2.89	118±2.83
NGC6860	3.36±0.28	5.60±0.30	2.85±0.21	6.65±0.19	2.80±0.25	···	2.41±0.14	12.1±0.17	7.93±0.64	10.4±0.64
MRK509	4.13±0.76	14.0±0.79	4.74±0.59	14.5±0.60	7.19±1.20	9.62±0.53	6.82±0.46	27.5±0.57	7.41±1.91	14.5±3.41
IC5063	47.4±0.86	26.7±1.17	30.3±0.86	66.3±0.99	21.8±1.19	···	23.6±1.37	114±1.34	31.0±3.00	52.7±3.26

TABLE 2
Fine Structure Lines in our Sample

NGC7130	5.27±0.84	79.3±0.93	9.09±0.64	29.4±0.77	19.6±0.33	54.2±0.88	5.22±0.86	19.7±0.84	48.2±2.59	93.9±4.90
NGC7172	5.87±0.61	33.0±1.01	10.2±0.67	17.1±0.68	11.9±1.00	···	13.8±0.49	45.4±0.48	26.9±1.51	59.3±2.42
NCG7213	2.32±0.61	25.7±0.74	<1.85	12.0±0.80	5.00±0.85	···	<7.89	<13.5	6.97±0.88	15.7±1.61
3C445	2.75±0.32	2.31±0.24	1.95±0.21	6.23±0.01	···	<3.54	5.84±0.11	22.6±0.92	<3.16	<3.69
NGC7314	15.9±0.53	8.08±0.39	16.9±0.52	23.2±0.53	9.97±0.71	···	21.5±0.32	67.0±0.41	15.0±1.71	14.2±1.76
MCG-03-58-007	2.75±0.21	8.52±0.34	6.63±0.33	9.29±0.37	5.20±0.60	1.92±0.36	3.91±0.30	8.80±0.34	<2.84	11.7±0.95
NGC7582	21.3±1.43	322±6.41	38.8±1.54	105±2.05	87.3±1.99	···	63.6±4.29	262±5.54	244±7.85	···
NGC7674	16.1±0.27	20.1±0.3	21.2±0.3	35.3±0.32	···	21.6±0.74	16.5±0.46	49.3±1.33	14.4±1.22	29.7±1.08
CGCG381-051	<0.61	19.1±0.44	<0.70	1.35±0.32	<0.65	···	<1.18	<1.26	9.36±1.13	12.5±1.72

TABLE 3
Molecular Hydrogen lines and PAH emission feature at 11.25μm

	Line fluxes (10^{-14} erg $s^{-1}cm^{-2}$)					
NAME	H_2 S(3) ($9.67\mu m$) (1)	H_2 S(2) ($12.28\mu m$) (2)	H_2 S(1) ($17.04\mu m$) (3)	H_2 S(0) ($28.22\mu m$) (4)	PAH ($11.25\mu m$) (5)	EQ.W. (μm) (6)
MRK335	···	<0.16	0.39±0.05	<0.72	···	···
MRK938	···	2.72±0.38	7.06±0.65	<1.02	292	-0.687
MRK348	···	<1.05	1.77±0.48	<1.14	···	···
NGC526A	···	<1.65	2.40±0.77	<1.41	···	···
IRAS01475-0740	···	<1.20	2.75±0.30	<2.18	30.3	-0.071
NGC1056	···	<2.46	3.58±0.48	2.25±0.27	214	-1.196
NGC1097	<1.69	6.95±0.55	14.4±0.24	4.95±0.94	285	-0.911
NGC1142	1.88±0.10	1.09±0.10	4.60±0.08	2.76±0.21	73.5	-0.707
MCG-02-08-039	···	0.89±0.29	1.21±0.38	<0.64	5.86	-0.021
NGC1194	···	<0.83	1.65±0.25	<0.96	···	···
NGC1241	···	<0.83	4.62±0.45	<0.57	44.7	-0.453
NGC1320	···	<1.26	3.26±0.37	<1.14	51.5	-0.072
NGC1365	···	5.38±1.65	21.0±1.17	37.59±14.87	657	-0.4
NGC1386	···	<2.75	5.65±0.86	<2.91	84.1	-0.106
IRAS03450+0055	<2.11	1.20±0.29	<2.12	<2.18	···	···
3C120	<1.68	<1.94	<2.52	<1.72	···	···
MRK618	<3.50	<2.54	2.41±0.48	<4.38	29.7	-0.047
F04385-0828	···	1.90±0.42	3.06±0.46	<2.17	50.5	-0.060
NGC1667	···	1.49±0.31	3.43±0.36	3.66±0.48	49.3	-0.807
ESO362-G018	···	<0.94	2.21±0.22	1.59±0.20	71.7	-0.232
ESO253-G3	<1.08	<1.02	1.93±0.39	<1.36	46.7	-0.092
F05563-3820	···	<1.22	<0.92	<2.88	···	···
MRK79	<0.99	<2.19	4.54±0.39	<2.18	13.4	-0.020
NGC2639	···	<0.6	0.96±0.34	<3.33	13.6	-0.199
MRK704	<2.00	<1.69	<3.06	<7.25	···	···
MRK1239	···	<1.13	<1.29	<0.85	34.2	-0.023
3C234	<1.48	<1.75	<0.57	<1.51	···	···
NGC3511	···	2.11±0.17	2.13±0.19	6.53±0.46	63.4	-1.086
MCG+00-29-023	<2.26	<1.55	8.00±0.51	<6.54	259	-0.702
NGC3982	···	<1.00	2.65±0.36	<1.16	52.6	-0.597
NGC4051	···	2.52±0.77	8.79±0.54	<7.37	133	-0.122
MRK766	···	<1.30	1.78±0.35	<1.45	58.5	-0.074
NGC4388	···	5.60±0.62	14.5±1.27	12.3±1.55	103	-0.141
NGC4593	···	<0.98	1.71±0.40	<4.51	44.5	-0.051
NGC4922	<1.69	1.98±0.35	7.81±0.47	<2.70	68.2	-0.145
NGC4941	···	<1.73	4.61±0.47	<1.35	···	···
NCG5005	···	11.96±0.84	26.0±0.62	8.35±0.85	243	-1.240
MCG-03-34-064	···	6.96±0.54	6.98±0.80	<2.75	71.2	-0.044
MCG-06-30-015	···	<1.69	2.91 ±0.52	<5.94	25.5	-0.035
NGC5135	···	<1.14	4.97±0.25	8.94±0.81	124	-0.554
NGC5256	···	1.63±0.19	4.68±0.24	<3.33	41.0	-0.595
IC4329A	···	<2.06	<3.19	<6.83	···	···
NCG5347	···	<2.12	6.49±0.91	2.95±0.73	33.2	-0.060
NGC5506	···	1.74±0.33	3.75±0.24	<3.40	34.8	-0.053
NCG5548	···	<1.70	<2.45	<0.25	34.9	-0.085
NGC5929	···	<1.03	4.10±0.27	<1.37	22.6	-0.495
MCG-02-40-004	···	<1.37	6.80±0.38	1.79±0.48	91.2	-0.120
FSC15480-0344	<0.89	<0.80	0.99±0.32	<0.98	49.2	-0.142
NGC6810	···	3.81±0.59	14.2±1.06	<3.50	91.2	-0.486
NGC6860	···	<1.56	2.69±0.24	1.18±0.24	21.7	-0.056
MRK509	<2.25	<1.24	<2.62	<1.79	53.9	-0.093
IC5063	···	6.64±0.97	9.43±1.03	8.65±1.42	···	···
NGC7130	···	<2.64	8.01±0.72	<2.94	216	-0.455
NGC7172	···	<2.13	6.60±0.76	4.23±0.67	145	-0.410
NCG7213	···	<1.73	2.45 ±0.76	<4.31	62.2	-0.116
3C445	<0.91	<0.61	<0.72	<2.70	···	···
NGC7314	···	<1.01	1.99±0.46	<2.00	···	···
MCG-03-58-007	···	<0.77	3.07±0.44	<1.11	47.1	-0.081
NGC7582	···	9.06±2.02	25.6±2.70	<14	920	-0.490
NGC7674	···	1.64±0.25	7.18±0.22	<1.54	84.6	-0.091
CGCG381-051	<1.49	<1.89	3.80±0.43	1.93±0.41	43.8	-0.203

---

[*] Columns (1) to (4) give the line fluxes of the H_2 rotational lines in units of 10^{-14} erg $s^{-1}cm^{-2}$. Column (5) and (6) give the flux and the equivalent width of the PAH 11.25 μm emission feature, respectively.

TABLE 4
H_2 ESTIMATED TEMPERATURES AND MASSES

NAME	T(2-3) (K)	T(1-2) (K)	T(0-1) (K)	H_2 Mass (10^8 $M_\odot$)
MRK938	···	304	>404	<1.47
MKN348	···	<379	>184	<0.51
NGC526A	···	<414	190	1.05
IRAS01475-0740	···	<322	>171	<1.32
NGC1056	···	<413	186	0.12
NGC1097	<195	339	206	0.27
NGC1142	363	249	189	4.65
MCG-02-08-039	···	432	>198	<1.23
NGC1194	···	<346	>191	<0.37
NGC1241	···	<226	>462	<11.93
NGC1320	···	<304	>237	<0.21
NGC1365	···	257	134	1.93
NGC1386	···	<340	>265	<0.03
IRAS03450+0055	366	369	157	3.97
MKR618	···	<563	>134	<9.72
F04385-0828	···	389	>178	<0.98
NGC1667	···	322	155	1.57
ESO362-G018	···	<318	177	0.48
ESO253-G3	···	<355	>178	<5.02
MKR79	···	<339	206	2.35
NGC2639	···	<390	>114	<0.68
NGC3511	···	535	117	0.15
MCG+00-29-023	···	<232	>169	<0.22
NGC3982	···	<301	>214	<0.04
NGC4051	···	304	>168	<0.08
MKN766	···	<430	>170	<0.46
NGC4388	···	304	167	1.17
NGC4593	···	<372	>122	<0.60
NGC4922	<277	256	>138	<12.12
NGC4941	···	<301	>258	<1.02
NGC5005	···	331	>246	<0.20
MCG-03-34-064	···	<538	224	1.71
MCG-06-30-015	···	<374	>129	<0.63
NGC5256	···	291	>178	<5.02
IC4329A	···	408	128	2.93
NGC5347	···	<283	211	0.39
NGC5929	···	<255	>242	<0.23
MCG-02-40-004	···	235	>273	<3.08
FSC15480-0344	···	<459	>162	<1.63
NGC6810	···	261	>283	<1.63
NGC6860	···	<373	214	0.58
IC5063	···	420	>163	<2.08
NGC7130	···	<284	>231	<1.79
NGC7172	···	<281	184	0.37
NGC7213	···	<421	>135	<0.52
NGC7314	···	<348	>158	<0.08
MCG-03-58-007	···	<255	>233	<2.65
NGC7582	···	<293	>196	<0.80
NCG7674	···	245	>307	<3.09
CGCG381-051	···	<368	192	3.80

TABLE 5
Photometric fluxes and extendedness factors

NAME	$F_{19\mu m}$(SH) (Jy)	$F_{19.5\mu m}$(LH) (Jy)	R	Class
MRK938	0.742±0.006	0.885±0.009	1.19	II
MRK348	0.589±0.007	0.647±0.003	1.10	I
NGC526A	0.363±0.017	0.361±0.003	0.993	I
IRAS01475-0740	0.462±0.003	0.507±0.004	1.1	I
NGC1056	0.130±0.006	0.209±0.001	1.61	III
NGC1142	0.096±0.001	0.184±0.015	1.92	III
MCG-02-08-039	0.356±0.005	0.379±0.003	1.06	I
NGC1194	0.336±0.007	0.427±0.004	1.27	II
NGC1241	0.100±0.004	0.144±0.002	1.44	II
NGC1320	0.698±0.005	0.743±0.005	1.06	I
NGC1386	0.793±0.015	0.990±0.006	1.23	II
IRAS03450+0055	0.473±0.006	0.463±0.003	0.98	I
3C120	0.579±0.024	0.577±0.006	0.996	I
MRK618	0.568±0.012	0.577±0.026	1.02	I
F04385-0828	0.910±0.007	1.008±0.006	1.11	I
NGC1667	0.053±0.004	0.154±0.009	2.91	III
ESO362-G018	0.339±0.005	0.361±0.002	1.06	I
ESO253-G3	0.565±0.003	0.667±0.002	1.18	II
MRK1239	0.944±0.001	0.971±0.002	1.07	I
3C234	0.237±0.005	0.258±0.005	1.09	I
NGC3982	0.116±0.003	0.172±0.003	1.48	II
MRK766	0.873±0.002	0.999±0.003	1.18	II
NGC4388	1.225±0.011	1.445±0.008	1.18	II
NGC4941	0.209±0.020	0.247±0.006	1.18	II
NCG5005	0.139±0.015	0.240±0.005	1.72	III
MCG-03-039-064	1.990±0.011	1.992±0.005	1.00	I
MCG-06-30-015	0.681±0.019	0.679±0.010	0.996	I
NCG5548	0.425±0.006	0.502±0.005	1.17	II
MCG-02-40-004	0.576±0.006	0.690±0.005	1.2	II
FSC15480-0344	0.455±0.006	0.496±0.002	1.09	I
NGC6810	1.514±0.005	1.910±0.004	1.26	II
NGC6860	0.280±0.003	0.317±0.004	1.13	I
MRK509	0.557±0.007	0.631±0.004	1.13	I
IC5063	2.344±0.008	2.480±0.011	1.06	I
NGC7130	0.814±0.009	1.094±0.004	1.34	II
NGC7172	0.256±0.014	0.338±0.003	1.32	II
NCG7213	0.425±0.020	0.541±0.003	1.27	II
NGC7314	0.233±0.008	0.248±0.004	1.07	I
MCG-03-58-007	0.651±0.005	0.677±0.005	1.04	I
NGC7582	2.337±0.042	3.290±0.015	1.40	II
CGCG381-051	0.336±0.008	0.343±0.011	1.02	I

TABLE 6
CLASSIFICATION TABLE

	Sy1	HBLR	AGN1	AGN2	non-Sy	"20μm peakers"
Extendedness	1.17±0.29	1.17±0.22	1.17±0.26	1.39±0.45	1.54±0.58	1.08±0.08
EW PAH 11.25μm	-0.15±0.20	-0.16±0.19	-0.15±0.19	-0.35±0.27	-0.81±0.42	-0.04±0.04
$\frac{[NeV]}{[NeII]}$	0.60±0.51	0.73±0.53	0.65±0.52	0.66±0.84	0.10±0.03	1.03±0.87
EW[NeII]12.81μm	-0.028±0.027	-0.028±0.026	-0.028±0.026	-0.081±0.057	-0.116±0.029	-0.014±0.015
EW[OIV]25.89μm	-0.122±0.127	-0.082±0.069	-0.116±0.134	-0.093±0.054	-0.033±0.035	-0.075±0.047
EW[H_2]17.07μm	-0.009±0.008	-0.008±0.006	-0.009±0.008	-0.046±0.069	-0.058±0.062	-0.008±0.003
%AGN at 19μm	92% ± 6%	92% ± 8%	92% ± 7%	79% ± 16%	69% ± 16%	96.8% ± 1.5%
$\alpha_{(60-25)\mu m}$	-0.84±0.62	-0.86±0.81	-0.86±0.74	-1.65±0.93	-2.19±0.65	-0.44±0.65

---

[*] Note: the mean values have been computed without considering the upper limits for all quantities and the zero values for the PAH EW.

TABLE 7

Equivalent widths of key lines

NAME	[NeII]12.81μm (μm)	[NeV]14.32μm (μm)	[NeIII]15.56μm (μm)	H_2 17.02μm (μm)	[OIV]25.89μm (μm)
MRK335	-0.002	-0.005	-0.010	-0.005	...
MRK938	-0.106	· · ·	-0.025	-0.025	...
MRK348	-0.030	-0.008	-0.037	-0.004	-0.063
NGC526A	-0.017	-0.022	-0.040	-0.013	-0.165
IRAS01475-0740	-0.028	-0.006	-0.023	-0.008	-0.023
NGC1056	-0.103	· · ·	-0.093	-0.025	-0.007
NGC1142	-0.141	-0.016	-0.063	-0.056	-0.032
MCG-02-08-039	-0.011	-0.022	-0.030	-0.006	-0.103
NGC1194	-0.007	-0.009	-0.018	-0.005	-0.060
NGC1241	-0.113	-0.015	-0.076	-0.045	-0.066
NGC1320	-0.013	-0.019	-0.022	-0.006	-0.066
NGC1386	-0.019	-0.040	-0.045	-0.007	-0.154
IRAS03450+0055	-0.001	· · ·	-0.008	· · ·	-0.010
3C120	-0.017	-0.038	-0.065	· · ·	-0.461
MRK618	-0.028	-0.007	-0.009	-0.004	-0.031
F04385-0828	-0.015	-0.001	-0.009	-0.004	-0.013
NGC1667	-0.183	-0.023	-0.195	-0.078	-0.065
ESO362-G018	-0.043	-0.012	-0.026	-0.007	-0.044
ESO253-G3	-0.028	-0.014	-0.040	-0.004	-0.058
F05563-3820	-0.005	-0.004	-0.009	· · ·	...
MRK1239	-0.007	-0.002	-0.010	· · ·	-0.037
3C234	· · ·	-0.010	-0.017	· · ·	-0.099
NGC3982	-0.100	-0.039	-0.073	-0.028	-0.050
MRK766	-0.032	-0.028	-0.031	-0.002	-0.071
NGC4388	-0.088	-0.054	-0.116	-0.014	-0.296
NGC4941	-0.075	-0.050	-0.143	-0.028	-0.225
NCG5005	-0.136	· · ·	-0.091	0.178	-0.044
MCG-03-39-064	-0.034	-0.039	-0.070	-0.004	0.1088
MCG-06-30-015	-0.010	-0.007	-0.009	-0.007	-0.076
NCG5135	-0.176	-0.032	-0.087	-0.021	...
IC4329A	-0.014	-0.014	-0.031	· · ·	...
NGC5347	-0.006	-0.004	-0.008	· · ·	...
NGC5506	-0.034	-0.029	-0.072	-0.007	...
NCG5548	-0.020	-0.013	-0.017	· · ·	-0.076
MCG-02-40-004	-0.022	-0.010	-0.015	-0.013	-0.030
FSC15480-0344	-0.017	-0.018	-0.028	-0.002	-0.120
NGC6810	-0.086	· · ·	-0.014	-0.013	-0.005
NGC6860	-0.015	-0.010	-0.023	-0.010	-0.087
MRK509	-0.027	-0.006	-0.032	· · ·	-0.096
IC5063	-0.012	-0.015	-0.033	-0.005	-0.075
NGC7130	-0.146	-0.016	-0.052	-0.012	-0.020
NGC7172	-0.092	-0.026	-0.046	-0.019	-0.163
NCG7213	-0.053	· · ·	-0.031	-0.007	· · ·
NGC7314	-0.039	-0.082	-0.106	-0.007	-0.467
MCG-03-58-007	-0.013	-0.013	-0.017	-0.005	-0.024
NGC7582	-0.126	-0.022	-0.060	-0.016	-0.088
CGCG381-051	-0.087	· · ·	-0.006	· · ·	· · ·

---

[*] MRK335, F05563-3820, NGC5135, IC4329A, NGC5347 and NGC5506 do not have calculated [OIV] equivalent width, because even if they have background subtracted spectra, the continuum in the (19-35)μm range results not well calibrated.

TABLE 8
AGN and Starburst Contribution at 19μm

NAME	AGN %	Starburst %	error
Seyfert 1			
ESO012-G021	85.4	14.6	4.5
ESO545-G013	78.4	21.6	13.5
NGC0931	97.7	2.3	0.7
MKR618	95.6	4.4	3.4
ESO362-G018	85.9	14.1	4.3
MRK0006	98.2	1.8	0.9
MRK0009	97.6	2.4	0.7
MKR79	98	2	1.1
MKN1239	97.7	2.3	1.6
NGC3516	95.6	4.4	1.1
MKN766	92.8	7.2	3.9
NGC4748	81.4	18.6	15.2
MRK0817	92.1	7.9	5.0
IRASF15091-2107	92.5	7.5	3.4
ESO141-G055	97	3	1.7
NGC6860	93.9	6.1	3.4
MKN509	90.9	9.1	4.6
HBLR			
ESO541-IG012	95.9	4.1	1.9
NGC0424	96.9	3.1	2.2
NGC0513	72.5	27.5	3.2
IRAS01475-0740	93.8	6.2	2.9
NGC1125	79.1	20.9	5
MCG-02-08-039	97	3	0.5
F04385-0828	95.8	4.2	2.3
NCG4388	91	9	3.1
NCG5347	92.9	7.1	4.1
TOLOLO1238-364	84.4	15.6	3.7
MCG-03-39-064	96.9	3.1	2.0
MCG-02-40-004	94.6	5.4	0.8
FSC15480-0344	94.5	5.5	0.5
IRASF22017+0319	95.6	4.4	1.3
MCG-03-58-007	95.7	4.3	1.7
AGN 2			
MRK938	52.9	47.1	12.6
IRAS00198-7926	96.8	3.2	0.8
NGC1142	44.8	55.2	6.2
NGC1241	69	31	7.9
NGC1320	95.4	4.6	1.4
NGC1667	71.7	28.3	11.9
ESO033-G002	96.8	3.2	1.9
ESO253-G3	89.6	10.4	2
NGC3660	75.5	24.5	7.3
NGC3982	80.6	19.4	7.7
NGC4501	70.2	29.8	7.6
NGC4968	90.1	9.9	2
NGC6890	89.5	10.5	1.3
NGC7582	68.8	31.2	11.3
NCG7172	85.3	14.7	3.5
non-BLR			
MRK1034 NED02	63.8	36.2	17.5
NGC4602	68	32	11.9
non-Sy			
MRK1034 NED01	67.0	33.0	21.0
NGC1056	68	32	12.1
NGC5005	43.1	56.9	8.5
MCG-03-34-063	41.6	58.4	17.7
NGC6810	80.5	19.5	8.8
MRK0897	53.8	46.2	16.1
NGC7130	77.2	22.8	9.8
NGC7496	81.2	18.8	9.3
NGC7590	75.6	24.4	10.3
CGCG381-051	87.5	12.5	14

TABLE 9
S-K STATISTIC FOR AGN FAMILIES

Diagram	Sy1 + HBLR	Sy1 + non-HBLR	HBLR + non-HBLR
F(H_2) vs F(PAH)	75%	18%	77%
L(H_2) vs L(PAH)	79%	88%	20%
EW PAH vs $\frac{[NeIII]}{[NeII]}$	100%	15%	39%
EW PAH vs $\frac{[NeV]}{[NeII]}$	54%	23%	54%
EW PAH vs $\frac{[OIV]}{[NeII]}$	40%	8%	41%
EW PAH vs $\frac{[NeV]}{[SiII]}$	98%	9%	20%
EW PAH vs EW[NeII]	78%	0.1%	0.4%
ext vs EW[NeII]	60%	19%	10%
ext vs EW[NeIII]	69%	17%	19%
ext vs EW PAH	84%	14%	33%
$\frac{[NeIII]}{[NeII]}$ vs α	97%	12%	12%
$\frac{[NeV]}{[NeII]}$ vs α	100%	6%	5%

TABLE 10

LINE LUMINOSITY FUNCTIONS OF SEYFERT 1

Luminosity(erg s^{-1}) L	Luminosity Function(10^{-6} Mpc^{-3} mag^{-1}) [SIV] (10.51μm)	[NeII] (12.81μm)	[NeV] (14.32μm)	[NeIII] (15.56μm)	[SIII] (18.71μm)	[NeV] (24.32μm)	[OIV] (25.89μm)	[SIII] (33.48μm)	[SiII] (34.82μm)
38.5	···	···	···	···	···	···	···	···	···
38.9	13.43±11.05	···	16.28±11.41	···	···	···	···	···	···
39.3	44.29±30.75	38.14±30.44	41.44±30.62	38.14±30.44	38.14±30.44	54.43±32.50	···	···	···
39.7	44.50±25.28	40.23±24.95	46.74±25.35	34.97±20.21	71.09±28.68	28.14±17.51	43.43±30.62	168.69±95.09	143.33±93.51
40.1	10.17±6.91	27.81±13.77	10.17±6.91	25.20±18.86	2.83±2.26	31.81±19.85	16.72±11.53	9.86±7.11	25.31±17.26
40.5	4.07±2.05	7.11±4.06	1.61±0.75	11.05±6.94	6.05±2.70	1.22±0.67	44.82±25.28	21.30±12.02	30.26±13.94
40.9	2.15±1.11	17.61±2.62	4.68±2.20	3.45±1.95	2.03±1.11	4.94±2.26	10.58±6.93	6.95±2.82	3.70±2.01
41.3	0.36±0.22	1.95±1.11	0.27±0.22	1.02±0.46	0.83±0.39	0.75±0.38	3.42±1.95	1.10±0.48	4.17±2.07
41.7	···	0.16±0.09	···	1.62±1.06	···	0.03±0.01	1.76±1.09	0.26±0.01	1.05±0.47
42.1	···	···	···	···	···	···	0.12±0.07	···	0.16±0.11
Line Luminosity Functions of Seyfert 2									
38.5	114.28±81.44	···	32.52±29.47	···	···	81.76±75.92	81.76±75.92	···	···
38.9	86.32±64.58	···	166.88±99.73	2.76±2.00	···	81.13±64.54	···	···	32.52±29.47
39.3	64.12±48.31	100.48±88.84	72.75±49.44	128.04±82.38	42.74±31.89	109.23±57.71	120.74±71.16	1.70±1.70	1.66±1.34
39.7	99.55±88.65	71.17±49.72	108.10±89.08	182.06±109.84	342.08±142.49	115.61±89.25	20.78±12.50	244.56±120.38	112.97±89.73
40.1	28.34±9.46	219.44±104.26	19.11±7.77	23.77±13.23	18.98±7.03	21.65±8.42	75.87±49.19	137.51±82.39	171.40±99.82
40.5	4.60±2.16	10.16±6.42	19.07±7.95	17.41±7.76	20.93±7.91	8.89±4.65	3.96±1.84	29.19±10.96	39.86±14.89
40.9	2.40±0.88	15.14±6.29	2.18±0.88	8.91±3.41	3.12±1.12	2.00±0.82	26.22±9.35	11.37±4.96	10.80±5.97
41.3	0.90±0.74	2.48±1.02	1.11±0.77	2.36±0.86	0.89±0.42	1.53±0.88	1.01±0.44	1.35±0.59	3.07±1.53
41.7	···	1.68±0.64	0.14±0.08	···	0.12±0.08	···	0.52±0.44	1.02±0.51	1.28±0.59
42.1	···	···	···	···	···	···	0.29±0.17	0.07±0.03	0.81±0.48

Luminosity(erg s^{-1})	Seyfert 1		Seyfert 2	
L	H_2 S(1)	PAH	H_2 S(1)	PAH
38.5	···	20.87±11.50	···	137.56±76.19
38.9	56.82±35.52	3.04±2.84	197.81±111.08	20.16±12.41
39.3	42.54±20.89	0.38±0.20	66.75±58.40	3.66±1.80
39.7	12.41±7.36	···	55.29±19.55	2.56±1.41
40.1	5.90±2.93	0.31±0.25	15.10±5.01	1.30±0.54
40.5	2.34±1.12	0.09±0.08	1.44±0.70	···
40.9	0.72±0.32	···	2.55±0.80	···
41.3	···	···	···	···
41.7	···	···	···	···
42.1	···	···	···	···

TABLE 11
New Classification, PAH flux and EQ.W. and H_2 Masses for Sources in Paper I

NAME	Old class.	New class.	PAH at 11.25μm flux (10^{-14} $erg\ s^{-1} cm^{-2}$)	EQ.W. (μm)	H_2 Mass (10^8 $M_\odot$)
IRAS00198-7926	Sy2	non-HBLR	31.2	-0.066	<19.36
ESO012-G021	Sy1		88.9	-0.417	<1.91
IRAS00521-7054	Sy2	HBLR		···	<12.27
ESO541-IG012	Sy2	HBLR	12.5	-0.031	<27.80
NGC0424	Sy2	HBLR	19.2	-0.001	<0.42
NGC0513	Sy2	HBLR	74.7	-0.588	3.69
MRK1034 NED01 (1)	Sy1	non-Sy	87.1	-1.105	5.36
MRK1034 NED02 (1)	Sy1	non-BLR	187	-1.051	<11.86
ESO545-G013 (1)	Sy1		21.9	-0.262	2.37
NGC0931	Sy1		39.5	-0.043	···
NGC1125	Sy2	HBLR	64.2	-0.465	<0.33
ESO033-G002	Sy2	non-HBLR	10.8	-0.024	0.66
MRK0006	Sy1		20.0	-0.041	<30.29
MRK0009	Sy1		15.2	-0.039	<2.20
NGC3516	Sy1		25.8	-0.037	<0.22
NGC3660	Sy2	non-HBLR	32.4	-0.584	0.94
NGC4501	Sy2	non-HBLR	36.1	-0.652	0.41
NGC4602 (1)	Sy1	non-BLR	28.2	-0.689	0.38
TOLOLO1238-364	Sy2	HBLR	111	-0.131	<0.44
NGC4748	Sy1		20.7	-0.300	0.38
NGC4968	Sy2	non-HBLR	88.1	-0.133	<0.30
MCG-03-34-063	Sy1	non-Sy	16.7	-1.176	<1.24
MRK0817	Sy1		24.5	-0.043	<2.73
IRASF15091-2107	Sy1		25.7	-0.081	<9.36
ESO141-G055	Sy1		19.2	-0.056	···
NGC6890	Sy2	non-HBLR	48.8	-0.155	0.20
MRK0897	Sy2	non-Sy	117	-1.194	1.66
IRASF22017+0319	Sy2	HBLR	9.56	-0.021	<6.75
NGC7496	Sy1	non-Sy	153	-0.419	<0.12
NGC7590	Sy1	non-Sy	56.1	-1.166	0.12

---

(1) See Appendix A for the source classification.

TABLE 12
Rare ionic fine structure lines

NAME	Line fluxes (10^{-14} erg $s^{-1}cm^{-2}$) [ArV] ($13.10\mu m$)	[FeIII] ($22.93\mu m$)	[FeII] ($24.52\mu m$)	[FeII] ($25.99\mu m$)	[FeIII] ($33.04\mu m$)
NGC1056	···	···	···	2.83±0.04	···
NGC1142	···	···	···	2.51±0.03	···
NGC1194	···	···	0.85±0.01	···	···
NGC1241	···	···	···	2.41±0.01	···
ESO253-G3	0.02786	···	···	···	···
NGC5135	···	···	···	6.80±0.61	···
NGC6810	···	11.12±0.05	···	9.69±0.12	1.23±0.08
NGC7130	···	···	···	11.81±0.10	···

TABLE 13
Average Full Width Half Maximum of the Lines

	Dispersion Velocity (km s^{-1}) FWHM	St. Dev.
$[SIV]10.51\mu m$	685	122
$[NeII]12.81\mu m$	604	151
$[NeV]14.32\mu m$	625	123
$[NeIII]15.56\mu m$	638	119
$[SIII]18.71\mu m$	673	185
$[NeV]24.32\mu m$	601	163
$[OIV]25.89\mu m$	552	89
$[SIII]33.48\mu m$	580	119
$[SiII]34.82\mu m$	708	215
H_2 S(1) $17.04\mu m$	587	149

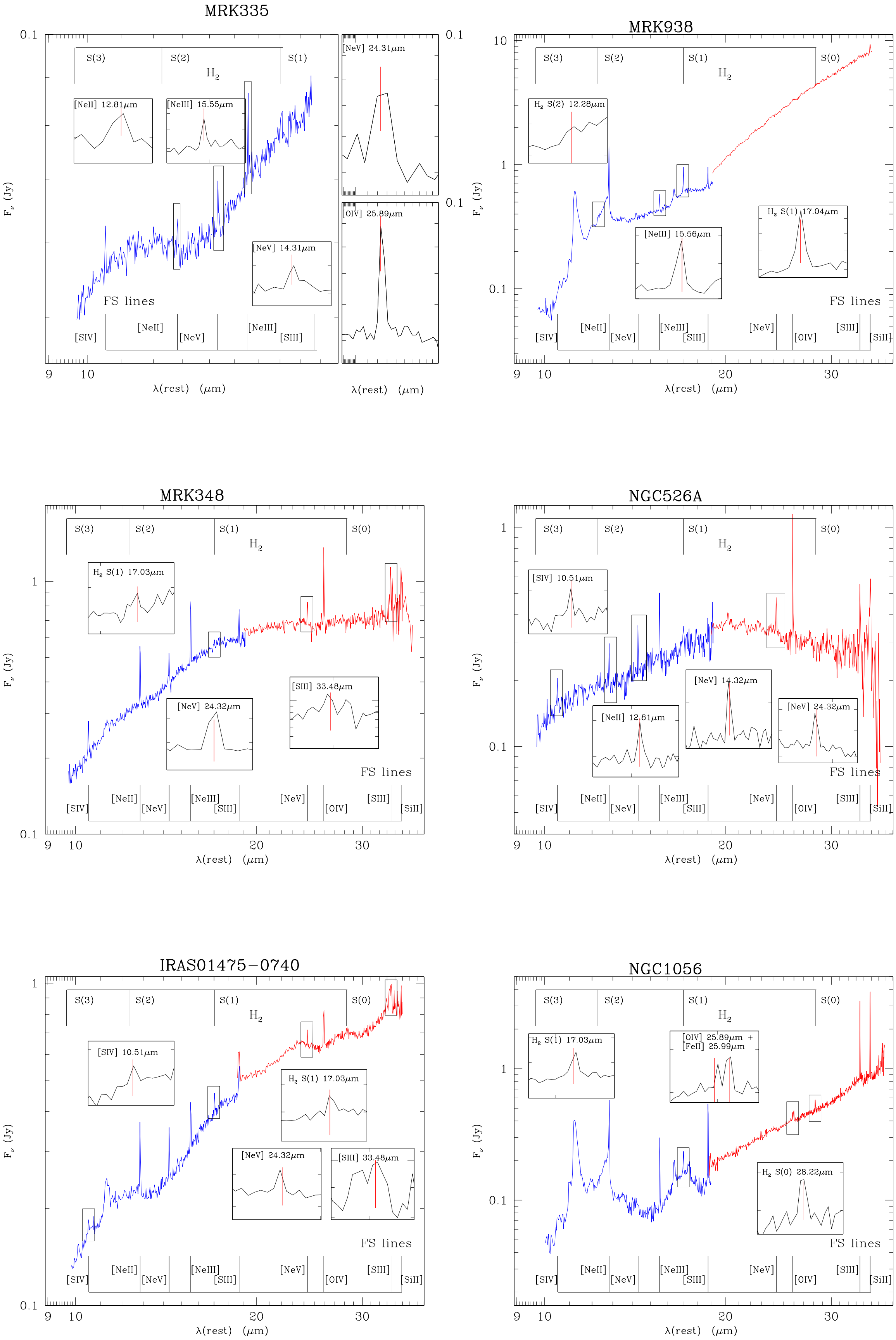

FIG. 1.— Spitzer IRS SH and LH specra of the observed Seyfert galaxies. Wavelengths have been shifted to the galaxies rest frames. For the objects with no off-source observation the SH spectrum is shown, because slightly affected from the background emission (1*simeq* 10 %), together with the $> 3\sigma$ detected lines in separated boxes. Figures 1.11.61 are available in the online version of the Journal.

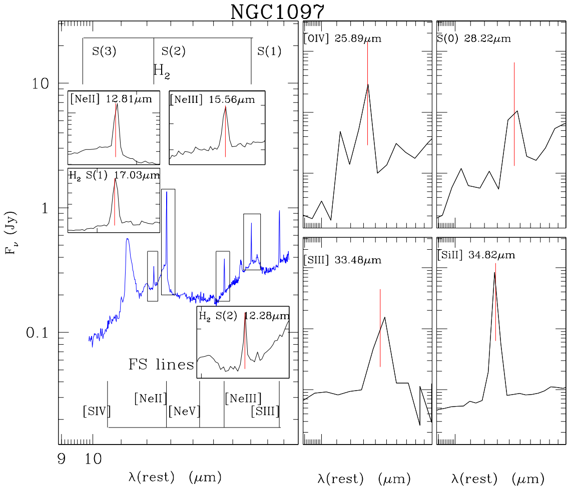
NGC1097
S(3)
S(2)
S(1)
H_2
[NeII] 12.81μm
[NeIII] 15.56μm
H_2 S(1) 17.03μm
H_2 S(2) 12.28μm
FS lines
[SIV]
[NeII]
[NeV]
[NeIII]
[SIII]
[OIV] 25.89μm
S(0) 28.22μm
[SIII] 33.48μm
[SiII] 34.82μm
10
1
0.1
F_ν (Jy)
9
10
λ(rest) (μm)
λ(rest) (μm)
λ(rest) (μm)

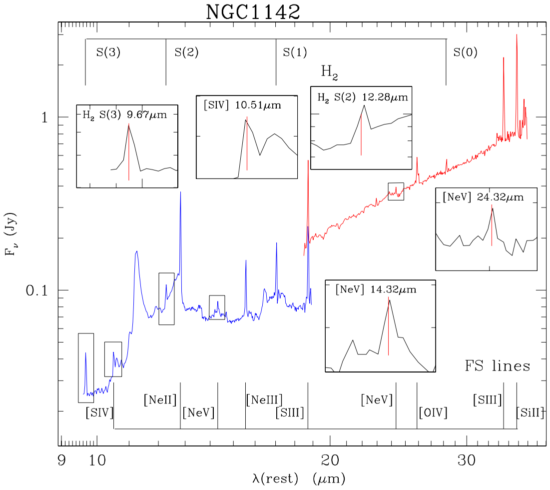
NGC1142
S(3)
S(2)
S(1)
S(0)
H_2
H_2 S(3) 9.67μm
[SIV] 10.51μm
H_2 S(2) 12.28μm
[NeV] 24.32μm
[NeV] 14.32μm
FS lines
[SIV]
[NeII]
[NeV]
[NeIII]
[SIII]
[NeV]
[OIV]
[SIII]
[SiII]
1
0.1
F_ν (Jy)
9
10
20
30
λ(rest) (μm)

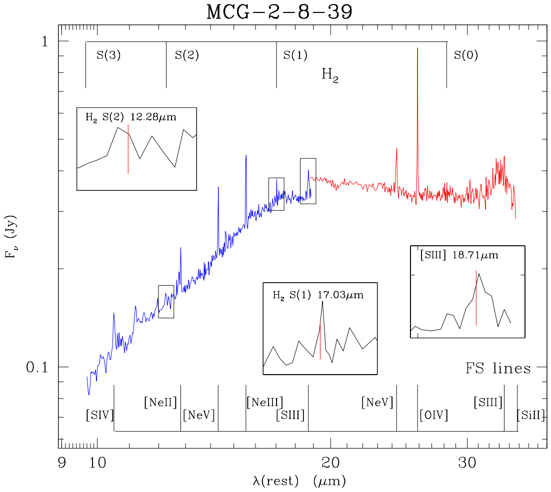
MCG−2−8−39
S(3)
S(2)
S(1)
S(0)
H_2
H_2 S(2) 12.28μm
H_2 S(1) 17.03μm
[SIII] 18.71μm
FS lines
[SIV]
[NeII]
[NeV]
[NeIII]
[SIII]
[NeV]
[OIV]
[SIII]
[SiII]
1
0.1
F_ν (Jy)
9
10
20
30
λ(rest) (μm)

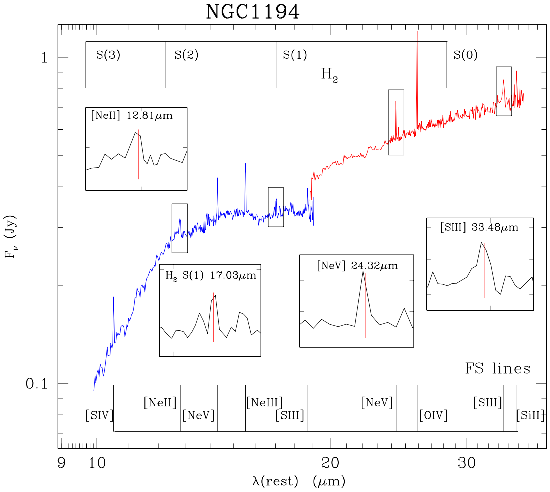
NGC1194
S(3)
S(2)
S(1)
S(0)
H_2
[NeII] 12.81μm
H_2 S(1) 17.03μm
[NeV] 24.32μm
[SIII] 33.48μm
FS lines
[SIV]
[NeII]
[NeV]
[NeIII]
[SIII]
[NeV]
[OIV]
[SIII]
[SiII]
1
0.1
F_ν (Jy)
9
10
20
30
λ(rest) (μm)

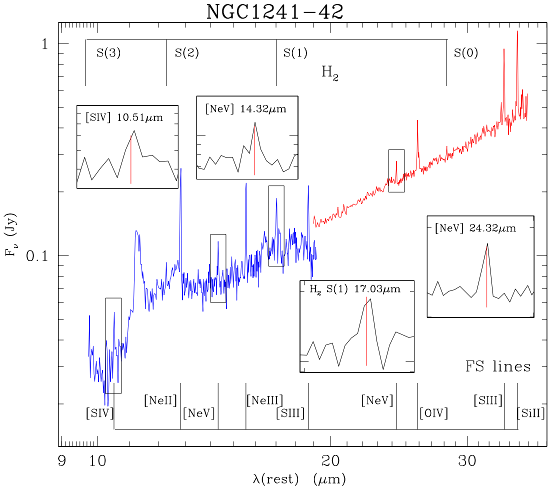
NGC1241−42
S(3)
S(2)
S(1)
S(0)
H_2
[SIV] 10.51μm
[NeV] 14.32μm
[NeV] 24.32μm
H_2 S(1) 17.03μm
FS lines
[SIV]
[NeII]
[NeV]
[NeIII]
[SIII]
[NeV]
[OIV]
[SIII]
[SiII]
1
0.1
F_ν (Jy)
9
10
20
30
λ(rest) (μm)

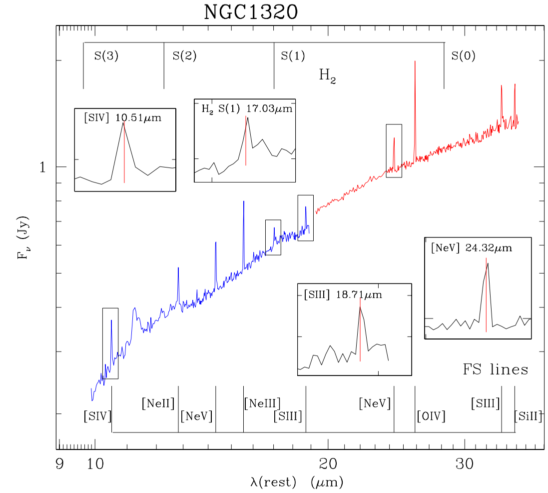
NGC1320
S(3)
S(2)
S(1)
S(0)
H_2
[SIV] 10.51μm
H_2 S(1) 17.03μm
[NeV] 24.32μm
[SIII] 18.71μm
FS lines
[SIV]
[NeII]
[NeV]
[NeIII]
[SIII]
[NeV]
[OIV]
[SIII]
[SiII]
1
F_ν (Jy)
9
10
20
30
λ(rest) (μm)

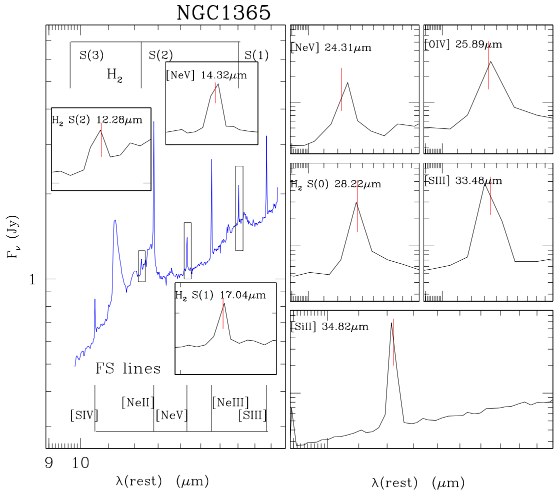
NGC1365
S(3)
S(2)
S(1)
H_2
[NeV] 14.32μm
H_2 S(2) 12.28μm
H_2 S(1) 17.04μm
FS lines
[SIV]
[NeII]
[NeV]
[NeIII]
[SIII]
[NeV] 24.31μm
[OIV] 25.89μm
H_2 S(0) 28.22μm
[SIII] 33.48μm
[SiII] 34.82μm
1
F_ν (Jy)
9
10
λ(rest) (μm)

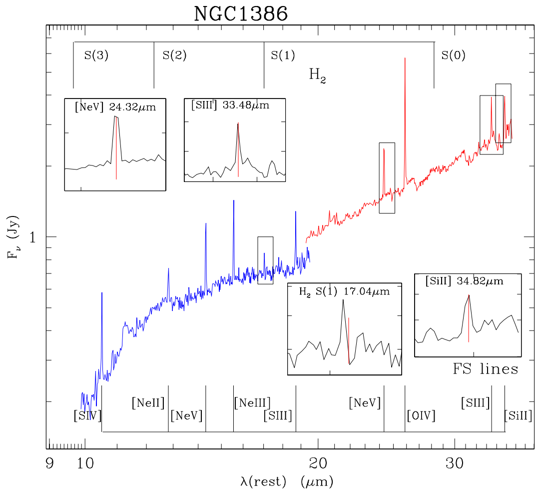
NGC1386
S(3)
S(2)
S(1)
S(0)
H_2
[NeV] 24.32μm
[SIII] 33.48μm
H_2 S(1) 17.04μm
[SiII] 34.82μm
FS lines
[SIV]
[NeII]
[NeV]
[NeIII]
[SIII]
[NeV]
[OIV]
[SIII]
[SiII]
1
F_ν (Jy)
9
10
20
30
λ(rest) (μm)

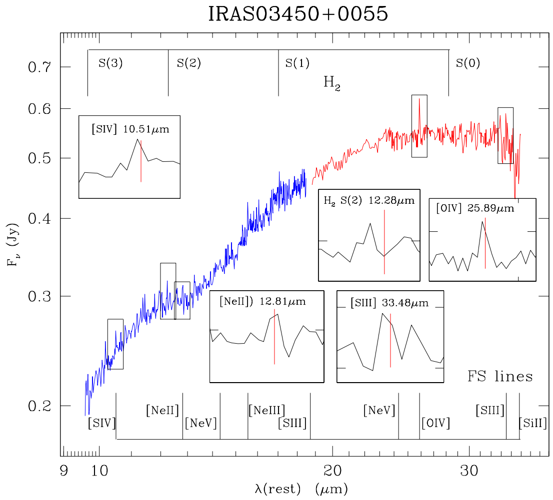
IRAS03450+0055
S(3)
S(2)
S(1)
S(0)
H_2
[SIV] 10.51μm
H_2 S(2) 12.28μm
[OIV] 25.89μm
[NeII]) 12.81μm
[SIII] 33.48μm
FS lines
[SIV]
[NeII]
[NeV]
[NeIII]
[SIII]
[NeV]
[OIV]
[SIII]
[SiII]
0.7
0.6
0.5
0.4
0.3
0.2
F_ν (Jy)
9
10
20
30
λ(rest) (μm)

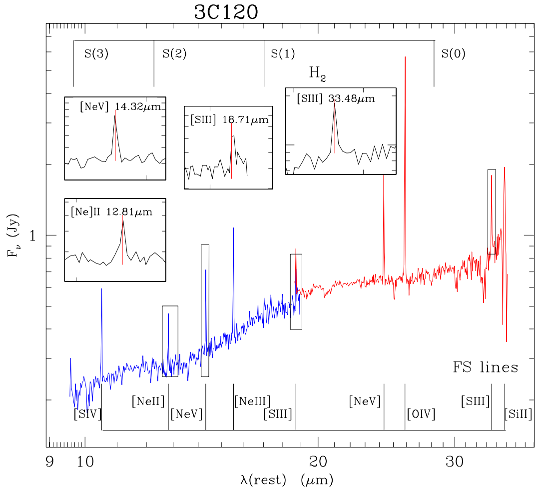
3C120
S(3)
S(2)
S(1)
S(0)
H_2
[NeV] 14.32μm
[SIII] 18.71μm
[SIII] 33.48μm
[Ne]II 12.81μm
FS lines
[SIV]
[NeII]
[NeV]
[NeIII]
[SIII]
[NeV]
[OIV]
[SIII]
[SiII]
1
F_ν (Jy)
9
10
20
30
λ(rest) (μm)

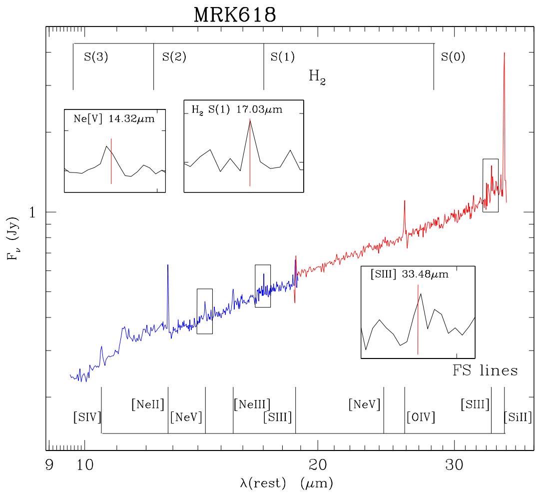
MRK618
S(3)
S(2)
S(1)
S(0)
H_2
Ne[V] 14.32μm
H_2 S(1) 17.03μm
[SIII] 33.48μm
FS lines
[SIV]
[NeII]
[NeV]
[NeIII]
[SIII]
[NeV]
[OIV]
[SIII]
[SiII]
1
F_ν (Jy)
9
10
20
30
λ(rest) (μm)

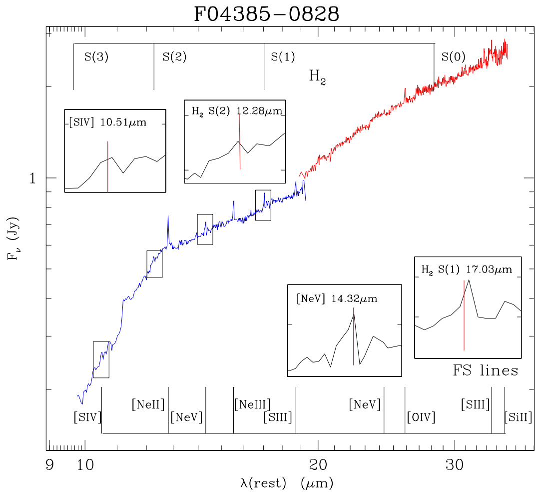
F04385−0828
S(3)
S(2)
S(1)
S(0)
H_2
[SIV] 10.51μm
H_2 S(2) 12.28μm
[NeV] 14.32μm
H_2 S(1) 17.03μm
FS lines
[SIV]
[NeII]
[NeV]
[NeIII]
[SIII]
[NeV]
[OIV]
[SIII]
[SiII]
1
F_ν (Jy)
9
10
20
30
λ(rest) (μm)

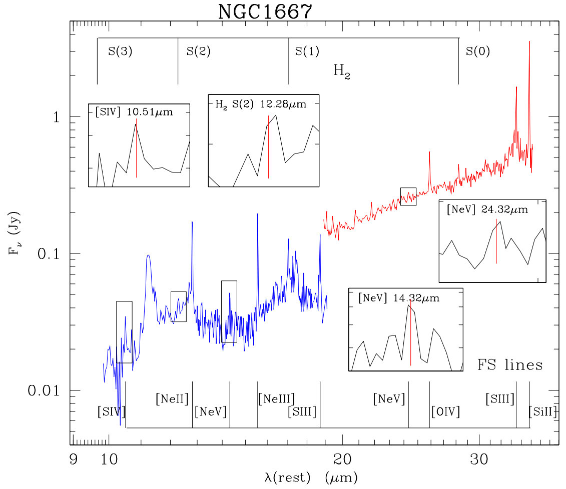
NGC1667
S(3)
S(2)
S(1)
S(0)
H$_2$
[SIV] 10.51μm
H$_2$ S(2) 12.28μm
[NeV] 24.32μm
[NeV] 14.32μm
FS lines
[SIV]
[NeII]
[NeV]
[NeIII]
[SIII]
[NeV]
[OIV]
[SIII]
[SiII]
F$_\nu$ (Jy)
1
0.1
0.01
9
10
20
30
λ(rest) (μm)

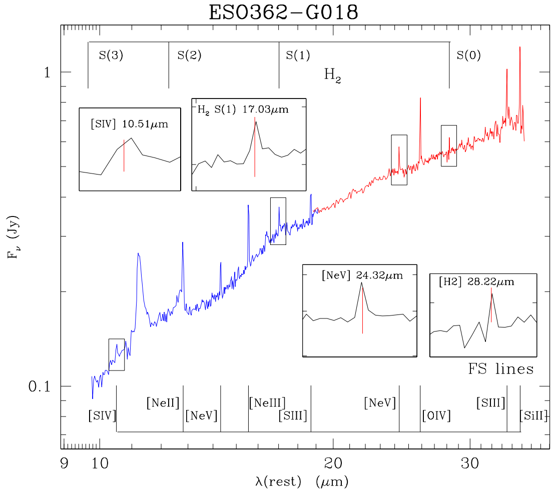
ESO362−G018
S(3)
S(2)
S(1)
S(0)
H$_2$
[SIV] 10.51μm
H$_2$ S(1) 17.03μm
[NeV] 24.32μm
[H2] 28.22μm
FS lines
[SIV]
[NeII]
[NeV]
[NeIII]
[SIII]
[NeV]
[OIV]
[SIII]
[SiII]
F$_\nu$ (Jy)
1
0.1
9
10
20
30
λ(rest) (μm)

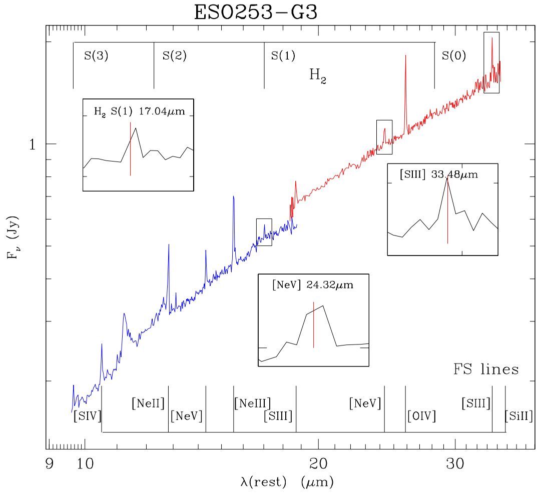
ESO253−G3
S(3)
S(2)
S(1)
S(0)
H$_2$
H$_2$ S(1) 17.04μm
[SIII] 33.48μm
[NeV] 24.32μm
FS lines
[SIV]
[NeII]
[NeV]
[NeIII]
[SIII]
[NeV]
[OIV]
[SIII]
[SiII]
F$_\nu$ (Jy)
1
9
10
20
30
λ(rest) (μm)

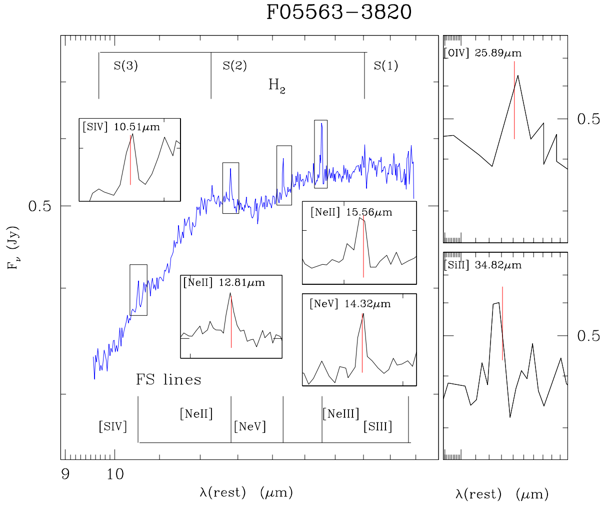
F05563−3820
S(3)
S(2)
S(1)
H$_2$
[SIV] 10.51μm
[NeII] 15.56μm
[NeII] 12.81μm
[NeV] 14.32μm
FS lines
[SIV]
[NeII]
[NeV]
[NeIII]
[SIII]
[OIV] 25.89μm
[SiII] 34.82μm
0.5
0.5
0.5
F$_\nu$ (Jy)
9
10
λ(rest) (μm)
λ(rest) (μm)

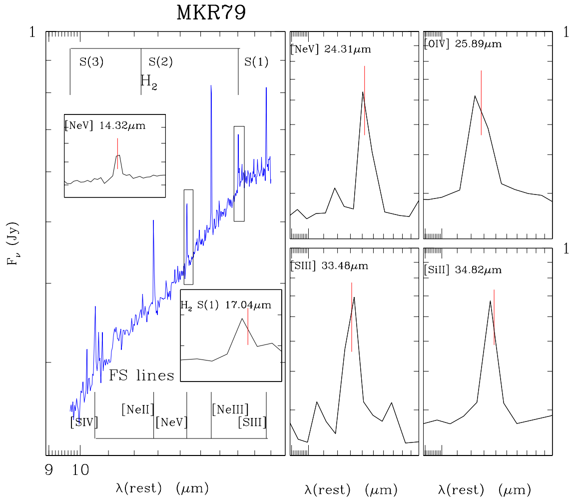
MKR79
S(3)
S(2)
S(1)
H$_2$
[NeV] 14.32μm
H$_2$ S(1) 17.04μm
FS lines
[SIV]
[NeII]
[NeV]
[NeIII]
[SIII]
[NeV] 24.31μm
[OIV] 25.89μm
[SIII] 33.48μm
[SiII] 34.82μm
1
1
1
F$_\nu$ (Jy)
9
10
λ(rest) (μm)
λ(rest) (μm)
λ(rest) (μm)

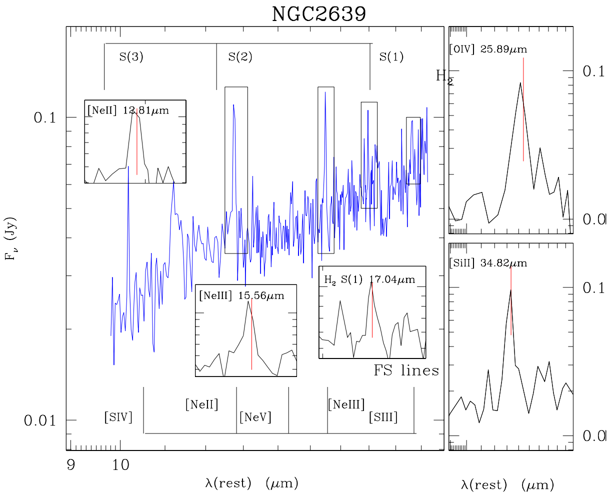
NGC2639
S(3)
S(2)
S(1)
H$_2$
[NeII] 12.81μm
[NeIII] 15.56μm
H$_2$ S(1) 17.04μm
FS lines
[SIV]
[NeII]
[NeV]
[NeIII]
[SIII]
[OIV] 25.89μm
[SiII] 34.82μm
0.1
0.01
0.1
0.0
0.1
0.0
F$_\nu$ (Jy)
9
10
λ(rest) (μm)
λ(rest) (μm)

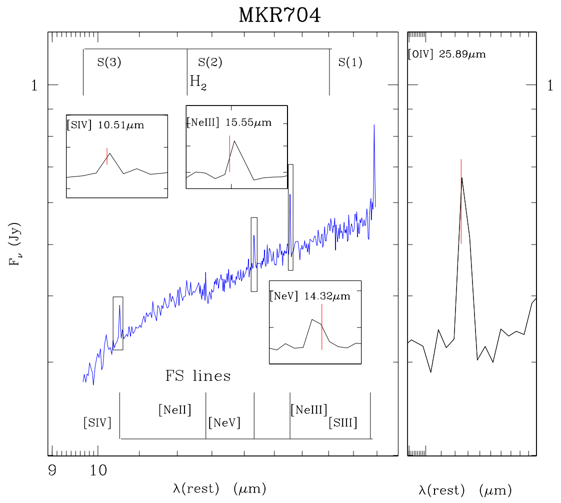
MKR704
S(3)
S(2)
S(1)
H$_2$
[SIV] 10.51μm
[NeIII] 15.55μm
[NeV] 14.32μm
[OIV] 25.89μm
FS lines
[SIV]
[NeII]
[NeV]
[NeIII]
[SIII]
1
F$_\nu$ (Jy)
9
10
λ(rest) (μm)
λ(rest) (μm)

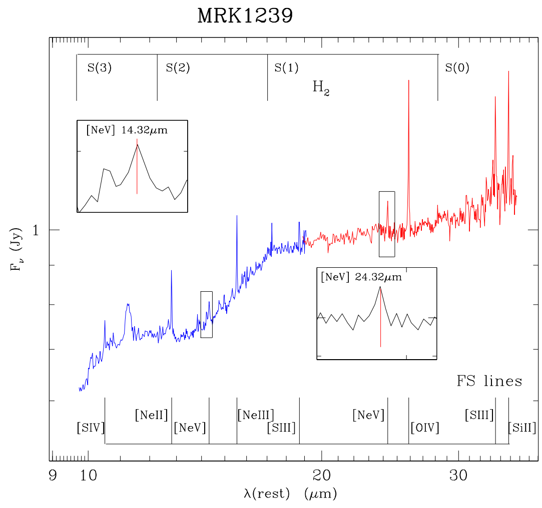
MRK1239
S(3)
S(2)
S(1)
S(0)
H$_2$
[NeV] 14.32μm
[NeV] 24.32μm
FS lines
[SIV]
[NeII]
[NeV]
[NeIII]
[SIII]
[NeV]
[OIV]
[SIII]
[SiII]
1
F$_\nu$ (Jy)
9
10
20
30
λ(rest) (μm)

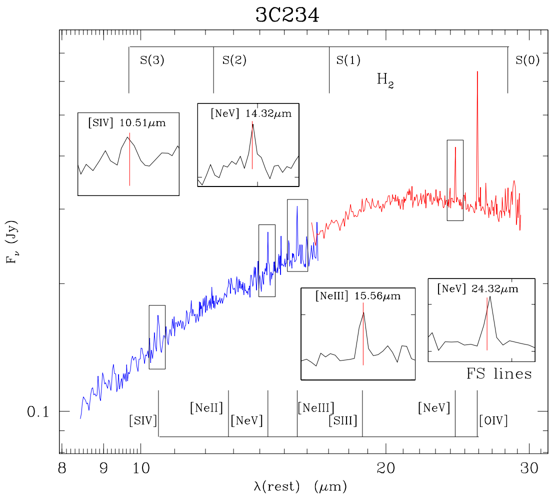
3C234
S(3)
S(2)
S(1)
S(0)
H$_2$
[SIV] 10.51μm
[NeV] 14.32μm
[NeIII] 15.56μm
[NeV] 24.32μm
FS lines
[SIV]
[NeII]
[NeV]
[NeIII]
[SIII]
[NeV]
[OIV]
0.1
F$_\nu$ (Jy)
8
9
10
20
30
λ(rest) (μm)

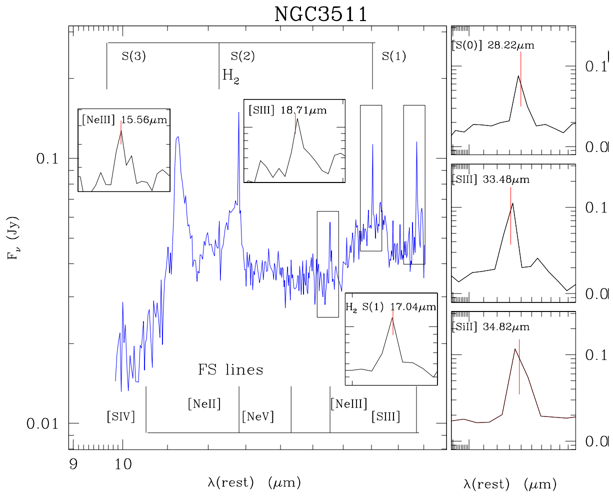
NGC3511
S(3)
S(2)
S(1)
H$_2$
[NeIII] 15.56μm
[SIII] 18.71μm
H$_2$ S(1) 17.04μm
[S(0)] 28.22μm
[SIII] 33.48μm
[SIII] 34.82μm
FS lines
[SIV]
[NeII]
[NeV]
[NeIII]
[SIII]
0.1
0.01
F$_\nu$ (Jy)
9
10
λ(rest) (μm)
λ(rest) (μm)

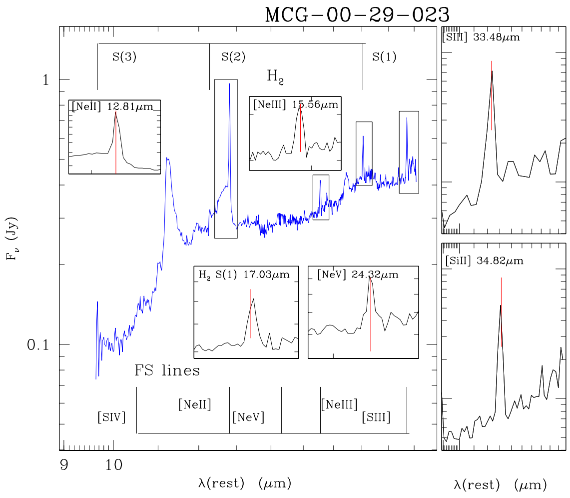
MCG−00−29−023
S(3)
S(2)
S(1)
H$_2$
[NeII] 12.81μm
[NeIII] 15.56μm
H$_2$ S(1) 17.03μm
[NeV] 24.32μm
[SIII] 33.48μm
[SIII] 34.82μm
FS lines
[SIV]
[NeII]
[NeV]
[NeIII]
[SIII]
1
0.1
F$_\nu$ (Jy)
9
10
λ(rest) (μm)
λ(rest) (μm)

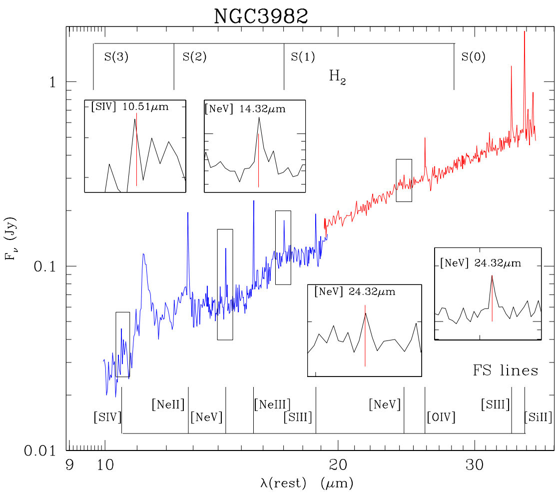
NGC3982
S(3)
S(2)
S(1)
S(0)
H$_2$
[SIV] 10.51μm
[NeV] 14.32μm
[NeV] 24.32μm
[NeV] 24.32μm
FS lines
[SIV]
[NeII]
[NeV]
[NeIII]
[SIII]
[NeV]
[OIV]
[SIII]
[SiII]
1
0.1
0.01
F$_\nu$ (Jy)
9
10
20
30
λ(rest) (μm)

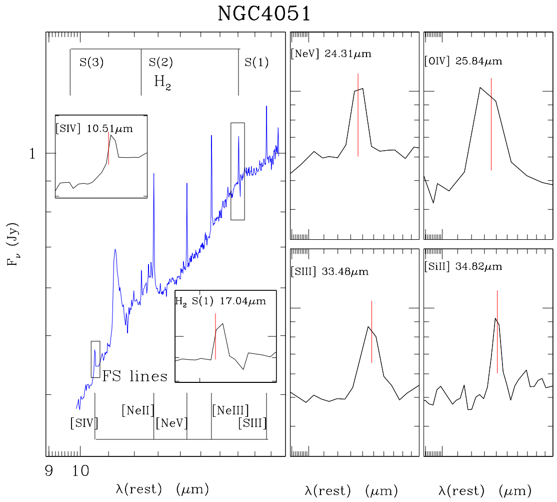
NGC4051
S(3)
S(2)
S(1)
H$_2$
[SIV] 10.51μm
H$_2$ S(1) 17.04μm
FS lines
[NeII]
[SIV]
[NeV]
[NeIII]
[SIII]
[NeV] 24.31μm
[OIV] 25.84μm
[SIII] 33.48μm
[SiII] 34.82μm
1
1
1
F$_\nu$ (Jy)
9
10
λ(rest) (μm)
λ(rest) (μm)
λ(rest) (μm)

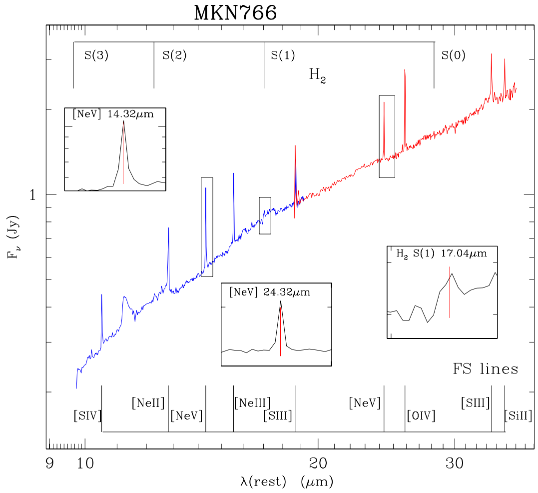
MKN766
S(3)
S(2)
S(1)
S(0)
H$_2$
[NeV] 14.32μm
[NeV] 24.32μm
H$_2$ S(1) 17.04μm
FS lines
[SIV]
[NeII]
[NeV]
[NeIII]
[SIII]
[NeV]
[OIV]
[SIII]
[SiII]
1
F$_\nu$ (Jy)
9
10
20
30
λ(rest) (μm)

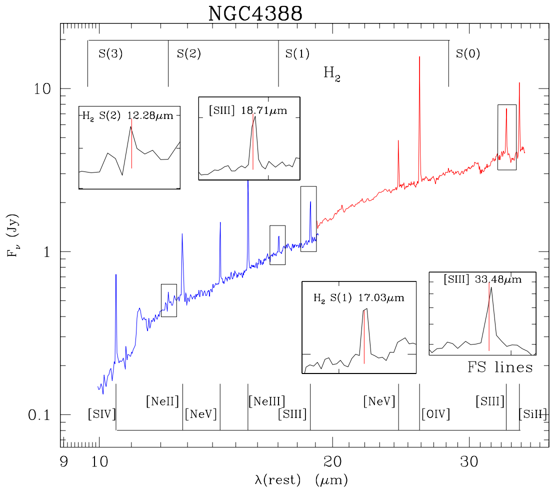
NGC4388
S(3)
S(2)
S(1)
S(0)
H$_2$
H$_2$ S(2) 12.28μm
[SIII] 18.71μm
H$_2$ S(1) 17.03μm
[SIII] 33.48μm
FS lines
[SIV]
[NeII]
[NeV]
[NeIII]
[SIII]
[NeV]
[OIV]
[SIII]
[SiII]
10
1
0.1
F$_\nu$ (Jy)
9
10
20
30
λ(rest) (μm)

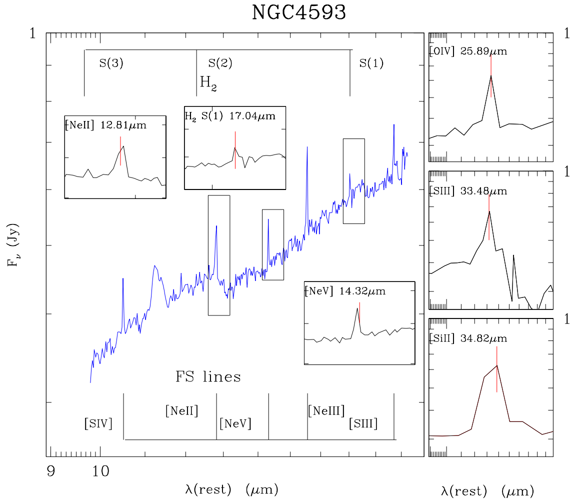
NGC4593
S(3)
S(2)
S(1)
H$_2$
[NeII] 12.81μm
H$_2$ S(1) 17.04μm
[NeV] 14.32μm
FS lines
[SIV]
[NeII]
[NeV]
[NeIII]
[SIII]
[OIV] 25.89μm
[SIII] 33.48μm
[SiII] 34.82μm
1
1
1
1
F$_\nu$ (Jy)
9
10
λ(rest) (μm)
λ(rest) (μm)

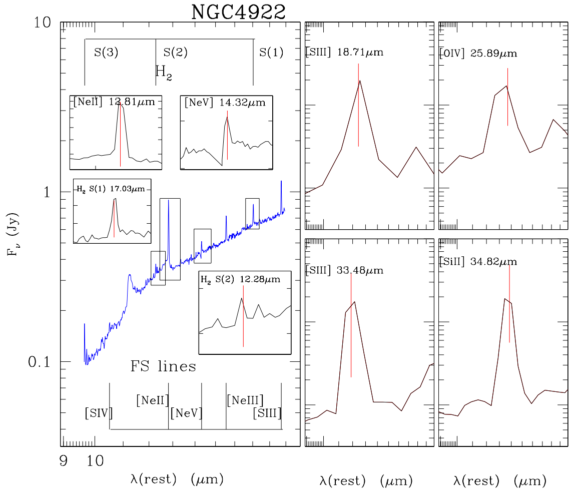
NGC4922
S(3)
S(2)
S(1)
H$_2$
[NeII] 12.81μm
[NeV] 14.32μm
H$_2$ S(1) 17.03μm
H$_2$ S(2) 12.28μm
FS lines
[SIV]
[NeII]
[NeV]
[NeIII]
[SIII]
[SIII] 18.71μm
[OIV] 25.89μm
[SIII] 33.48μm
[SiII] 34.82μm
10
1
0.1
10
1
0.1
10
1
0.1
F$_\nu$ (Jy)
9
10
λ(rest) (μm)
λ(rest) (μm)
λ(rest) (μm)

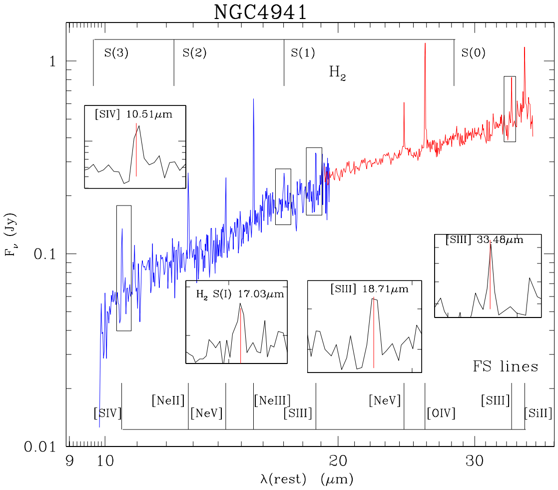
NGC4941
S(3)
S(2)
S(1)
S(0)
H$_2$
[SIV] 10.51μm
H$_2$ S(1) 17.03μm
[SIII] 18.71μm
[SIII] 33.48μm
FS lines
[SIV]
[NeII]
[NeV]
[NeIII]
[SIII]
[NeV]
[OIV]
[SIII]
[SiII]
1
0.1
0.01
F$_\nu$ (Jy)
9
10
20
30
λ(rest) (μm)

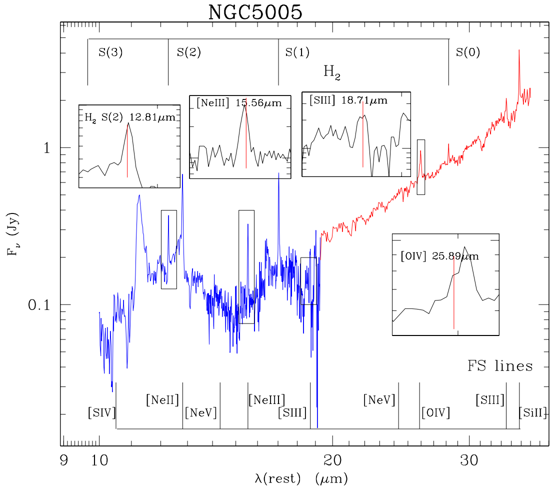
NGC5005
S(3)
S(2)
S(1)
S(0)
H$_2$
H$_2$ S(2) 12.81μm
[NeIII] 15.56μm
[SIII] 18.71μm
[OIV] 25.89μm
FS lines
[SIV]
[NeII]
[NeV]
[NeIII]
[SIII]
[NeV]
[OIV]
[SIII]
[SiII]
F$_\nu$ (Jy)
1
0.1
9
10
20
30
λ(rest) (μm)

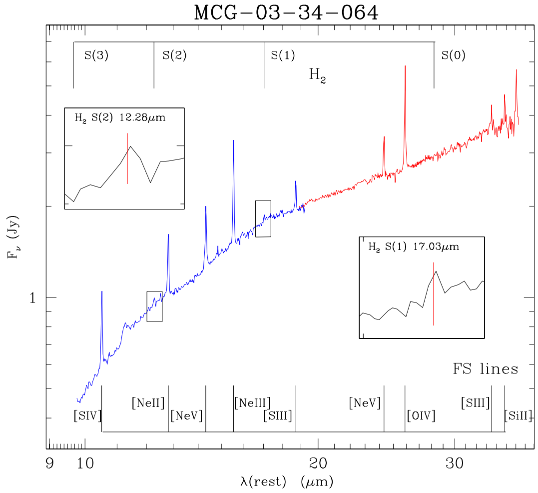
MCG−03−34−064
S(3)
S(2)
S(1)
S(0)
H$_2$
H$_2$ S(2) 12.28μm
H$_2$ S(1) 17.03μm
FS lines
[SIV]
[NeII]
[NeV]
[NeIII]
[SIII]
[NeV]
[OIV]
[SIII]
[SiII]
F$_\nu$ (Jy)
1
9
10
20
30
λ(rest) (μm)

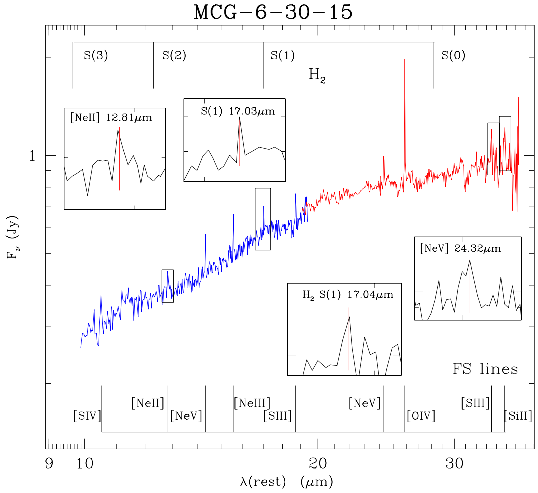
MCG−6−30−15
S(3)
S(2)
S(1)
S(0)
H$_2$
[NeII] 12.81μm
S(1) 17.03μm
H$_2$ S(1) 17.04μm
[NeV] 24.32μm
FS lines
[SIV]
[NeII]
[NeV]
[NeIII]
[SIII]
[NeV]
[OIV]
[SIII]
[SiII]
F$_\nu$ (Jy)
1
9
10
20
30
λ(rest) (μm)

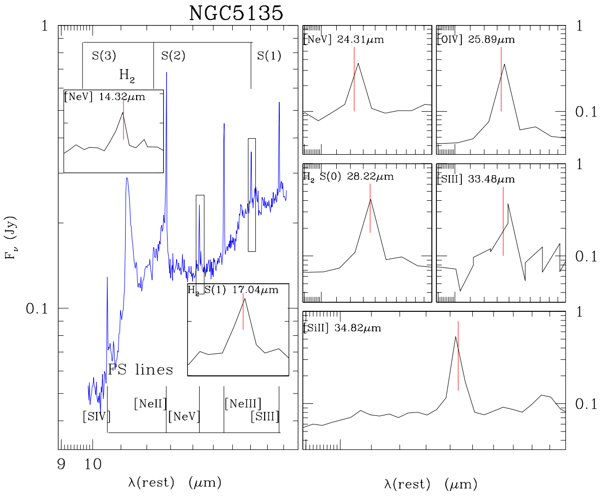
NGC5135
S(3)
S(2)
S(1)
H$_2$
[NeV] 14.32μm
H$_2$ S(1) 17.04μm
FS lines
[SIV]
[NeII]
[NeV]
[NeIII]
[SIII]
[NeV] 24.31μm
[OIV] 25.89μm
H$_2$ S(0) 28.22μm
[SIII] 33.48μm
[SiII] 34.82μm
F$_\nu$ (Jy)
1
0.1
9
10
λ(rest) (μm)
λ(rest) (μm)

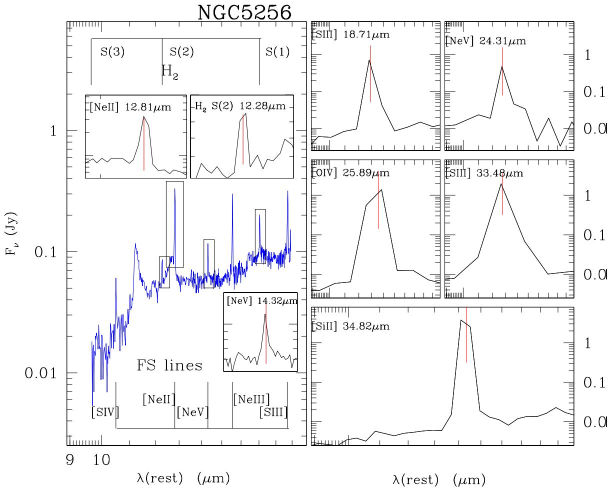
NGC5256
S(3)
S(2)
S(1)
H$_2$
[NeII] 12.81μm
H$_2$ S(2) 12.28μm
[NeV] 14.32μm
FS lines
[SIV]
[NeII]
[NeV]
[NeIII]
[SIII]
[SIII] 18.71μm
[NeV] 24.31μm
[OIV] 25.89μm
[SIII] 33.48μm
[SiII] 34.82μm
F$_\nu$ (Jy)
1
0.1
0.01
9
10
λ(rest) (μm)
λ(rest) (μm)

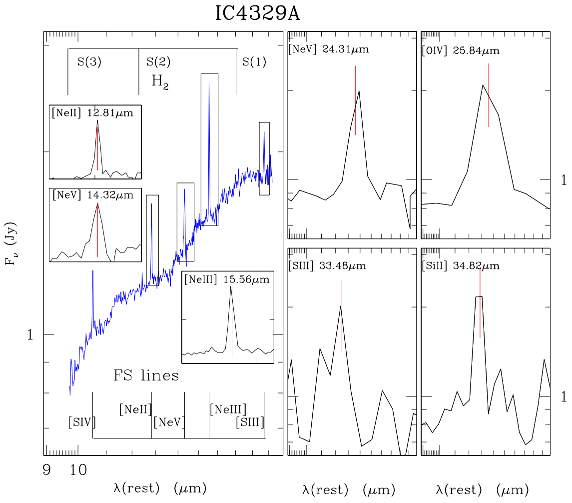
IC4329A
S(3)
S(2)
S(1)
H$_2$
[NeII] 12.81μm
[NeV] 14.32μm
[NeIII] 15.56μm
FS lines
[SIV]
[NeII]
[NeV]
[NeIII]
[SIII]
[NeV] 24.31μm
[OIV] 25.84μm
[SIII] 33.48μm
[SiII] 34.82μm
F$_\nu$ (Jy)
1
9
10
λ(rest) (μm)
λ(rest) (μm)
λ(rest) (μm)

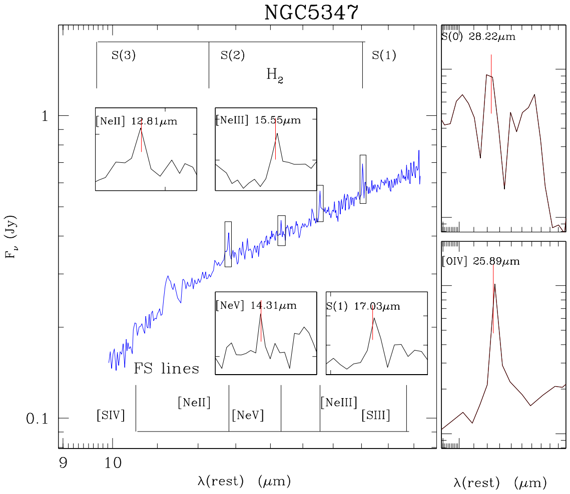
NGC5347
S(3)
S(2)
S(1)
H_2
[NeII] 12.81μm
[NeIII] 15.55μm
[NeV] 14.31μm
S(1) 17.03μm
FS lines
[SIV]
[NeII]
[NeV]
[NeIII]
[SIII]
S(0) 28.22μm
[OIV] 25.89μm
1
0.1
9
10
F_ν (Jy)
λ(rest) (μm)

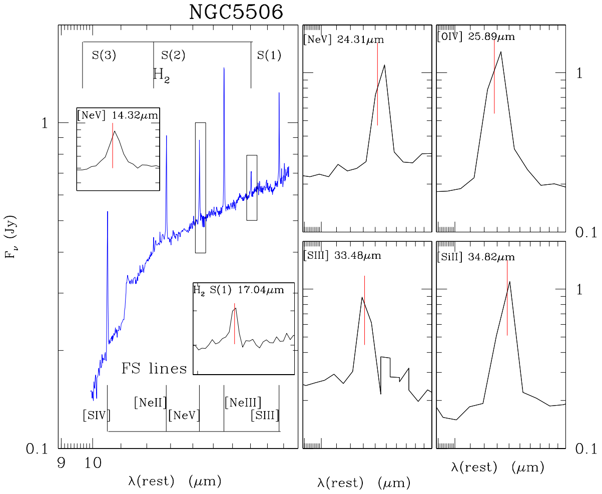
NGC5506
S(3)
S(2)
S(1)
H_2
[NeV] 14.32μm
H_2 S(1) 17.04μm
FS lines
[SIV]
[NeII]
[NeV]
[NeIII]
[SIII]
[NeV] 24.31μm
[OIV] 25.89μm
[SIII] 33.48μm
[SiII] 34.82μm
1
0.1
9
10
F_ν (Jy)
λ(rest) (μm)

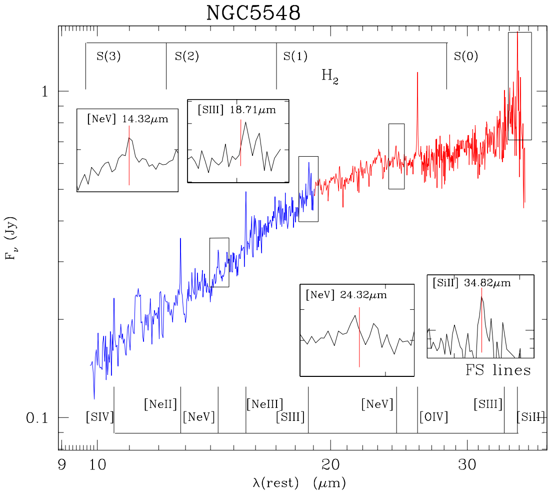
NGC5548
S(3)
S(2)
S(1)
S(0)
H_2
[NeV] 14.32μm
[SIII] 18.71μm
[NeV] 24.32μm
[SiII] 34.82μm
FS lines
[SIV]
[NeII]
[NeV]
[NeIII]
[SIII]
[NeV]
[OIV]
[SIII]
[SiII]
1
0.1
9
10
20
30
F_ν (Jy)
λ(rest) (μm)

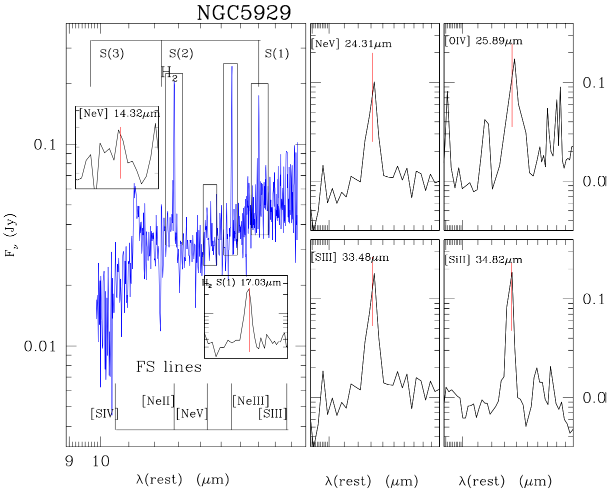
NGC5929
S(3)
S(2)
S(1)
H_2
[NeV] 14.32μm
H_2 S(1) 17.03μm
FS lines
[SIV]
[NeII]
[NeV]
[NeIII]
[SIII]
[NeV] 24.31μm
[OIV] 25.89μm
[SIII] 33.48μm
[SiII] 34.82μm
0.1
0.01
0.0
9
10
F_ν (Jy)
λ(rest) (μm)

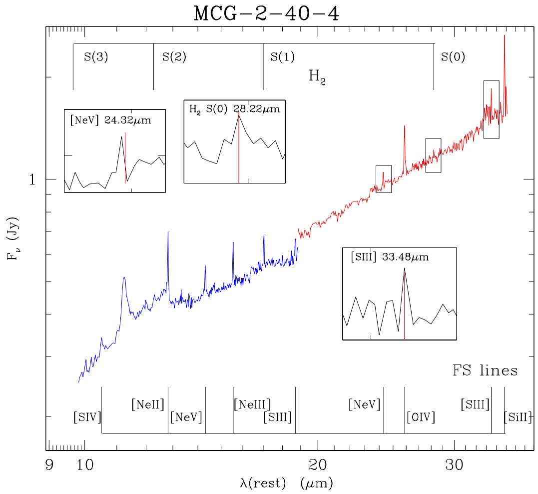
MCG−2−40−4
S(3)
S(2)
S(1)
S(0)
H_2
[NeV] 24.32μm
H_2 S(0) 28.22μm
[SIII] 33.48μm
FS lines
[SIV]
[NeII]
[NeV]
[NeIII]
[SIII]
[NeV]
[OIV]
[SIII]
[SiII]
1
9
10
20
30
F_ν (Jy)
λ(rest) (μm)

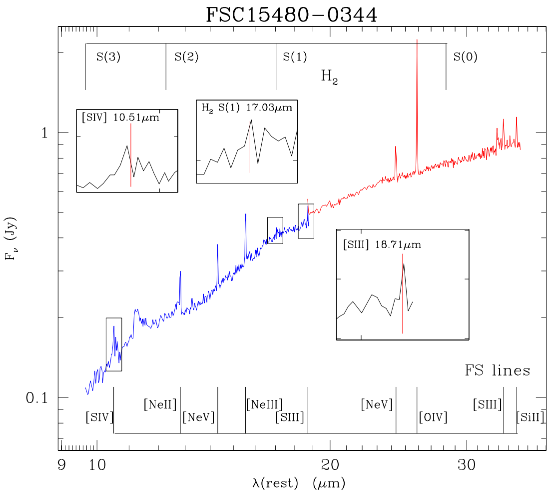
FSC15480−0344
S(3)
S(2)
S(1)
S(0)
H_2
[SIV] 10.51μm
H_2 S(1) 17.03μm
[SIII] 18.71μm
FS lines
[SIV]
[NeII]
[NeV]
[NeIII]
[SIII]
[NeV]
[OIV]
[SIII]
[SiII]
1
0.1
9
10
20
30
F_ν (Jy)
λ(rest) (μm)

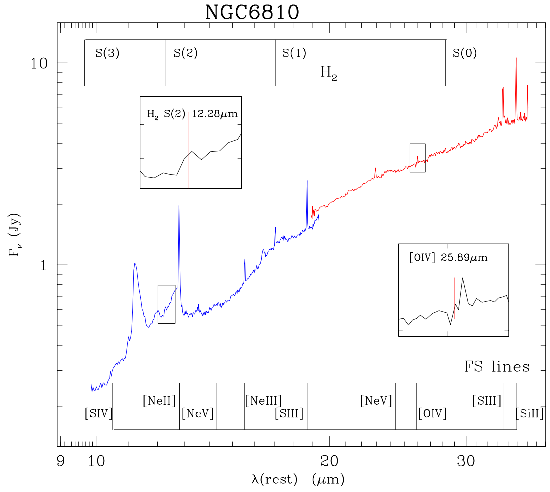
NGC6810
S(3)
S(2)
S(1)
S(0)
H_2
H_2 S(2) 12.28μm
[OIV] 25.89μm
FS lines
[SIV]
[NeII]
[NeV]
[NeIII]
[SIII]
[NeV]
[OIV]
[SIII]
[SiII]
F_ν (Jy)
10
1
9
10
20
30
λ(rest) (μm)

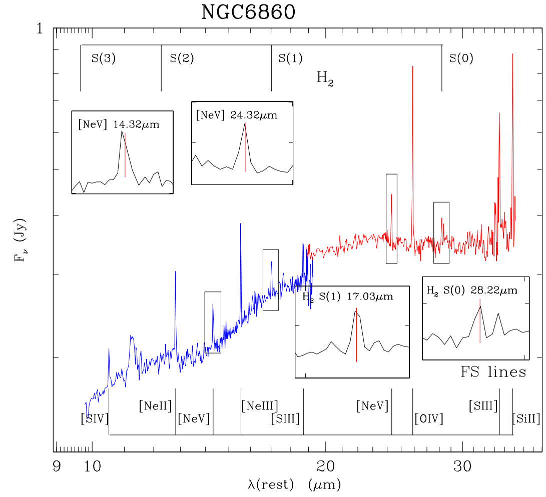
NGC6860
S(3)
S(2)
S(1)
S(0)
H_2
[NeV] 14.32μm
[NeV] 24.32μm
H_2 S(1) 17.03μm
H_2 S(0) 28.22μm
FS lines
[SIV]
[NeII]
[NeV]
[NeIII]
[SIII]
[NeV]
[OIV]
[SIII]
[SiII]
F_ν (Jy)
1
9
10
20
30
λ(rest) (μm)

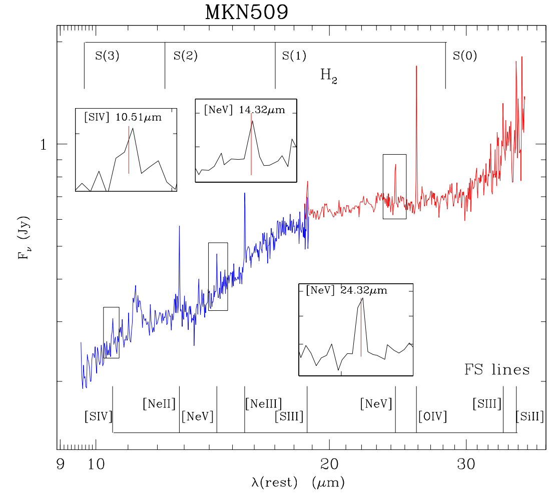
MKN509
S(3)
S(2)
S(1)
S(0)
H_2
[SIV] 10.51μm
[NeV] 14.32μm
[NeV] 24.32μm
FS lines
[SIV]
[NeII]
[NeV]
[NeIII]
[SIII]
[NeV]
[OIV]
[SIII]
[SiII]
F_ν (Jy)
1
9
10
20
30
λ(rest) (μm)

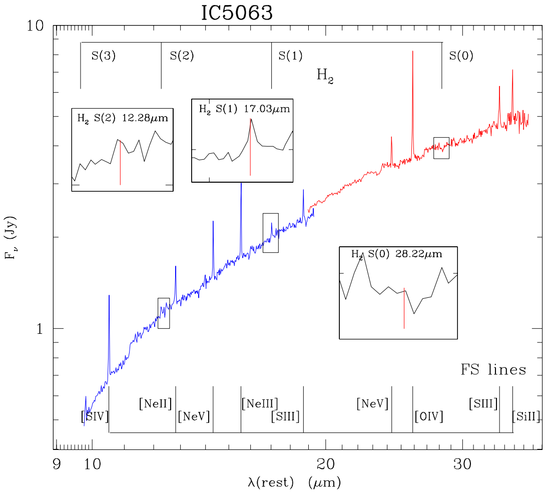
IC5063
S(3)
S(2)
S(1)
S(0)
H_2
H_2 S(2) 12.28μm
H_2 S(1) 17.03μm
H_2 S(0) 28.22μm
FS lines
[SIV]
[NeII]
[NeV]
[NeIII]
[SIII]
[NeV]
[OIV]
[SIII]
[SiII]
F_ν (Jy)
10
1
9
10
20
30
λ(rest) (μm)

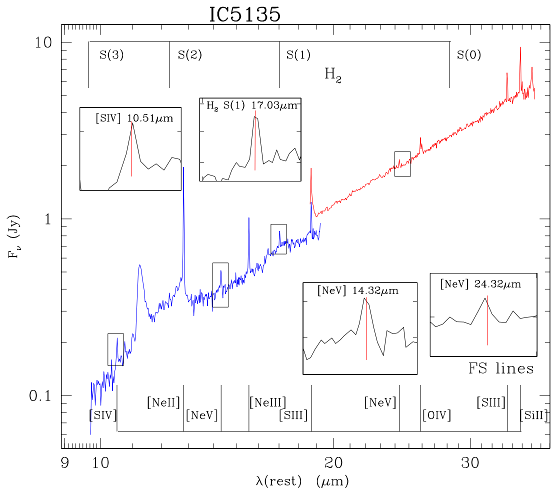
IC5135
S(3)
S(2)
S(1)
S(0)
H_2
[SIV] 10.51μm
H_2 S(1) 17.03μm
[NeV] 14.32μm
[NeV] 24.32μm
FS lines
[SIV]
[NeII]
[NeV]
[NeIII]
[SIII]
[NeV]
[OIV]
[SIII]
[SiII]
F_ν (Jy)
10
1
0.1
9
10
20
30
λ(rest) (μm)

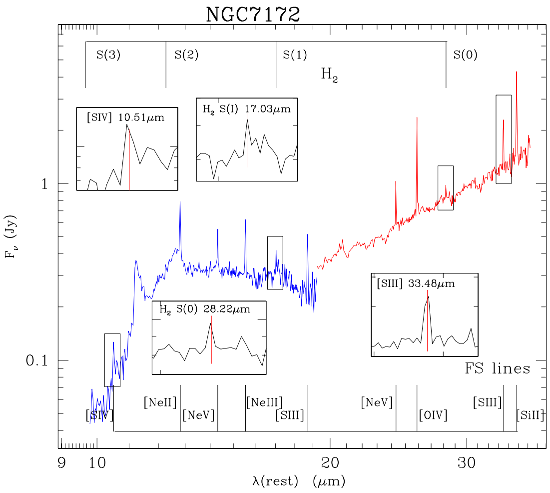
NGC7172
S(3)
S(2)
S(1)
S(0)
H_2
[SIV] 10.51μm
H_2 S(l) 17.03μm
H_2 S(0) 28.22μm
[SIII] 33.48μm
FS lines
[SIV]
[NeII]
[NeV]
[NeIII]
[SIII]
[NeV]
[OIV]
[SIII]
[SiII]
F_ν (Jy)
1
0.1
9
10
20
30
λ(rest) (μm)

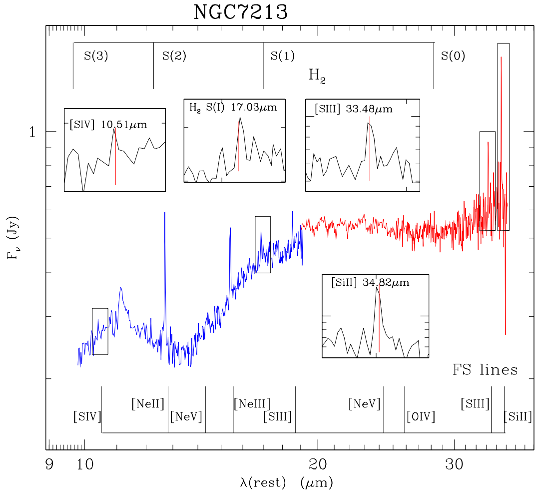
NGC7213
S(3)
S(2)
S(1)
S(0)
H$_2$
[SIV] 10.51μm
H$_2$ S(1) 17.03μm
[SIII] 33.48μm
[SiII] 34.82μm
FS lines
[SIV]
[NeII]
[NeV]
[NeIII]
[SIII]
[NeV]
[OIV]
[SIII]
[SiII]
F$_\nu$ (Jy)
1
9
10
20
30
λ(rest) (μm)

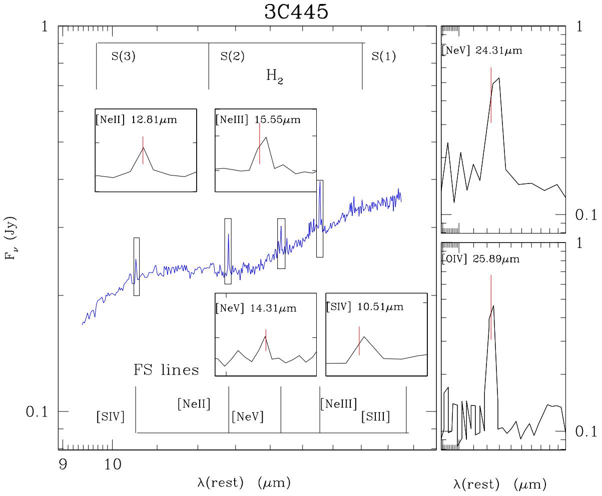
3C445
S(3)
S(2)
S(1)
H$_2$
[NeII] 12.81μm
[NeIII] 15.55μm
[NeV] 14.31μm
[SIV] 10.51μm
FS lines
[SIV]
[NeII]
[NeV]
[NeIII]
[SIII]
[NeV] 24.31μm
[OIV] 25.89μm
F$_\nu$ (Jy)
1
0.1
9
10
λ(rest) (μm)

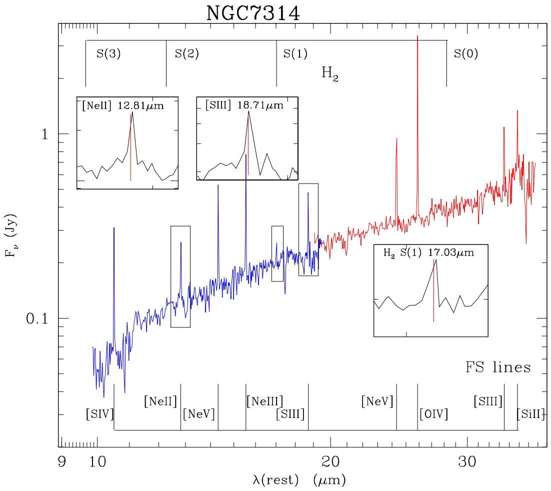
NGC7314
S(3)
S(2)
S(1)
S(0)
H$_2$
[NeII] 12.81μm
[SIII] 18.71μm
H$_2$ S(1) 17.03μm
FS lines
[SIV]
[NeII]
[NeV]
[NeIII]
[SIII]
[NeV]
[OIV]
[SIII]
[SiII]
F$_\nu$ (Jy)
1
0.1
9
10
20
30
λ(rest) (μm)

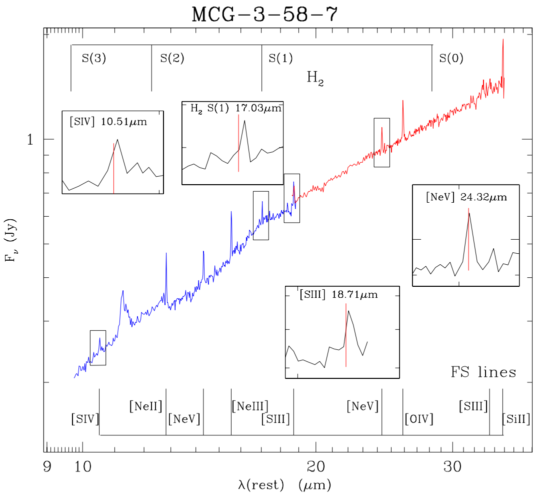
MCG−3−58−7
S(3)
S(2)
S(1)
S(0)
H$_2$
[SIV] 10.51μm
H$_2$ S(1) 17.03μm
[NeV] 24.32μm
[SIII] 18.71μm
FS lines
[SIV]
[NeII]
[NeV]
[NeIII]
[SIII]
[NeV]
[OIV]
[SIII]
[SiII]
F$_\nu$ (Jy)
1
9
10
20
30
λ(rest) (μm)

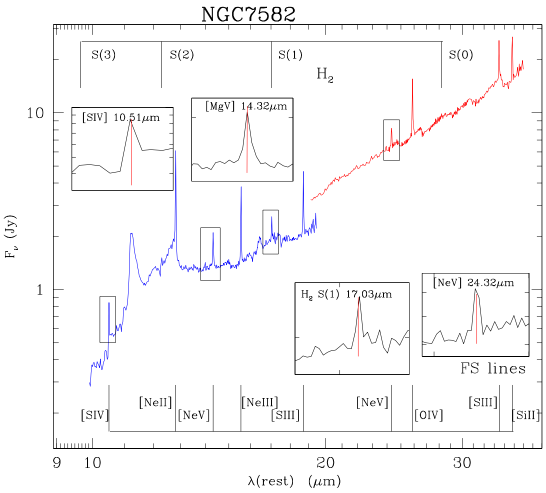
NGC7582
S(3)
S(2)
S(1)
S(0)
H$_2$
[SIV] 10.51μm
[MgV] 14.32μm
H$_2$ S(1) 17.03μm
[NeV] 24.32μm
FS lines
[SIV]
[NeII]
[NeV]
[NeIII]
[SIII]
[NeV]
[OIV]
[SIII]
[SiII]
F$_\nu$ (Jy)
10
1
9
10
20
30
λ(rest) (μm)

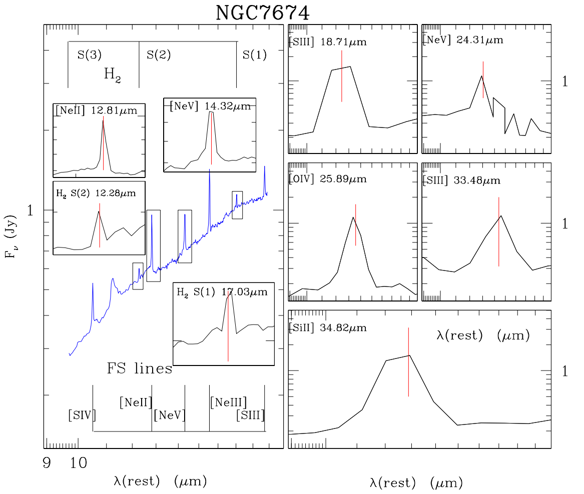
NGC7674
S(3)
S(2)
S(1)
H$_2$
[NeII] 12.81μm
[NeV] 14.32μm
H$_2$ S(2) 12.28μm
H$_2$ S(1) 17.03μm
FS lines
[SIV]
[NeII]
[NeV]
[NeIII]
[SIII]
[SIII] 18.71μm
[NeV] 24.31μm
[OIV] 25.89μm
[SIII] 33.48μm
[SiII] 34.82μm
λ(rest) (μm)
F$_\nu$ (Jy)
1
9
10
λ(rest) (μm)
λ(rest) (μm)

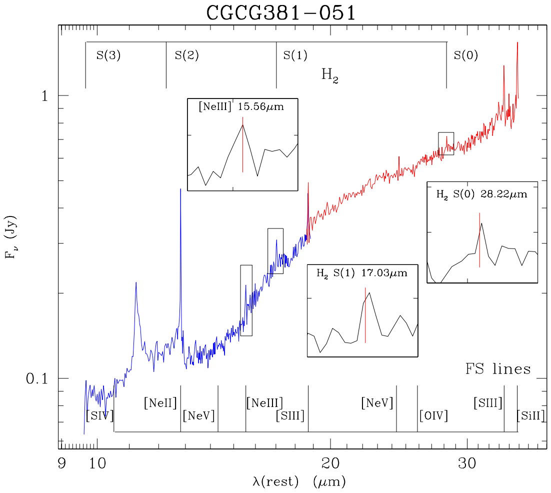
CGCG381−051
S(3)
S(2)
S(1)
S(0)
H$_2$
[NeIII] 15.56μm
H$_2$ S(0) 28.22μm
H$_2$ S(1) 17.03μm
FS lines
[SIV]
[NeII]
[NeV]
[NeIII]
[SIII]
[NeV]
[OIV]
[SIII]
[SiII]
F$_\nu$ (Jy)
1
0.1
9
10
20
30
λ(rest) (μm)

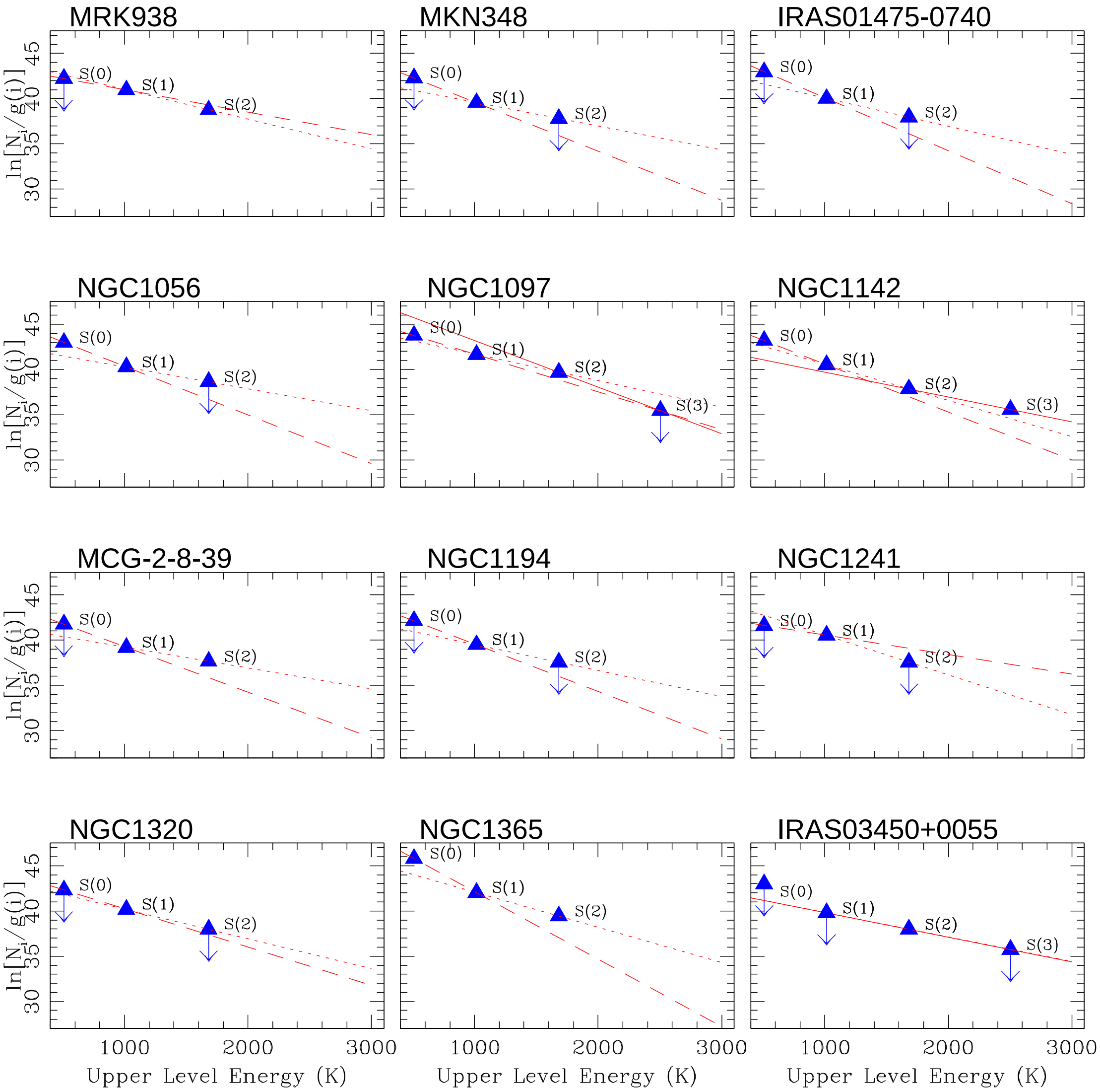

FIG. 2.— H$_2$ excitation diagrams. For each measured line, the natural logarithm of the level population normalized to its statistical weight is plotted against the upper level energy (in temperature units). For each pair of adjacent transitions the connecting line is shown, whose inverse value represents the gas temperature: the dashed line connects the S(0) and S(1) detections, the dotted line the S(1) and S(2), the solid line the S(2) and S(3). Upper limits have been used to obtain limiting slopes and hence limiting temperatures and masses (see text). Figures 2.12.43 are available in the online version of the Journal.

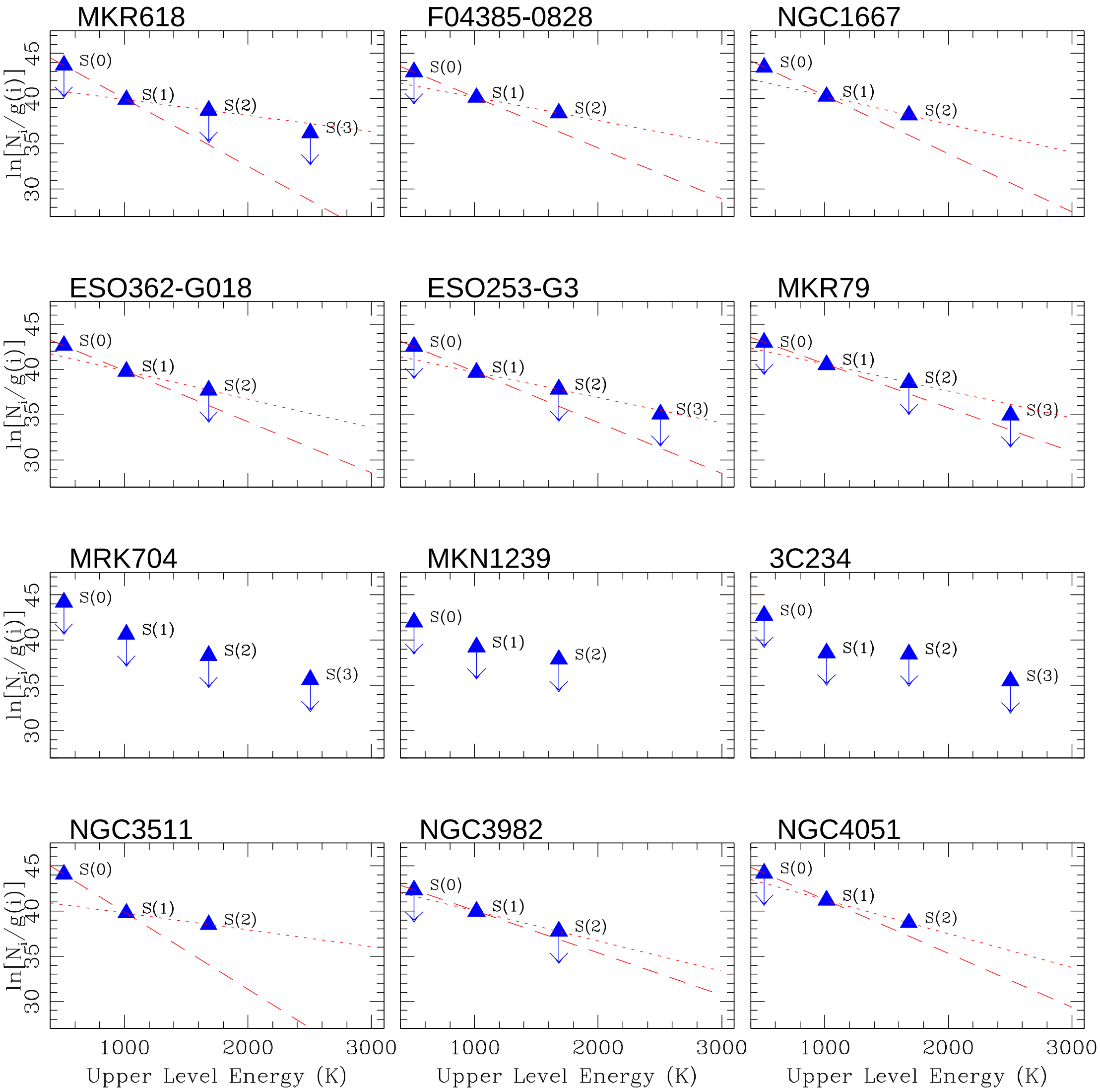
MKR618
F04385-0828
NGC1667
ESO362-G018
ESO253-G3
MKR79
MRK704
MKN1239
3C234
NGC3511
NGC3982
NGC4051
S(0)
S(1)
S(2)
S(3)
ln[N_i/g(i)]
30
35
40
45
1000
2000
3000
Upper Level Energy (K)

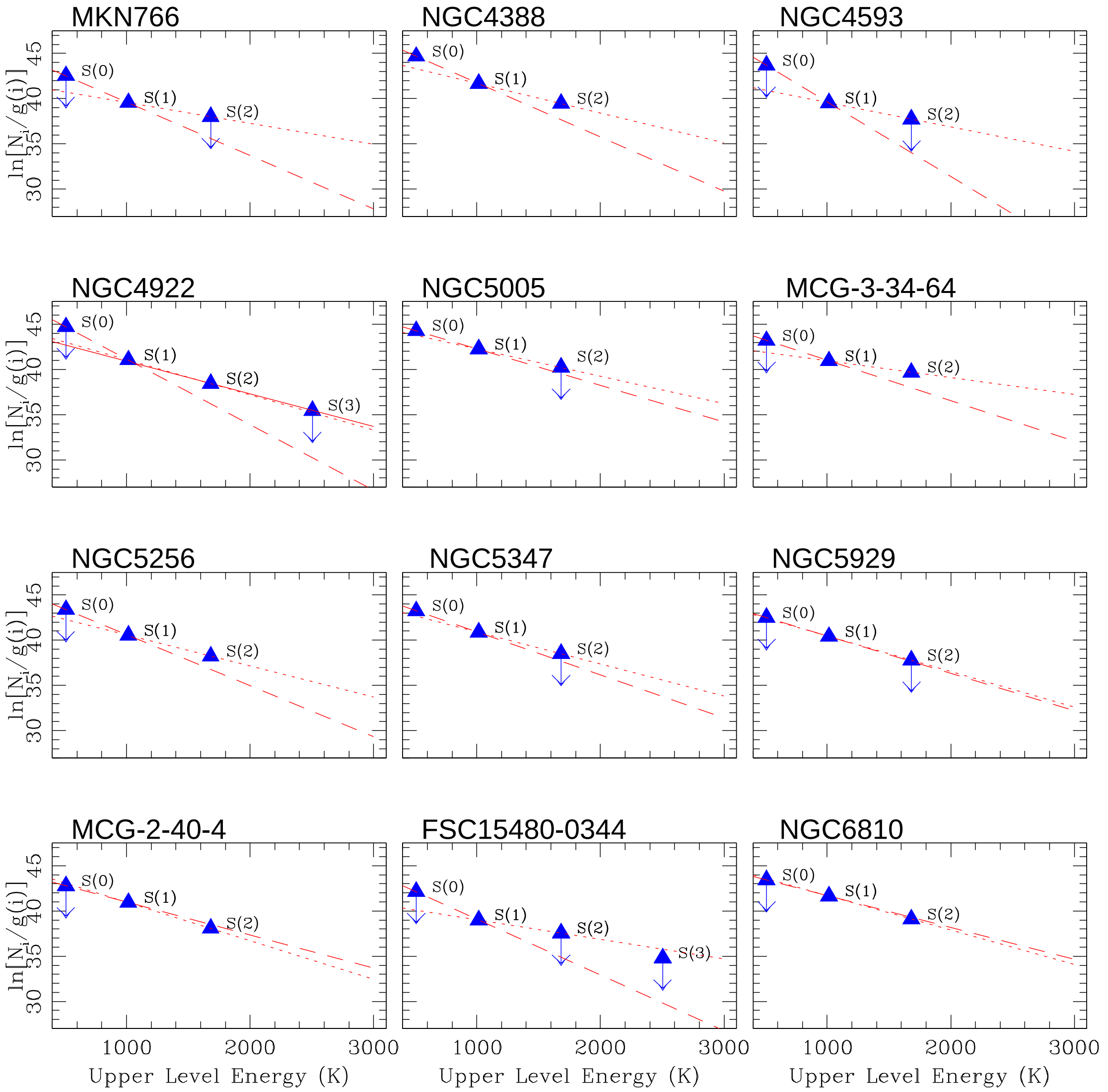
MKN766
NGC4388
NGC4593
NGC4922
NGC5005
MCG-3-34-64
NGC5256
NGC5347
NGC5929
MCG-2-40-4
FSC15480-0344
NGC6810
S(0)
S(1)
S(2)
S(3)
$\ln[N_i/g(i)]$
30
35
40
45
1000
2000
3000
Upper Level Energy (K)

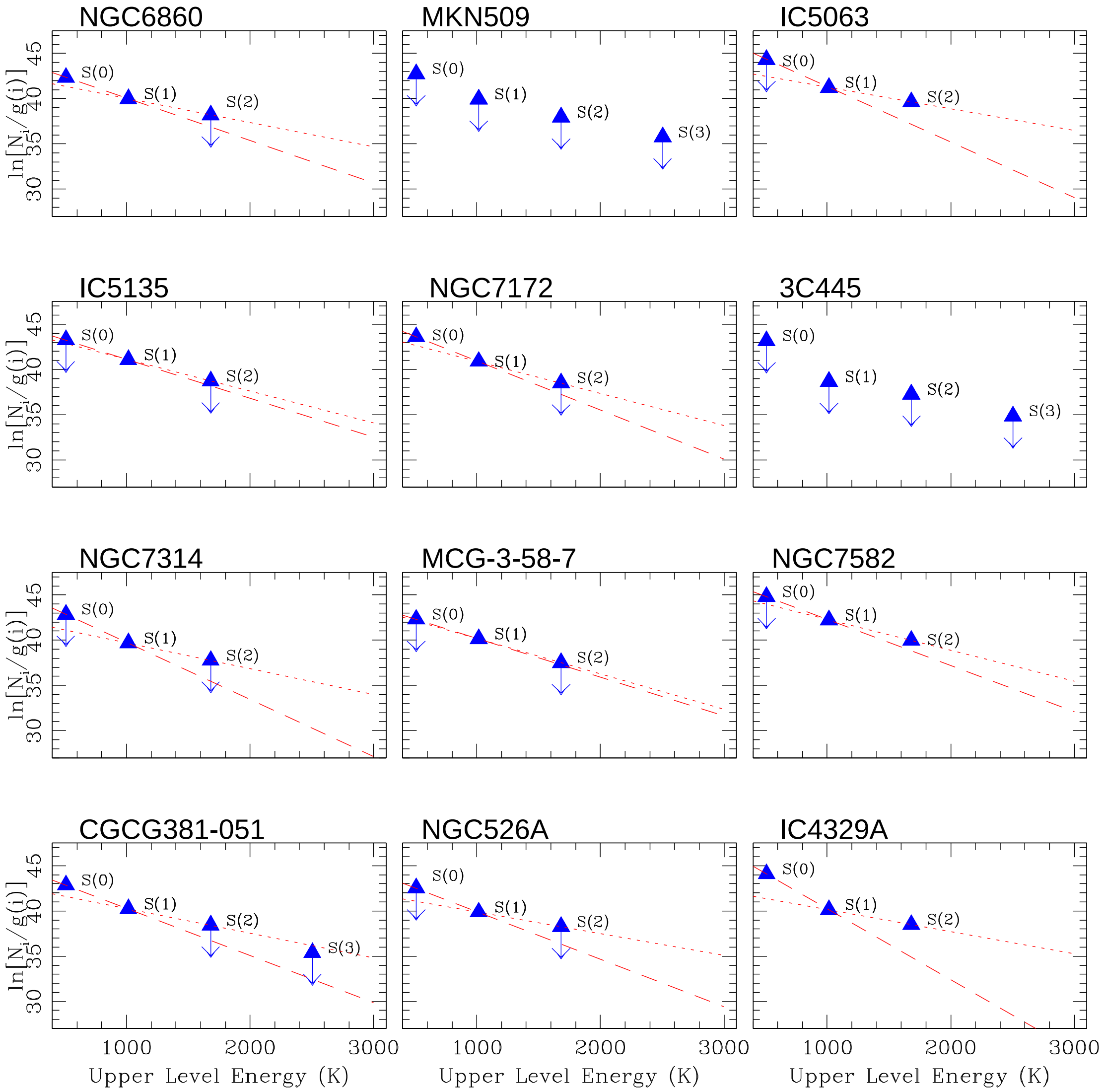
NGC6860
MKN509
IC5063
IC5135
NGC7172
3C445
NGC7314
MCG-3-58-7
NGC7582
CGCG381-051
NGC526A
IC4329A
S(0)
S(1)
S(2)
S(3)
$\ln[N_i/g(i)]$
30
35
40
45
1000
2000
3000
Upper Level Energy (K)

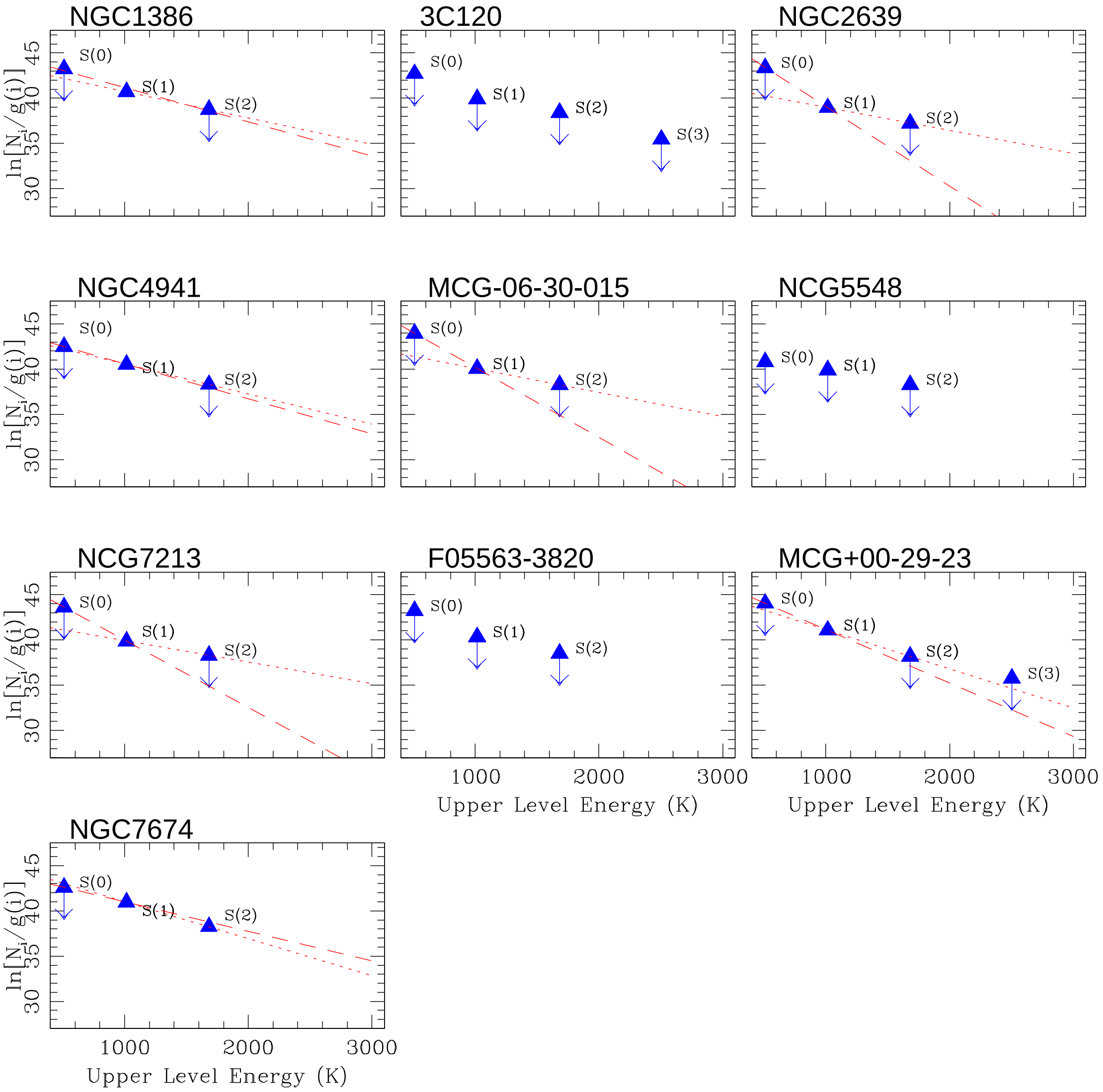
NGC1386
3C120
NGC2639
NGC4941
MCG-06-30-015
NCG5548
NCG7213
F05563-3820
MCG+00-29-23
NGC7674
S(0)
S(1)
S(2)
S(3)
ln[N$_i$/g(i)]
30
35
40
45
1000
2000
3000
Upper Level Energy (K)

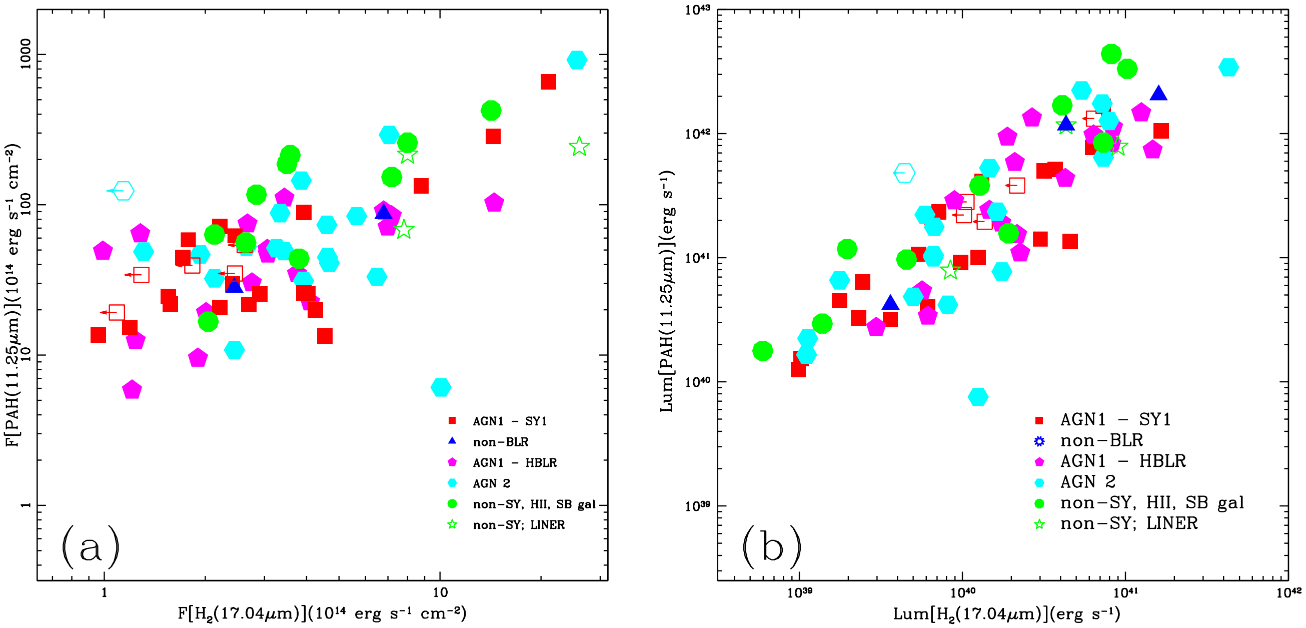

FIG. 3.— **a:** H_2 17.04 μm line flux versus PAH 11.25μm integrated flux. **b:** H_2 17.04 μm line luminosity versus PAH 11.25μm luminosity.

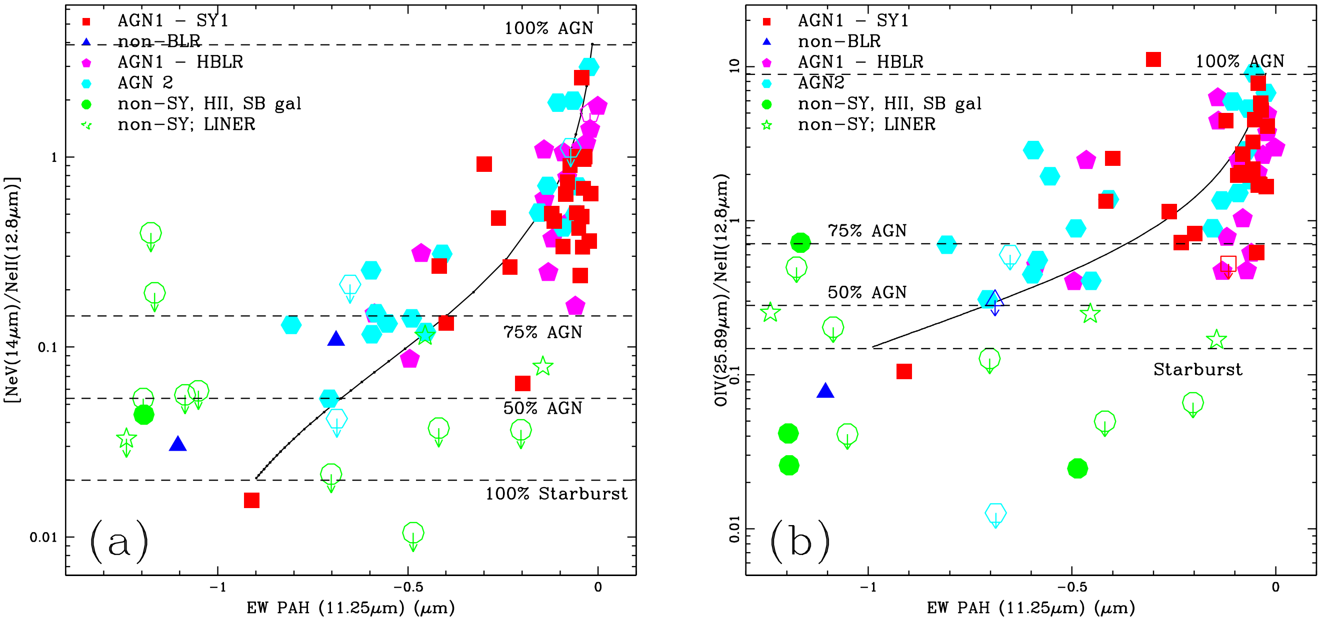

FIG. 4.— **a:** The PAH 11.25μm equivalent width versus [NeV]14.3μm/[NeII]12.8μm line ratio. The black line shows the behaviour of the analytical model for this diagram. **b:** The PAH 11.25μm equivalent width versus [OIV]25.9μm/[NeII]12.8μm line ratio. The black line as in Fig. 4a.

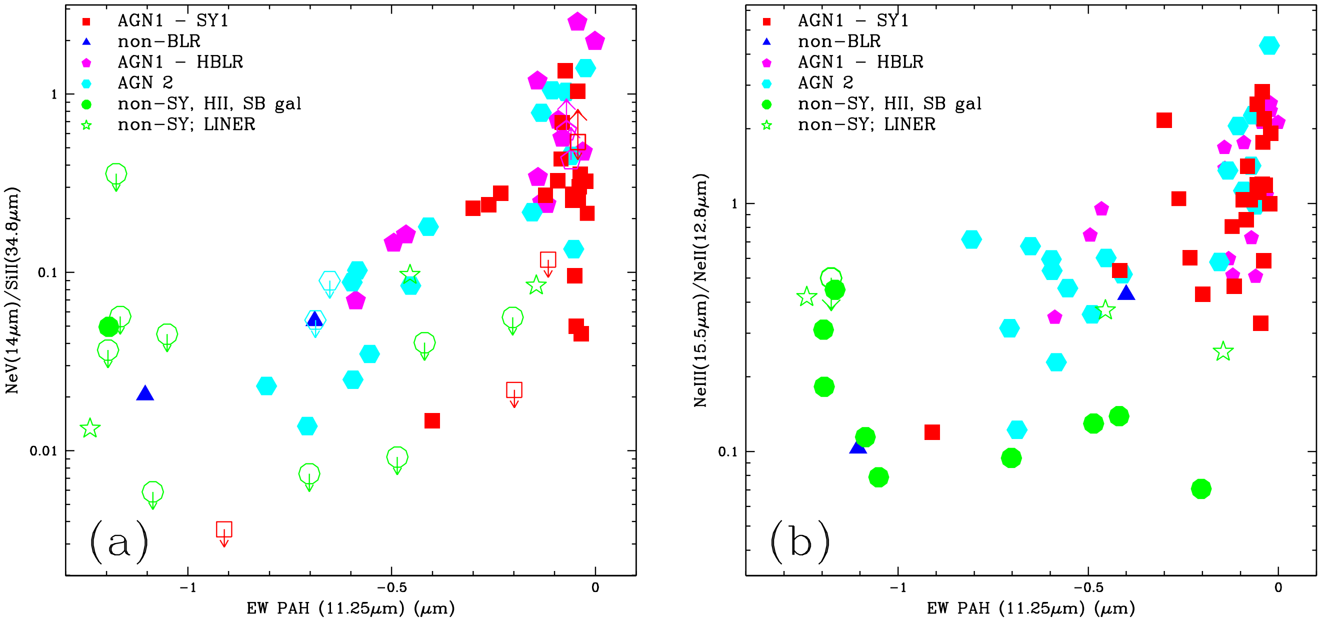

FIG. 5.— **a:** The PAH 11.25μm equivalent width versus [NeV]14.3μm/[SiII]34.8μm line ratio. **b:** [NeIII]15.5μm/[NeII]12.8μm line ratio versus the PAH 11.25μm equivalent width.

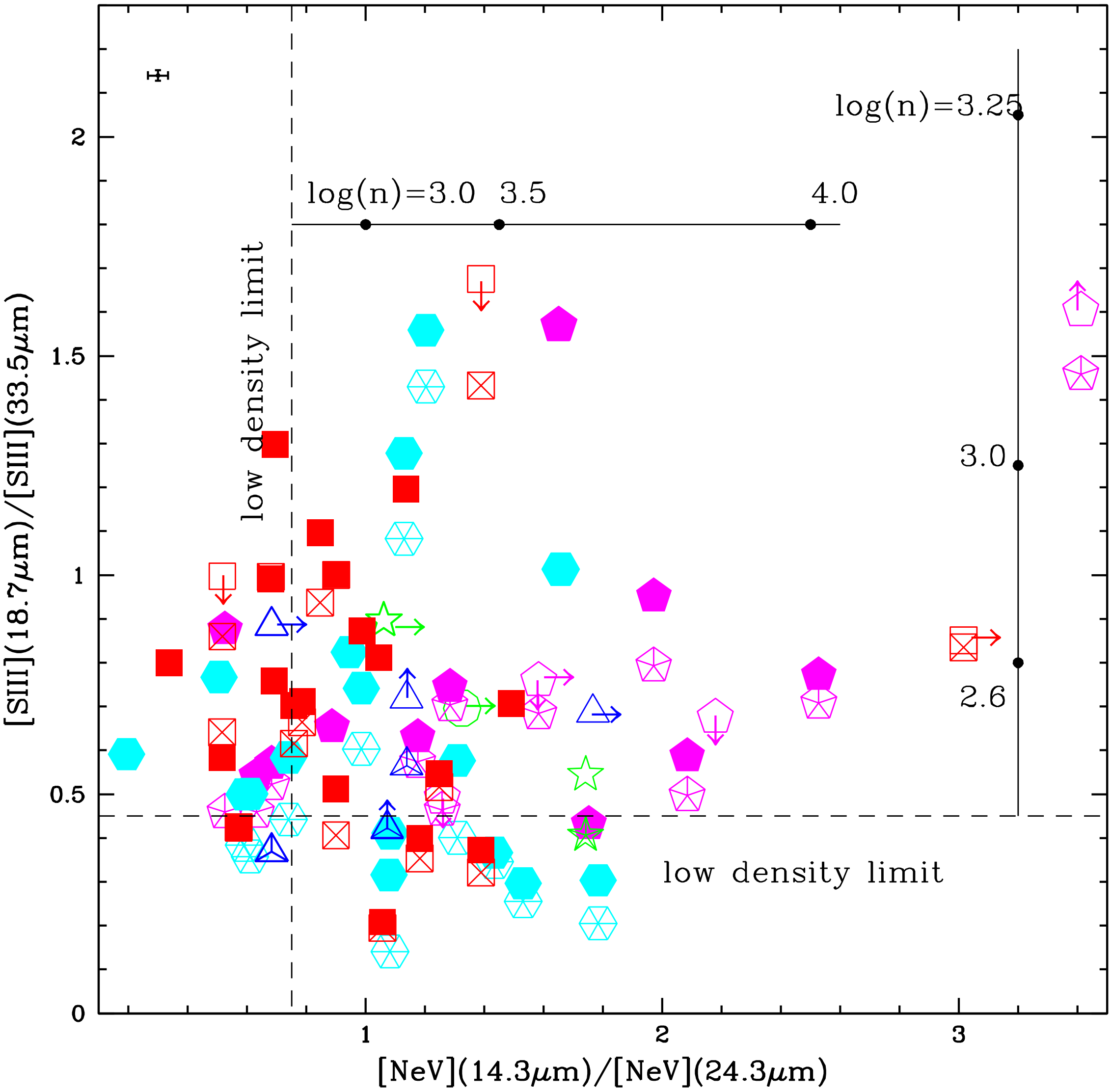

Fig. 6.— [NeV]14.3μm/[NeV]24.3μm line ratio versus the [SIII]18.7μm/[SIII]33.5μm line ratio. Symbols as in the previous figures, except for the open crossed symbols indicating the ratio of objects with small aperture [SIII]18.71μm measures and the filled symbols directly above them showing the aperture corrected [SIII] line ratio. The dashed lines show the low density limits (see text). The solid lines at the top and at the right give the corresponding electron densities.

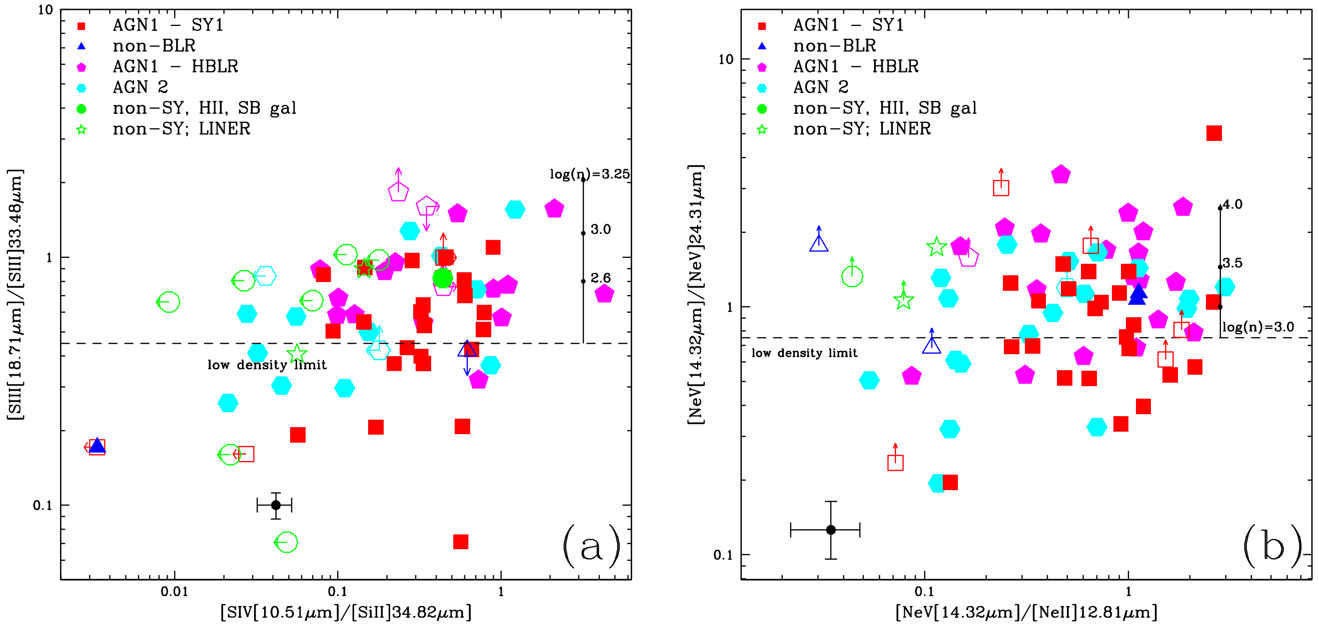

FIG. 7.— **a:** [SIV]10.51*μm*/[SiII]34.82*μm* line ratio versus the [SIII]18.7*μ*m/[SIII]33.5*μ*m line ratio. The [SIII]18.7*μ*m flux has been corrected by the extendedness 4.2. The average error bars are calculated with the propagation of the uncertainty from the mean line fluxes and their largest relative error of the sample sources' line measurements. Dashed and solid lines are as in the previous figure. **b:**[NeV]14.3*μ*m/[NeII]12.8*μ*m line ratio versus the [NeV]14.3*μ*m/[NeV]24.3*μ*m line ratio. Dashed and solid lines are as in the previous figure.

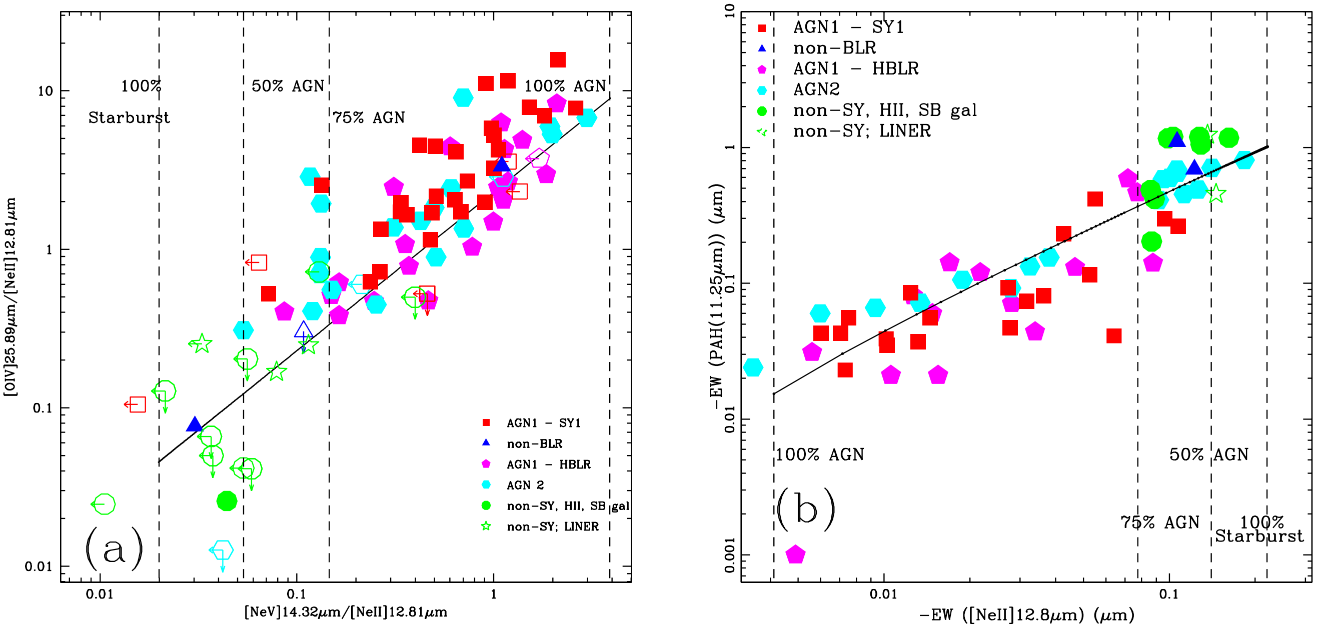

FIG. 8.— **a:** [NeV]14.3*μ*m/[NeII]12.8*μ*m line ratio versus the [OIV]25.9*μ*m/[NeII]12.8*μ*m line ratio. The black line shows the behaviour of the analytical model for this diagram. **b:** [NeII]12.8*μ*m equivalent width versus the PAH 11.25*μ*m equivalent width. We note that, for graphical reasons, in this diagram and in the following ones in which the equivalent widths, covering a large range, the logarithm of the inverse of the actual equivalent width is plotted. The black line shows the behaviour of the analytical model for this diagram.

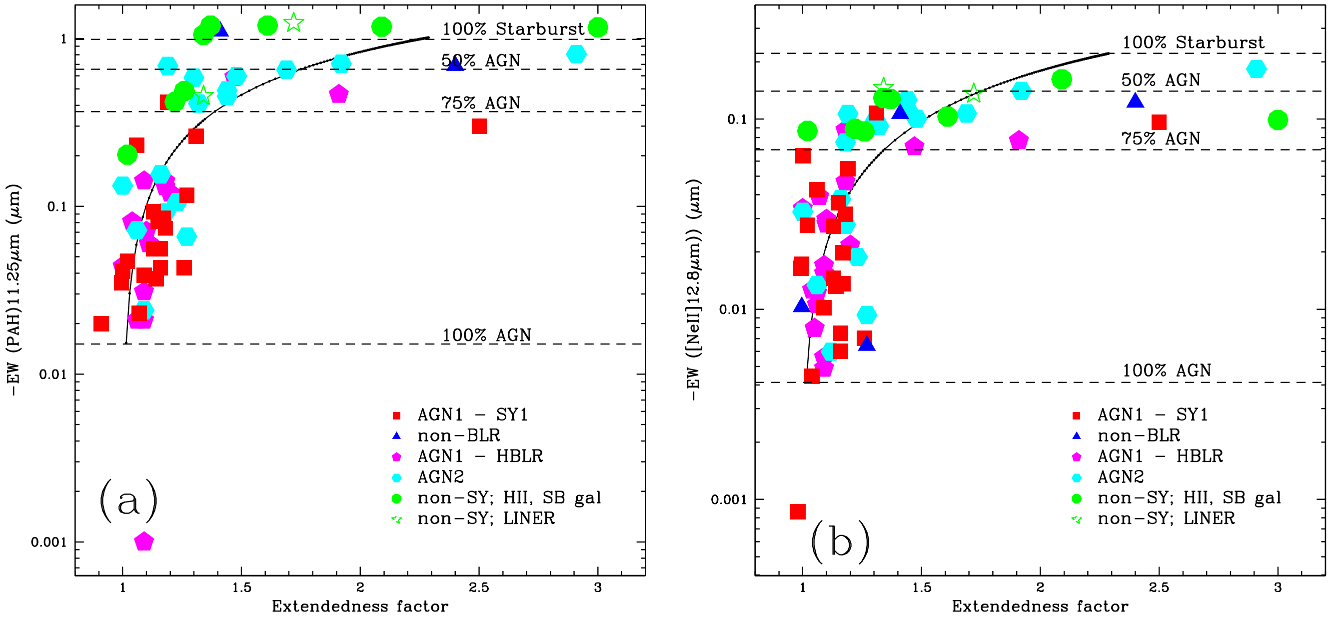

FIG. 9.— **a:** PAH 11.25μm equivalent widths versus extendness parameter. The black line shows the behaviour of the analytical model for this diagram. **b:** [NeII]12.8μm equivalent widths versus extendness parameter. The black line shows the behaviour of the analytical model for this diagram.

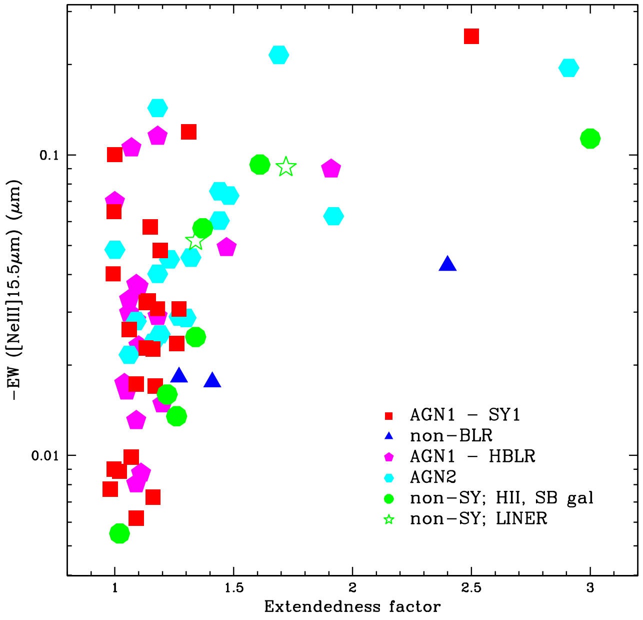

FIG. 10.— [NeIII]15.5μm line equivalent width versus extendness parameter.

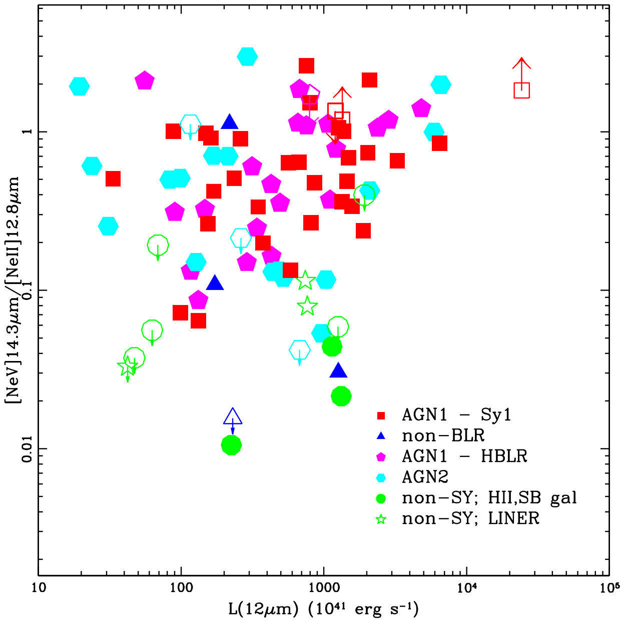

FIG. 11.— [NeV]14.3μm/[NeII]12.8μm line ratio versus 12μm luminosity.

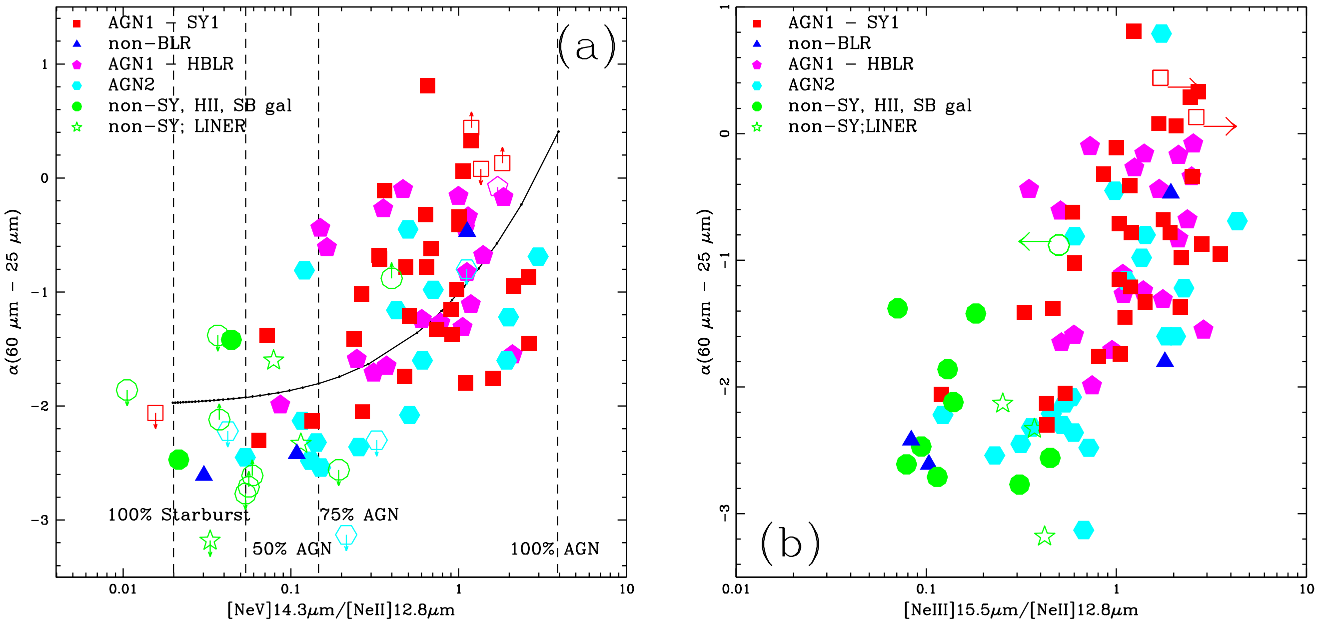

FIG. 12.— **a:** [NeV]14.3μm/[NeII]12.8μm line ratio versus the 60-25μm spectral index. The black line shows the behaviour of the analytical model for this diagram. **b:** [NeIII]15.5μm/[NeII]12.8μm line ratio versus the 60-25μm spectral index.

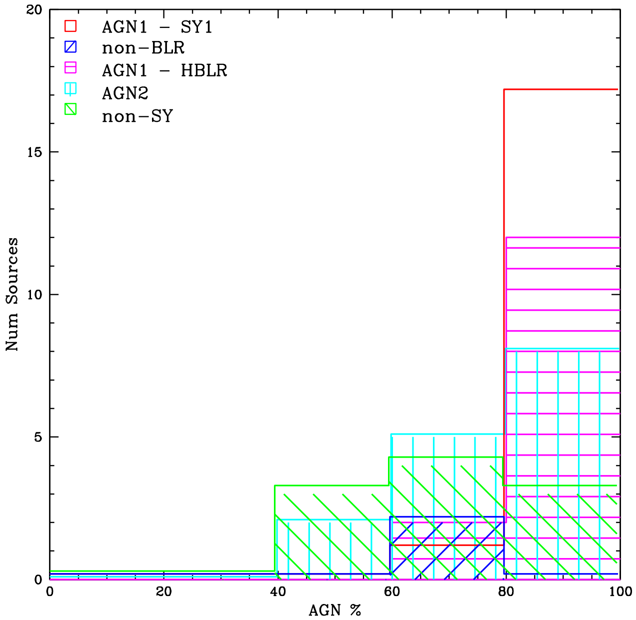

Fig. 13.— The histogram shows the percentage of AGN contribution.

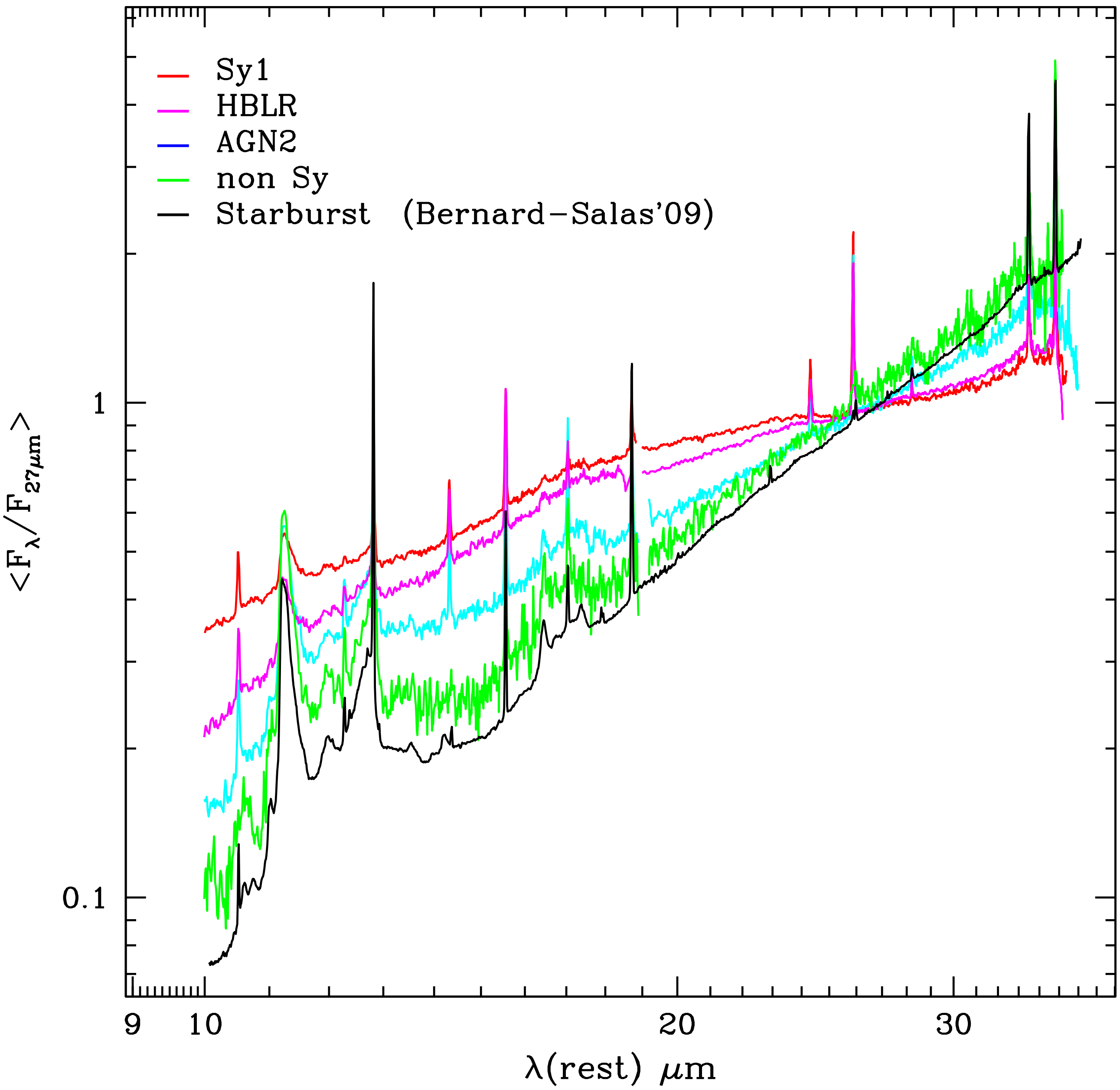

FIG. 14.— Average high resolution spectra for our classes of galaxies, compared with the mean high resolution spectrum of starburst galaxies.

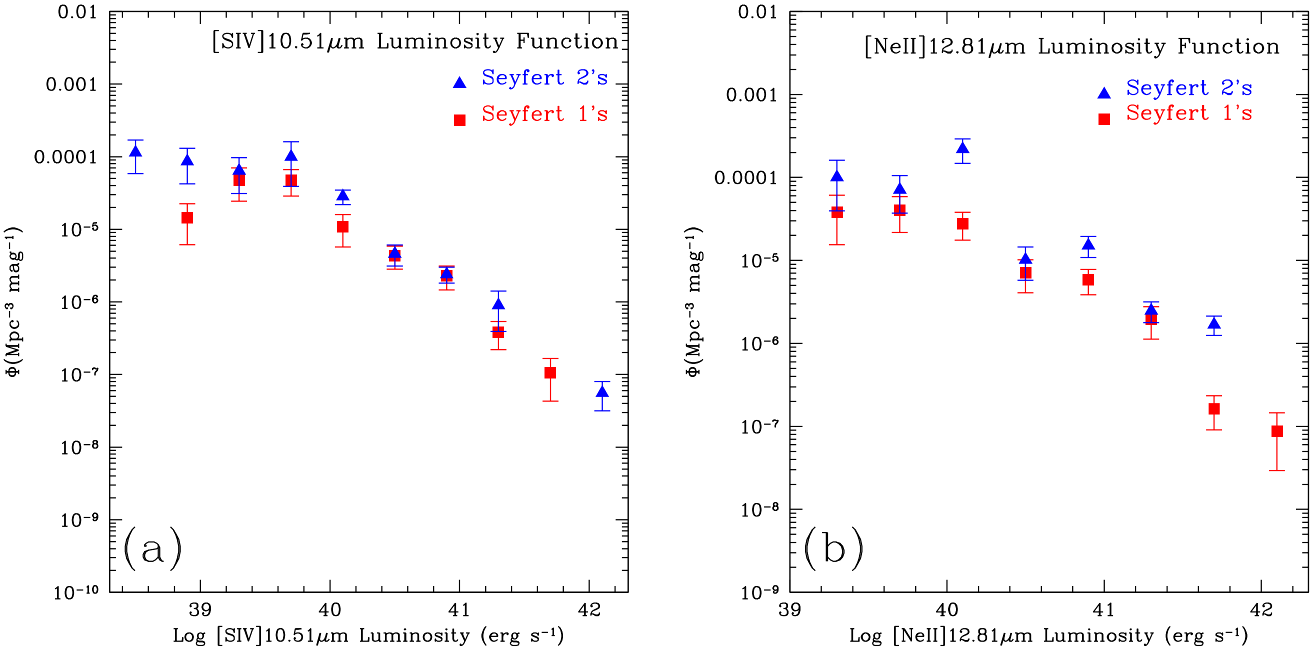

FIG. 15.— **a:** Line luminosity function of the [SIV]10.51*μm*, the red squares represent the Seyfert 1's and the blue triangles the Seyfert 2's. **b:** Line luminosity function of the [NeII]12.81*μm*, symbols are as in the previous figure.

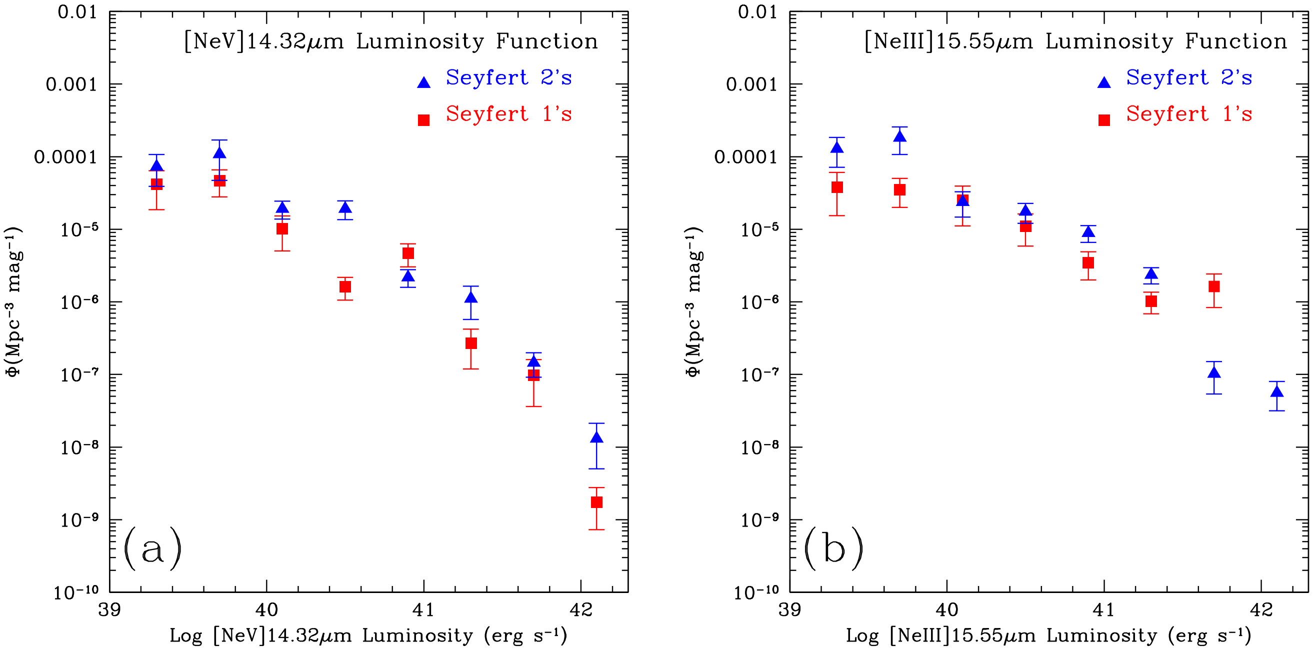

FIG. 16.— **a:** Line luminosity function of the [NeV]14.32*μm*, symbols are as in the previous figure. **b:** Line luminosity function of the [NeIII]15.55*μm*, symbols are as in the previous figure.

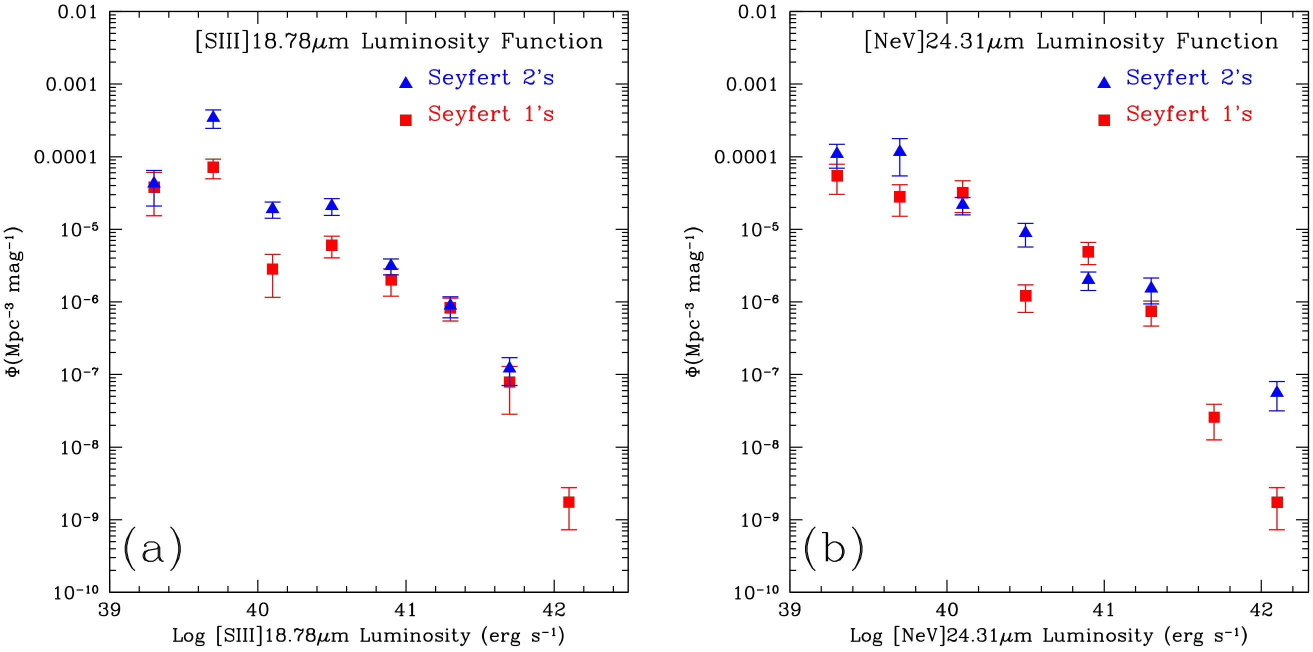

FIG. 17.— **a:** Line luminosity function of the [SIII]18.71μm, symbols are as in the previous figure. **b:** Line luminosity function of the [NeV]24.31μm, symbols are as in the previous figure.

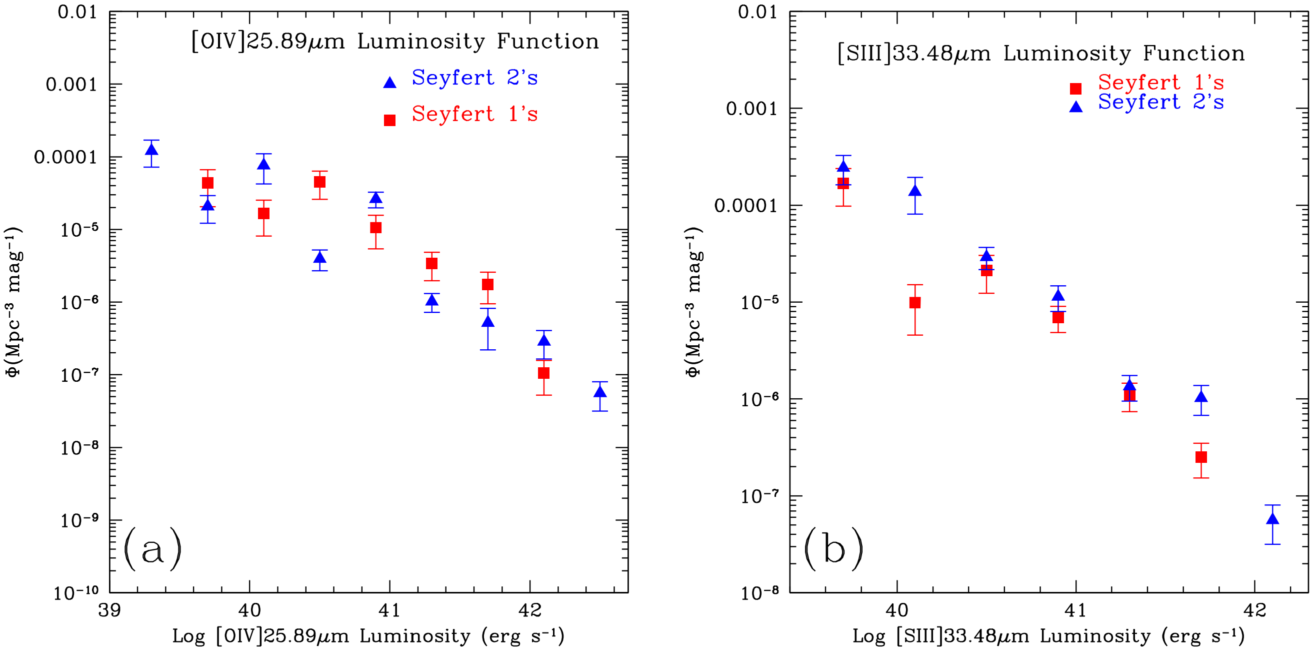

FIG. 18.— **a:** Line luminosity function of the [OIV]25.89μm, symbols are as in the previous figure. **b:** Line luminosity function of the [SIII]33.48μm, symbols are as in the previous figure.

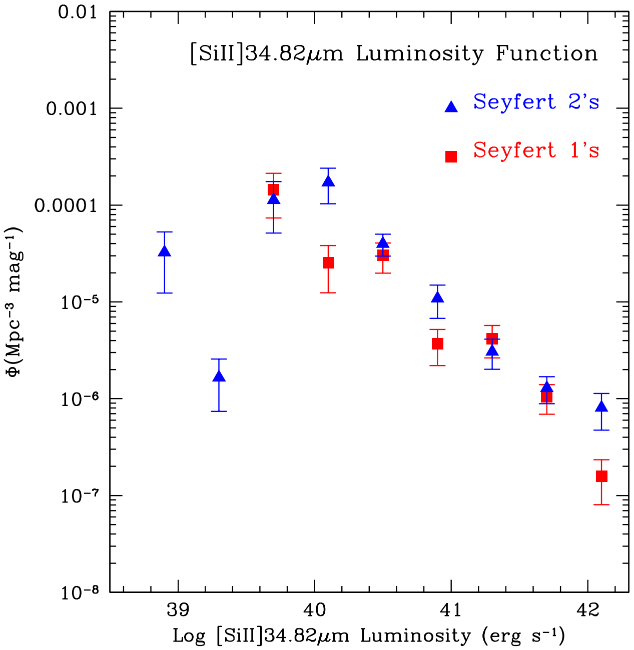

FIG. 19.— Line luminosity function of the [SiII]34.82*mum*, symbols are as in the previous figure.

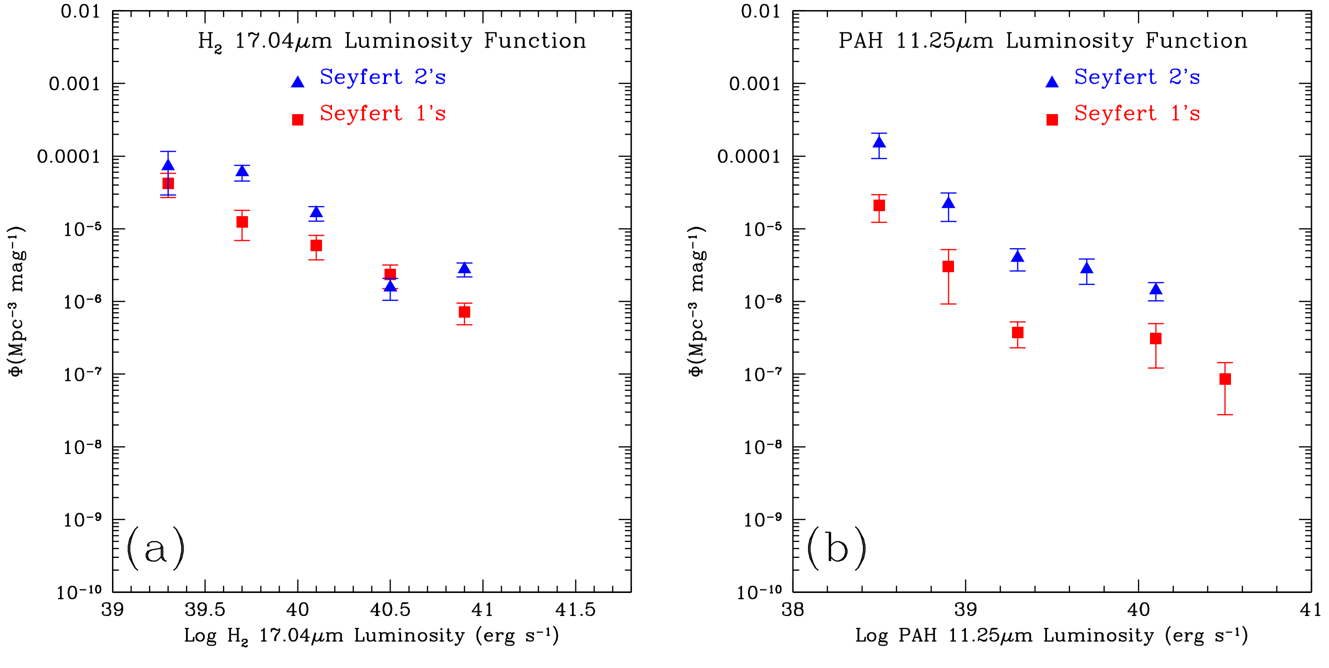

FIG. 20.— **a:** Line luminosity function of the H_2 17.04μm, symbols are as in the previous figure. **b:** Line luminosity function of the PAH 11.25μm, symbols are as in the previous figure.

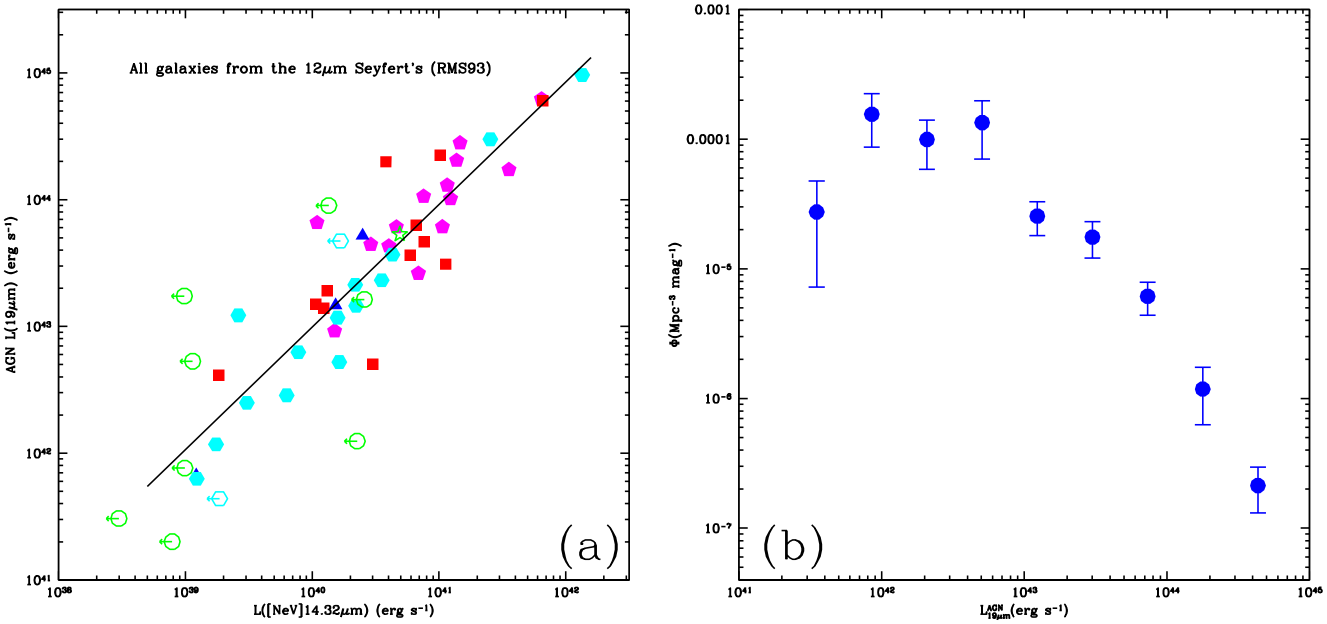

FIG. 21.— **a:** [NeV]14.3μm vs AGN 19μm luminosity, symbols are as in the previous figure. **b:** AGN 19μm luminosity function.

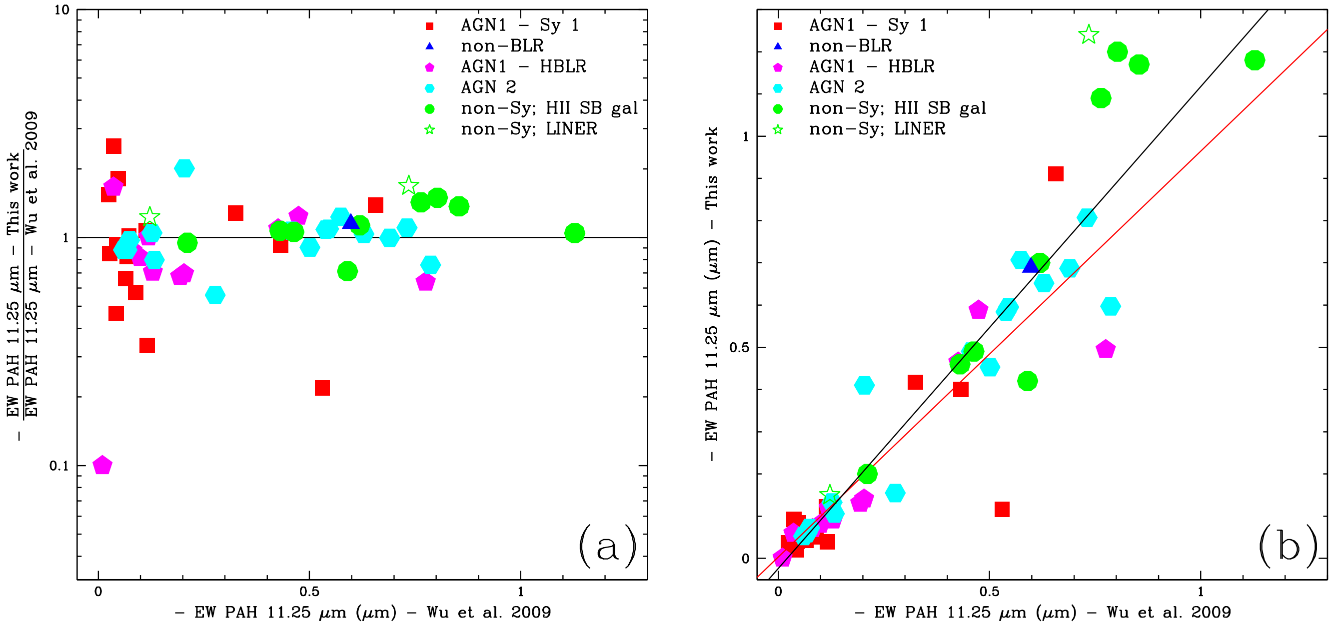

FIG. 22.— **a:** The ratio of the PAH 11.25μm EW calculated by Wu et al. (2009) to ours as a function of the values by Wu et al. (2009). **b:** PAH 11.25μm EW calculated by Wu et al. (2009) versus ours. We computed a mean square fit among the AGN1 + AGN2 class (values are fitted by the red line) and all the galaxy types (black line). For the slope values and confidence intervals, see the text.

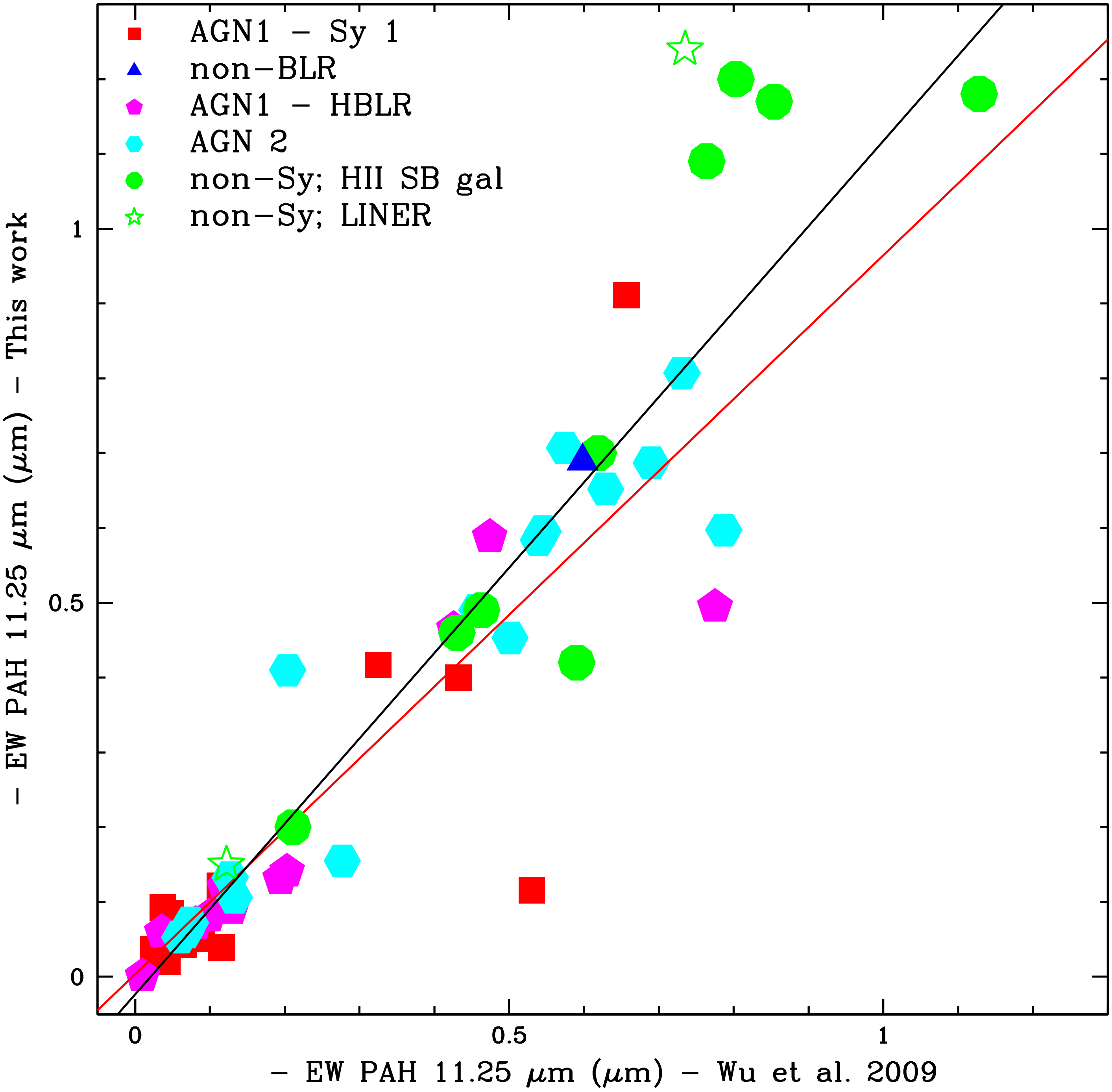
AGN1 – Sy 1
non–BLR
AGN1 – HBLR
AGN 2
non–Sy; HII SB gal
non–Sy; LINER
– EW PAH 11.25 μm (μm) – This work
0
0.5
1
– EW PAH 11.25 μm (μm) – Wu et al. 2009
0
0.5
1